# Molecular Dynamics Study of Electric Double Layer Capacitors: Modifying Electrode and Electrolyte Composition

By

Yu Zhang

Dissertation

Submitted to the Faculty of the

Graduate School of Vanderbilt University

In partial fulfillment of the requirements

for the degree of

DOCTOR OF PHILOSOPHY

in

Chemical and Biomolecular Engineering

May 31, 2019

Nashville, Tennessee

Approved:

Peter T. Cummings, Ph.D.

Rizia Bardhan, Ph.D.

Clare M$^{c}$Cabe, Ph.D.

Çağlar Oskay, Ph.D.

To my family, thank you for your unconditional love and support.

# ACKNOWLEDGEMENTS

First and foremost, I would like to express my deep gratitude to my advisor Professor Peter T. Cummings for his guidance, advice and support throughout the course of this work. I am always impressed and inspired by your extensive knowledge and keen scientific intuition. I learned not only from your knowledge, but also your generosity, and heartfully enjoy your mentorship. I would also like to thank my committee members: Professor Rizia Bardhan, Professor Clare McCabe, and Professor Çağlar Oskay. Your critiques and suggestions are an essential part of this work.

I would also like to give my sincere gratitude to the current and previous members of the McCabe and Cummings research groups, who have helped me with science and engineering problems. I'm especially thankful to Dr. Guang Feng, who helped me get started with molecular simulations. Thanks also to Dr. Ting Zheng for the useful discussions during his visit as an exchanging student, as well as his continuous encouragement. I also owe my gratitude to all of my collaborators in the Fluid Interface Reactions, Structures and Transport (FIRST) center. I truly appreciate the opportunities to be able to collaborate with exceptional experimentalists and computational researchers. Dr. Cheng Zhan and Dr. De-en Jiang (UC Riverside) for collaborations on the work of N-doped graphene and graphene edges； Dr. Boris Dyatkin and Dr. Yury Gogotsi (Drexel University) for collaborations on oxidized carbons; and Dr. Naresh C. Osti, Dr. Eugene Mamontov, and Dr. Hsiu-wen Huang (Oak Ridge National Laboratory) for the neutron scattering and X-ray scattering measurements.

My PhD life would be less colorful without the joy of family and friendship. I am honored to have met kind and fascinating friends in Nashville, and received their constant solicitude and company. Most importantly, I wish to acknowledge my family, my father Wangyou Zhang, my mother Lianmei Cai, my brother Ping Zhang, and my sister Qin Zhang, who have always been encouraging and supportive. I could not have done it without you.

# TABLE OF CONTENTS

Page

CHAPTER

# LIST OF TABLES

Table Page

# LIST OF FIGURES

# CHAPTER I

# INTRODUCTION

Electric double layer capacitors (EDLCs), also known as supercapacitors, are energy storage devices that are the subject of active research due to high power density and moderate energy density, broad operating temperature windows, and long cycle lifetimes.[1] Distinct from batteries, which convert external energy to charges through redox reactions, EDLCs store charge by electrosorption of ions from electrolyte onto an electrode surface, resulting in an electric double layer (EDL). This physical charge storage mechanism enables EDLCs to yield greater power densities compared to batteries. However, as a consequence of the surface electrosorption mechanism, EDLCs exhibit limited energy density. The past few years has seen a huge increase in the performance of supercapacitors due to the discovery of novel electrode and electrolyte materials, better understanding of charging/discharging mechanisms, as well as more intelligent design of hybrid systems.

Considerable effort has been taken to find electrode materials that increase the specific capacitance of EDLCs. Carbon-based materials, including graphene,[3,4] activated carbons,[5,6] and carbide-derived carbons,[7,8] have drawn researchers' attention due to their low cost, variety of form, ease of processability, electrochemical stability, controllable porosity, etc.[9] However, most experimental and computational studies have treated carbon electrodes as idealized surfaces with no remarkable heterogeneous features. In reality, experimentally produced porous and nonporous carbons feature reactive edge sites, semi-conductive electronic band structure, and synthesis-dependent robust surface chemistries. The effects of these non-ideal heterogeneous features remain largely unknown. Moreover, instead of discovering or synthesizing new materials, modifying the carbon electrode surfaces provides an alternative route to enhancing the performance of supercapacitors. However, this also requires a comprehensive knowledge of the effects of surface configuration and chemistry on the performance of supercapacitors.

In order to extract maximum benefits from novel electrode materials, researchers are also experimenting with the electrolyte to improve the voltage window of EDLCs. Recently, the development of IL-based supercapacitors has received much attention due to the outstanding properties of ILs as electrolytes. Ionic liquids electrolytes offer wider operating voltage windows than conventional aqueous electrolytes or organic electrolytes. However, their slow transport properties and low electrical conductivities in their neat states may reduce power densities, especially when neat ILs are confined in nanoporous electrodes.[10,11] In practice, ILs are often mixed with organic solvents to enhance their rate handling capabilities. Questions still remain regarding the effects of solvation on the energy density and power density of IL-based supercapacitors.

While experimental approaches are vital to address the aforementioned questions, computational techniques, such as molecular dynamics (MD) simulation, are powerful tools to investigate the interfacial phenomenon and provide underlining mechanisms for the capacitive performance. Previously, MD simulation has shown its successes in predicting supercapacitors capacitance and EDL structures.[12,13] Therefore, in this dissertation, we mainly rely on MD simulations to study the capacitive performance of supercapacitors, and their intrinsic EDL structures. In addition, we validate our simulation results with experimental observations from our collaborators.

In this work, we apply three different modifications to carbon-based electrodes and evaluate corresponding influences on their performance. In addition, we investigate the effects of cation sizes of ionic liquid electrolytes on the performance, as well as the influence of the dilution. Chapter II introduces supercapacitors and promising electrode and electrolyte materials. An introduction about computation models and MD simulation is provided in Chapter III.

We first modify graphene electrodes with nitrogen dopants. In Chapter IV, we study the effects of doping concentration and the configuration on the EDL capacitance, quantum capacitance, and total capacitance. It is found that pyridinic and graphitic configurations increase the total capacitance by increasing the quantum capacitance, but the pyrrolic configuration limits the total capacitance due to its much lower quantum capacitance than the other two configurations. Our investigation provides a deeper understanding of the capacitance enhancement of the nitrogen-doping in carbon electrodes and suggests a potentially effective way to optimize the capacitance by controlling the configurations of nitrogen-doping.

In Chapter V, we study the capacitance of graphene edge planes in contact with an aqueous electrolyte. Two types of graphene edges are studied, including the armchair edge and zigzag edge. We find that the graphene edge surfaces have higher capacitance than the graphene basal planes, and the zigzag edge has higher capacitance than the armchair edge. We further decompose the total capacitance into EDL capacitance, dielectric capacitance, and quantum capacitance. Our theoretical calculations provide a complete picture of the various factors contributing to the charge capacitive performance of graphene edges and suggests that the zigzag graphene edge could potentially enhance capacitance.

In Chapter VI, we investigate the influence of surface oxidization of graphene and carbide-derived carbon (CDC) electrodes on charge storage and ion dynamics of supercapacitors. Both experimental electrochemical tests and MD simulations show positive, electrolyte-specific influences of hydroxyl-free graphene electrode interfaces on capacitance. Furthermore, MD simulations of ion mobility with respect to electrode surface in the lateral and perpendicular directions reveal significantly slower diffusion performance on oxidized graphene. The effects of surface oxidization are also investigated for the porous CDCs, with different pore size distributions. Our efforts enhance the level of fundamental understanding of the effects of hydroxyl groups on electrode-electrolyte interfaces and resulting supercapacitor performance.

In Chapter VII, we inspect the effects of electrolyte composition and concentration on the bulk properties of an ion liquid electrolyte and the electrochemical performance on carbon-based electrodes, including pristine graphene, oxidized graphene, graphene armchair edge, graphene zigzag edge, onion-like carbon, and slit-pore carbon. We find the increase of cation size decrease the diffusivity of ion in the bulk and at the interface. In addition, we find that diluting the electrolyte weakens ion correlations in the bulk, and significantly improves ion dynamics in the bulk and at the interface. The capacitance of the two-edge electrodes decreases monotonically as the solvent concentration increases, while the capacitance of other non-edge electrodes exhibits a non-monotonic behavior and a capacitance maximum is observed. Our simulation results demonstrate that diluting an ionic liquid electrolyte could potentially enhance the energy density and power density of ion-liquid-carbon supercapacitors.

Finally, Chapter VIII concludes the results from proceeding chapters and provide insights into future research directions for materials for capacitive energy storage.

# CHAPTER II

# BACKGROUND

## 2.1 Electric Double Layer Capacitors

One major challenge in today's renewable energy industry is the ability to efficiently store the energy generated by sources, such as solar and wind. Due to the intermittency of these energy sources, electric energy storage technologies are required to dynamically match renewable energy generation. Pumped water and compressed air are commonly used technologies in power grids for intermittent renewable energy generation. However, these two technologies heavily depend on geographical location, hence showing relatively low round-trip efficiency.[14] Batteries and supercapacitors are commonly used electric energy storage devices that have a quicker response to demand variations, and are deployable to devices ranging from portable electronics to electric vehicles are needed.[15] A battery stores electrical energy through redox or intercalation reactions, and thus exhibit high energy density but low power density. There are two main types of supercapacitors: electric double layer capacitors (EDLCs) store electrical energy by reversible electrosorption of ions of electrolytes, which form electrical double layers; pseudocapacitors store electrical energy by reversible surface redox reactions or ion intercalation. Due to their essential advantages such as high power-handling ability, long cycle life, versatile geometric configuration, and scalability,[1] EDLCs have attracted great interest and emerged as a promising type of electrochemical energy storage device in recent years.[16] The global supercapacitor market was \$1.2B in 2014, and, by some estimates, will grow over 20% per year to more than \$7B in 2023.[17]

Thanks to the proliferation of novel electrode and electrolyte materials, the performance of supercapacitors has been significantly enhanced. However, the primary limitation of supercapacitors is their moderate energy density compared to batteries.[1,9] In general, the energy density of carbon-based EDLC is below 10 Wh kg$^{-1}$, while commercial Li-ion batteries have energy densities on the order of 100 Wh kg$^{-1}$.[9] The unit mass energy density $E$ stored in an EDLC is related to the capacitance and the voltage applied, i.e.,

$$E = \frac{1}{2} ACV^2 \tag{2.1}$$

Where $A$ is the specific surface area (SSA), $C$ is the capacitance, and $V$ is the applied potential. The most fundamental material research in this field has therefore focused on discovering or modifying electrode and electrolyte materials to maximize capacitance and minimize electrolyte breakdown at high potentials.

## 2.2 Electrode Materials

Since EDLCs rely on charge accumulation at electrodes under biased potentials, the electrodes typically have high specific surface areas and superb conductivity. Carbon materials have drawn researchers' attention due to their often-cited advantages, including low cost, wide potential window, relative inert electrochemistry, rich surface chemistry, and structural polymorphism.[18] The well-known allotropes of carbon include graphite, diamond, and fullerenes, each of which can exist in various materials with different electrochemical properties.[19] Typically, the sp$^2$ hybridized graphitic carbons satisfy all the requirements for the applications of EDLCs, and thus have been tested as electrode materials, including graphene,[3,4] activated carbons,[5,6] carbon nanotubes,[20] carbon onions,[21,22] and carbide-derived carbons.[7,8]

Two-dimensional graphene materials[23] made of atomic carbon sheets have many advantages as the electrode of EDLCs, including large surface area, electrochemical stability, superior stiffness and high electrical conductivity.[24,25] Single-layer graphene exhibits a theoretical SSA of 2630 $m^2$ $g^{-1}$,[4] and electrochemical capacitors based on graphene materials could achieve a theoretical specific capacitance of 526 F $g^{-1}$ if their entire surface area could be used.[26] Single-layer graphene can be produced via various mechanical or chemical exfoliation or via chemical vapor deposition, which are expensive and difficult to scale up for commercialization. In practice, graphene-based materials are often obtained by thermal or chemical processing of graphite.[4,27] Yet, even with strong reduction treatments, oxide impurities are likely to persist, and thus graphene is sometimes referred as reduced graphene oxide (RGO) in the literature.[28] In recent years, RGO has gained popularity as an alternative graphene-based material, partly due to the low cost of production. X-ray photoelectron spectroscopy (XPS) and nuclear magnetic resonance (NMR) studies have shown that hydroxyl and epoxide moieties are the predominant oxygen groups in graphene oxide.[29] However, experimental studies are inconclusive about whether the oxidation of graphene increases the capacitance or not. Xu et al.[30] found graphene oxide electrodes offer higher capacitance, while Buglione et al.[31] suggest the opposite. Furthermore, due to the difficulty of characterizing the graphene-based electrodes, previous computational studies typically used pure graphene as model electrodes.[32–37] Theoretical studies are needed to investigate how the functional groups on graphene sheets influence the electrolyte structure near the electrode surface and thus capacitance.

In addition, graphene sheets tend to restack during all phases of preparation and subsequent electrode production procedures, which evitable introduces edge sits. It has been shown in literature that the edges of graphene sheets exhibit higher capacitance than basal plane.[38]

Particularly, Yuan's experimental work illustrated that graphene edges have a specific capacitance four times higher than that of graphene basal planes.[39] Thus, it is highly desirable to develop edge-enriched graphene electrodes for the EDLC applications. However, theoretical understanding of the capacitance of graphene edge plane is still limited.

Recent experiments also showed a way to improve the capacitance of graphene-based supercapacitor by nitrogen (N) doping. Nitrogen doping is a simple but useful process for graphene because N-doping easily manipulates local electronic structures,[40] which allow for enhanced binding with ions in the electrolyte, and thus improves the electronic device performance.[41] By the plasma doping process, nitrogen atoms are expected to replace carbon atoms in the original graphene sheets and form three types of N-configurations: graphitic, pyridinic and pyrrolic. These structures can be distinctly recognized by XPS[42] and observed by scanning tunneling electron microscopy (STM)[43]. Studies have reported a more than 4-fold increase of specific capacitance for graphene in both KOH and organic electrolyte after N-doping.[44] Experimental[45,46] and theoretical[47] work have shown that the total capacitance for a few layer graphene-based supercapacitor, the total capacitance can be influenced by both EDL capacitance and quantum capacitance. However, the effects of doping configuration and concentration have not been studied. To have a more comprehensive understanding toward the doping effects of N-doped graphene supercapacitors, an integrated study combining various modeling methods is needed.

While graphene exhibits very high SSA, it has a low packing density ($< 0.5$ g/cm$^3$), which leads to empty space in the electrode flooded by electrolyte, thereby decreasing the gravimetric capacitance.[48] Porous carbon materials, however, have been developed recently to accommodate ions by optimizing porous structures. Actually, activated and carbide-derived carbons provide 1000-3000 m$^2$ g$^{-1}$ SSA, and can be easily scaled up and integrated into various device-specific applications.[49] CDC materials can be synthesized by halogen etching of various carbides (SiC, TiC, $Ti_3AlC_2$, etc.), whose porous structures can be tuned by varying $Cl_2$ treatment temperatures (300-1200 °C) and precursor materials.[50] The resulting structures contain robust surface chemistry, including C-Cl, C-H and C-$NH_2$ originated from the halogen treatment and annealing. Various hydroxyl and carbonyl groups are presented due to the exposure of the material to air.[49] Previous modeling efforts predict that the pore size and microstructure significantly impact the interactions with electrolytes, creating an energetically-favorable confinement in pores, and demonstrate a key role in charge storage.[51] Ion configuration inside porous carbons, however, is also impacted by surface chemistry and roughness. Functional groups with different surface charges may affect the ions' geometrical orientation and interface with the pore surface, impacting the charge storage density.[52] It is also reported that the presence of functional groups and lattice deformations disrupts $sp^2$ inherent $\pi$ bonding symmetry, and enhances the quantum capacitance by over 300%.[53] However, the coupled effect of surface chemistry and ion confinement condition in pores has not been studied by integrated efforts. Such unresolved problems also impede the integration of novel carbons as high-performance electrodes, such as glassy carbon (GC), high ordered pyrolytic graphite (HOPG) and single walled carbon nanotubes (SWCNTs).[49] Fundamental information regarding ion dynamics, ion structures in confined porous environment from modeling are necessary to correlate experimental observations.

## 2.3 Electrolyte Materials

The general electrolytes used for supercapacitors are aqueous electrolytes, molten salts, organic electrolytes and room temperature ionic liquids (RTILs). Molten salts require a high working temperature, limiting their applications. Aqueous electrolytes, such as sulfuric acid and potassium hydroxide solutions, are widely used in carbon-based supercapacitors because of their good conductivity. However, their applications are comprised by the key limitation of water decomposition at a low voltage (theoretically, 1.23 V). In addition, the corrosion induced by aqueous solution is another problem for reliability and safety. Moving from aqueous to organic electrolytes increases the cell voltage from 0.9V to 2.5-2.7 V,[1] which is also beneficial for energy density according to Equation (2.1). Neat RTILs can achieve even higher operating voltage, e.g. ~4.5 V for imidazolium ILs and ~5.5 V for pyrrolidinium and tetraalkylammonium ILs.[54] Besides, RTILs have attracted increasingly wide attention due to their low vapor pressure, high thermal and electrochemical stability, non-flammability and tunable miscibility.[55,56]

While an ever-growing number of viable RTILs are available, a careful choice of cation and anion allows the design of high voltage supercapacitors. For example, using CDC as electrode material and an [Emim$^+$][TFSI$^-$] as electrolyte, a high capacitance of 160 $\mathrm{F \cdot g^{-1}}$ can be obtained at 60 °C with a cell voltage of 3 V.[57] Tunability of RTILs is an essential property that allows optimal tailoring of electrolyte dimensions to specific electrode materials in order to maximize capacitance. However, experimental study of every combination of cation and anion is inefficient, and systematic and comprehensive methods that combine experimental tests and computational simulations are needed to address this question.

In addition, the typically high viscosity and low ionic conductivity of RTILs affect their performance in the temperature range from -30 °C to 60 °C, where supercapacitors are mainly used. Their slow transport properties may reduce the power density of supercapacitors, especially when neat ILs are confined in nanoporous electrodes.[10,11] In practice, ILs are often mixed with organic solvents to enhance their rate handling capabilities.[58–61] While most researchers found that solvation of ionic liquids greatly increases conductivities and the power densities of EDLCs,[6,21,62–

[64] the effects of solvation on the energy density are less clear. On one hand, slightly narrower voltage windows are expected when organic solvent is introduced into the electrolyte, which might compromise the energy density.[62,65] On the other hand, it has been shown by both experimental and computational studies that the addition of solvent improves capacitance of graphene-based EDLCs.[66–69] Particularly, Bozym et al. found that by diluting 1-ethyl-3-methylimidazolium bis(trifluoromethyl- sulfonyl)imide ([EMIm$^+$][TFSI$^-$]) with a miscible organic solvent, the differential capacitance on glassy carbon increases and reaches a maximum when the ion concentration is 5-10 mol%.[68] Similarly, Uralcan et al. observed nonmonotonic behavior of the capacitance as a function of ion concentration using molecular dynamics simulations, where the capacitance on graphene exhibited a maximum at intermediate concentrations.[69] Nevertheless, the effects of solvent concentrations on the performance of other carbon electrodes, such as OLCs and CDCs, are less studied.

This work in this thesis aims to understand the performance of IL-carbon-based EDLCs from both electrode and electrolyte viewpoints. Chapter IV, V, VI mainly focus on how modifications on carbon electrode materials change the performance of EDLCs, and Chapter VII probes factors from the electrolyte side, including cation size and solvent concentration.

# CHAPTER III

# COMPUTATIONAL METHODS

## 3.1 Classical Electric Double Layer Models

### 3.1.1 The Helmholtz model

In EDLCs, electric energy is stored by the formation of an electrical double layer through the electrosorption of counter-ions at the electrode surface. The concept of the EDL originated from the interfacial double layer model in classical surface physical chemistry, first proposed by Hermann von Helmholtz in 1853,[70] and formed by the co-ion exclusion and counter-ion adsorption. According to the Helmholtz model (shown in Figure 3.1(a)), the differential capacitance of an EDL can be computed as:

$$C = \frac{\varepsilon_r \varepsilon_0 A}{d} \tag{3.1}$$

where $A$ is the area of the electrode, $\varepsilon_r$ is the dielectric constant of the electrolyte solvent, $\varepsilon_0$ is the vacuum permittivity, and $d$ is the thickness of the Helmholtz layer. Note that this is independent of applied voltage or properties of the electrolyte other than the solvent dielectric constant.

Equation (3.1) can be used to estimate the areal capacitance for a planar electrode by:

$$C_d = \frac{C}{A} = \frac{\varepsilon_r \varepsilon_0}{d} \tag{3.2}$$

The value of $d$ in aqueous electrolytes is several angstroms. If we assume $d = 0.3$ nm, which is roughly the size of an atom, and the relative dielectric constant is 6 for an aqueous electrolyte, the areal capacitance is about 18 μF cm$^{-2}$. This value agrees well with reported values for EDLCs with aqueous electrolytes (around 15 μF cm$^{-2}$).[71] Ionic liquids usually have a dielectric constant about 10, but their sizes tend to be larger. If we assume $d = 1$ nm, then the areal capacitance is about 10 μF cm$^{-2}$, which is also close to experimental values (around 11 μF cm$^{-2}$).[71]

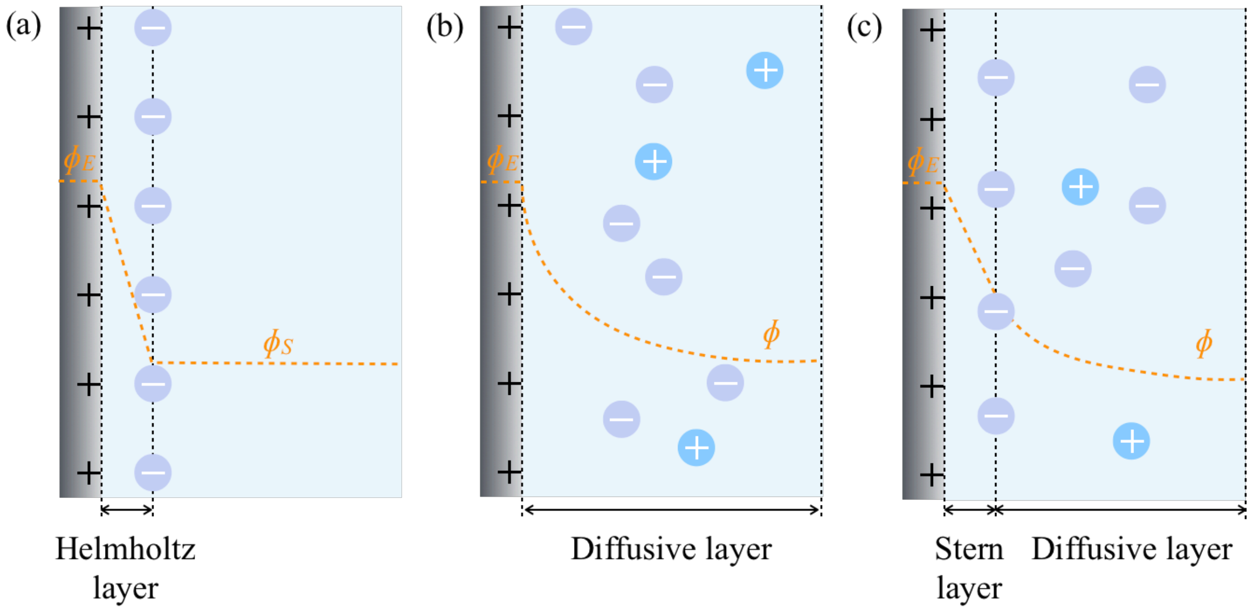

Figure 3.1 Electric double layer models. (a) Helmholtz model. (b) Gouy-Chapman model. (c) Gouy-Chapman-Stern model.

### 3.1.2 The Gouy-Chapman-Stern model

Gouy[72] in 1910 and Chapman[73] in 1913 derived an improved model for differential capacitance, which also depends on the electrode voltage and ionic concentration. The Gouy-Chapman model introduces a diffuse layer (shown in Figure 3.1(b)), which describes the ion charge distribution as a function of distance to the electrode surface, and used the Maxwell-Boltzmann statistics to account for the thermal effect. In 1924, Stern combined the Holmholtz model and the Gouy-Chapman model to describe the electrolyte/electrode interface. This model is known as the Gouy-Chapman-Stern model (shown in Figure 3.1(c)). According to this model, the adsorbed ions have finite size and form a Stern layer besides a diffuse layer. The Gouy-Chapman-Stern model gives a more general description of the electrolyte/electrode interfacial behavior, but is still highly simplified. For example, the diffusive ions in this model are considered to be point charges, while important ionic features that might influence capacitance, such as radii and valences, are ignored.

### 3.1.3 Recent models

More recently, Kornyshev *et al* proposed a model to describe the interfacial capacitance of the metal/ionic liquid system by solving the Poisson-Boltzmann equation, which treats the electrolyte by a mean-field lattice-gas model.[74] The model reduces to the nonlinear Gouy-Chapman model when ions are extremely sparsely packed in the electrolyte, but differs drastically if ionic volume exclusion takes more realistic values. Capacitance is predicted to have a maximum close to potential of zero charge, and decreases with the square root potential at large potentials. Futhermore, this model also accounts for the appearance of charge overscreening at the ionic liquid/electrode interface, where the charge in the first absorbed layer overscreens that on the electrode surface, and the subsequent layer again overcompensates the charge in its previous layer. However, these models neglect the atomic detail of electrolyte molecules, and lose the structural detail of electric double layers. As a matter of fact, all-atom molecular dynamics simulations or Monte Carlo simulations have been conducted in complement to validate the results.[75]

## 3.2 Molecular Dynamics Simulation

Molecular dynamics (MD) simulation is one the most widely used atomic modeling technique for computing the equilibrium and transport properties of a classical many-body system.[76] In comparison with other computational simulation methods such as Monte Carlo (MC), *ab initio* molecular dynamic (AIMD) and continuum theory, MD simulation can provide more realistic structural information of the EDLs. MC does not provide a complete description of the dynamic properties of the system, even though it is able to provide atomic details as MD simulation can. AIMD is not favored for modeling of EDLs, since it is limited to very small system sizes and short (10−100 ps) time scales, which are far from sufficient for EDL systems. Continuum simulation neglects the discrete nature of charge by treating ions as continuous medium, and hence loses the details of nanoscale structure. In so doing, the trajectories of atoms and molecules are determined by numerically solving the Newton's equations of motion. In the meanwhile, useful information at the microscopic level, such as atomic position, velocities and forces, etc., can be used to further obtain the system properties related to phases, structures and dynamics.

Previous studies have successfully applied MD simulations to study the capacitance of ionic liquids with different carbon electrodes, including graphene,[77,78] carbon nanotubes,[79,80] onion-like carbons,[78,81] CDCs,[51,82] etc. In addition, the length scale (nm) and/or time scale (ns) of MD simulations match various experimental measurements, including Atomic force microscopy (AFM), nuclear magnetic resonance (NMR), quasielastic neutron scattering (QENS), small angle neutron scattering (SANS), In situ X-ray reflectivity (XR), Small-angle X-ray scattering (SAXS), X-ray total scattering. Thus, MD simulation serves as a powerful complement to traditional experiments to probe the properties of EDLs, which is critical to understand the charge storage mechanism in supercapacitors.

## 3.3 Calculation of Capacitance

In molecular simulations of supercapacitors, a particular challenge is the modeling of electrodes. Because of the difficulty in defining a consistent classical atomistic model for a conductor, a simplified way to model the electrode is to assume a uniform constant charge for electrode atoms. This constant charge method has been used in many studies of supercapacitors.[33,47,54,83–85] The distribution of electric potential $\phi$ across the system is then obtained by solving Poisson equation as follows,

$$\nabla^2\phi = -\frac{\rho_e}{\varepsilon_0} \tag{3.3}$$

where $\rho_e$ is the spatial charge density, and $\varepsilon_0$ is the vacuum permittivity. This equation can be simplified as integrating the 1-D charge distribution for systems with simple electrode geometries, such as the planar surfaces (graphene), and spherical surfaces (onion-like carbons). For example, Figure 3.2 shows the MD simulation of IL-graphene supercapacitor. The special charge density in the direction perpendicular to the electrode surface can be calculated from the MD trajectories, and is shown in Figure 3.3(a). Then the potential distribution across a simulation channel can be calculated by integrating Equation (3.3):[86]

$$\emptyset(z) = -\frac{1}{\varepsilon_0}\int_0^z (z - z')\rho_e(z')\mathrm{d}z' - \frac{\sigma}{\varepsilon_0}z \tag{3.4}$$

where $z$ is the perpendicular distance from the electrode surface, and $\sigma$ is the surface charge density. Similarily, the potential distribution for a spherical electrode system is as below:[87]

$$\emptyset(r) = -\frac{1}{\varepsilon_0}\int_R^r \left(1 - \frac{r'}{r}\right) r'\rho_e(r')\mathrm{d}r' - \frac{\sigma R}{\varepsilon_0}\left(1 - \frac{R}{r}\right) \tag{3.5}$$

where $R$ is the radius of spherical electrode. However, the integration for other complicated systems is non-trivial. A customized code was developed to extract electric potentials for slit-pore electrode systems from GROMACS.[82]

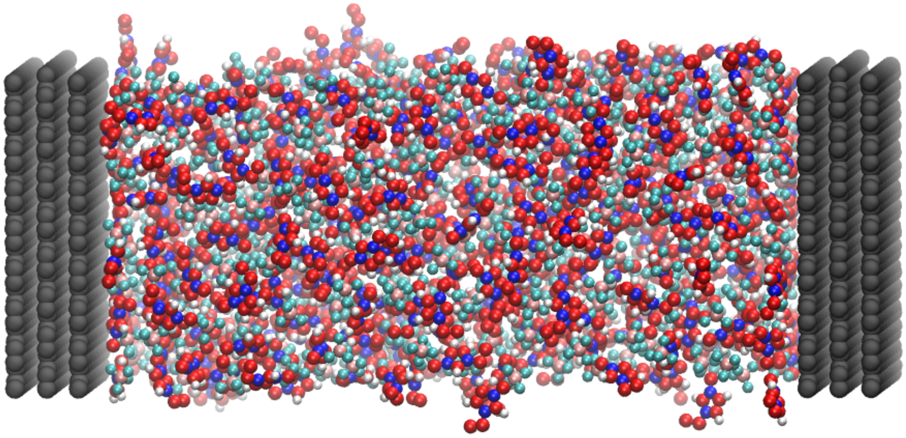

Figure 3.2 Simulation setup for graphene-ILs-based supercapacitors.

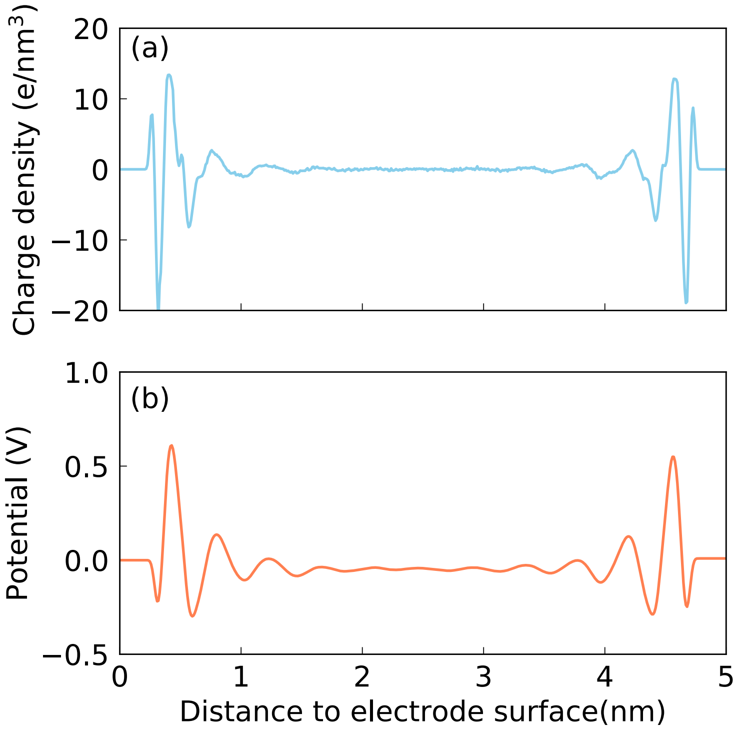

Figure 3.3 (a) Spatial charge density distribution. (b) Electrical potential distribution.

With the potential distribution calculated, the electrode potential is the difference between the potential at electrode surface and that in the bulk-like region. There are several types of capacitance. The specific areal capacitance normalized by SSA can be calculated by the following equation:

$$C_{sp} = \frac{\sigma}{\phi_{electrode} - \phi_{PZC}} \tag{3.6}$$

where $\sigma$ is the surface charge density, $\phi_{electrode}$ is the potential at the electrode, and $\phi_{PZC}$ is the potential of zero charge, i.e., $\phi_{electrode}$ at $\sigma = 0$. In simulation studies, the differential EDL capacitance is often computed numerically to compare with experimental results. The differential capacitance is defined as:

$$C_d = \frac{\mathrm{d}\sigma}{\mathrm{d}\phi_{electrode}} \tag{3.7}$$

The surface charge density is fitted as a function of the electrode potential with a fourth-order polynomial function. The differential capacitance is then calculated by differentiating the fitted charge density with respect to the electrode potential. The specific capacitance in a given potential range is then calculated by integrating the differential capacitance and dividing it by the potential range:

$$C_{sp}(\phi_1, \phi_2) = \frac{\int_{\phi_1}^{\phi_2} C_d(\phi)\mathrm{d}\phi}{\phi_2 - \phi_1} \tag{3.8}$$

where $\phi_1$ and $\phi_2$ represent the lower and upper bounds of the potential range.

It is worth noting that the constant charge method neglects the image charge effect of the electrode induced by local density fluctuations in the electrolyte solution.[88–91] Based on the theoretical work done by Siepmann and Sprik,[92] a constant potential method was then developed by Reed *et al.*[93] to take into account of such fluctuations. In this method, the electric potential ($\phi_i$) on each electrode atom is constrained at each simulation step to be equal to a constant potentiall ($V$), which is the value of the preset electrode potential. This electrostatic condition in the electrode is achieved by minimizing the total energy for the dynamic system, and leads to the following equation for charge ($q_i$) on each electrode atom:

$$V = \phi_i = \frac{\partial U_c}{\partial q_i} \tag{3.9}$$

where $U_C$ is the total Coulomb energy of the system.

This constant potential method has been used by many computational studies, especially for simulations of porous carbons.[51,94,95] However, it is worthwhile to mention that ion density profiles are almost the same from both methods, when electrolytes are RTILs and electrodes are flat and with biased voltage less than 6 V,[89] or when electrolytes are aqueous solutions and the biased voltage is smaller than 2V.[96] Considering the operating voltage of RTILs and aqueous solutions used in our research and the relatively cheap cost of the constant charge method, it is still applicable to use the constant charge method to model the EDL near flat surface.

# CHAPTER IV

# NITROGEN-DOPED GRAPHENE

Recent experiments have shown that nitrogen doping (N-doping) enhances capacitance in carbon electrode supercapacitors. However, a detailed study of the effect of N-doping on capacitance is still lacking. In this chapter, we study the doping concentration and the configuration effect on the electric double-layer (EDL) capacitance, quantum capacitance, and total capacitance. It is found that pyridinic and graphitic nitrogen can increase the total capacitance by increasing quantum capacitance, but pyrrolic configuration limits the total capacitance due to its much lower quantum capacitance than the other two configurations. We also find that, unlike the graphitic and pyridinic nitrogen, the pyrrolic configuration's quantum capacitance does not depend on the nitrogen concentration, which may explain why some capacitance versus voltage measurements of N-doped graphene exhibit a V-shaped curve similar to that of undoped graphene. Our investigation provides a deeper understanding of the capacitance enhancement of the N-doping effect in carbon electrodes and suggests a potentially effective way to optimize the capacitance by controlling the type of N-doping.

This work has been published in Ref. 109.

## 4.1 Introduction

In recent years, carbon nanomaterials such as carbide-derived carbons and graphene have become popular as supercapacitor electrode materials due to their combination of good conductivity and high specific surface area.[97–99] Graphene, unlike a traditional metal electrode, has a different capacitive performance due to its quantum capacitance, which is caused by its limited density of states (DOS) near the Fermi level.[100–102] In a graphene supercapacitor, total capacitance $C_{total}$ reflects the overall effect of quantum capacitance $C_Q$ and the electrical double layer capacitance $C_{EDL}$, which can be estimated by

$$\frac{1}{C_{total}} = \frac{1}{C_Q} + \frac{1}{C_{EDL}} \tag{4.1}$$

if one ignores the polarization effect of solvent on the electronic structure of electrode surface.[103] Under this assumption, one can treat EDL capacitance and quantum capacitance separately to study the total capacitance.[104–106] The contribution of quantum capacitance to the total capacitance is negligible when the electrode is metal such as Pt, which as extremely large DOS near the Fermi level. However, quantum capacitance is comparable to the EDL capacitance in 2D systems like graphene.

A consequence of the theoretical relationship of total capacitance with respect to quantum capacitance and EDL capacitance in Equation (4.1) is that $C_{total} < \min\left(C_Q, C_{EDL}\right)$, suggesting that in cases where the quantum capacitance is the bottleneck, the total capacitance may be improved by increasing quantum capacitance. To alter the DOS and thus change the quantum capacitance, the most common and widely used way is doping. Nitrogen-doped graphene has been studied for many years and shows a higher capacitance than pristine graphene and porous carbon. [107–112] Ruoff et al. attributes this capacitance enhancement to increase of quantum capacitance,[107] but Choi explains the increase of capacitance by the higher binding energy between pyridinic group and cation.[44] So this topic is still controversial due to the complex structure of N-doped graphene and the experimental difficulty of accurate measurement of the quantum capacitance.

In this chapter, we aim to elucidate the role of N-doping on the capacitance of graphene. To simply the complex structure, we choose the three most common configurations in N-doped graphene: graphitic, pyridinic, and pyrrolic configurations. These three configurations can be distinguished by X-ray Photoelectron Spectroscopy (XPS). Here we focus on a single-layer graphene sheet to evaluate the influence of N-doping on quantum capacitance and EDL capacitance. Besides different doping configurations, we are also interested in the effects of doping concentration on the capacitance of graphene electrode.

## 4.2 Computational Methods

Classical molecular dynamics simulations were performed to obtain EDL capacitance for the three types of N-doped graphene. As illustrated in Figure 4.1(a), the simulation channel consists of a slab of 1.0 M NaCl aqueous solution enclosed between two electrodes. The separation between the two electrodes is 5.0 nm to ensure a bulk-like behavior of the electrolyte in the channel center. The electrode configurations are shown in Figure 4.1(b-d). Specifically, for graphitic N-doped graphene, three different doping percentages are studies: the ratio between C atoms and total non-hydrogen atoms are 3.1%, 5.5%, and 12.5% respectively. For pyridinic N-doped graphene, the doping percentages are 6.1%, 9.7%, and 17.6%. And the doping percentages for pyrrolic N-doped graphene are 3.2% and 5.9%.

The simulations are performed in the canonical NVT ensemble using the MD package GROMACS.[113] The SPC/E model is used for the water molecules,[114] while the Lennard-Jones (LJ) parameters for $Na^+$ and $Cl^-$ are taken from the work of Smith et al.[115] All atoms of the graphene electrode are described by a polymer consistent force field (PCFF),[113,115] whose positions are fixed in space during the simulation process. Since the system has a slab geometry, the slab-PME method[116] is used here to compute the electrostatic interaction. The dimension vertical to the electrode is set to be 5 times the electrode separation to guarantee that the accuracy of the electrostatic force calculation is comparable to that of the two-dimensional Ewald method.[117] Each simulation is initiated at 800 K for 2 ns, and followed by 9 ns of equilibrating run at 298 K. Another 15 ns of production run is performed for analyses. The temperature of the system is controlled by Berendsen thermostat.[118] The time step of 2 fs is applied, and the atomic positions are saved every 4 ps. To ensure statistical accuracy, each simulation is repeated 3 times with different initial configurations.

Differential electrical potentials are created by varying the surface charge densities of the electrode. The excess charges are evenly distributed to the electrode atoms. The final partial charge of each atom is comprised of the excess charge and the partial charge from the force fields. To calculate the EDL capacitance, the surface charge density is fitted as a function of the electrode potential with a fourth-order polynomial. The EDL capacitance is then calculated by differentiating the fitted charge density with respect to the electrode potential. The quantum capacitance is calculated by our collaborators using the electronic density functional theory (DFT) with implicit solvation model through JDFTx code. Please refer to Ref. 109 for computational detail.

We establish the total capacitance as a function of applied voltage ($\varphi_a$) by combining $C_{EDL}$ and $C_Q$ as described in literature.[105] More specifically, the EDL capacitance is expressed a function of $\varphi_{EDL} = \varphi - \varphi_{PZC}$ , and the quantum capacitance is expressed as a function of $\varphi_{QC} = E - E_{Fermi}$. The applied voltage is the sum of partial voltages from both parts, i.e., $\varphi_a = \varphi_{EDL} + \varphi_{QC}$. $C_{EDL}$ and $C_Q$ are both voltage-dependent, but they share the same interfacial charge. Thus, we can obtain the relationship between surface charge density with applied voltage by summing up $\varphi_{EDL}$ and $\varphi_{QC}$ at the same surface charge density.[119]

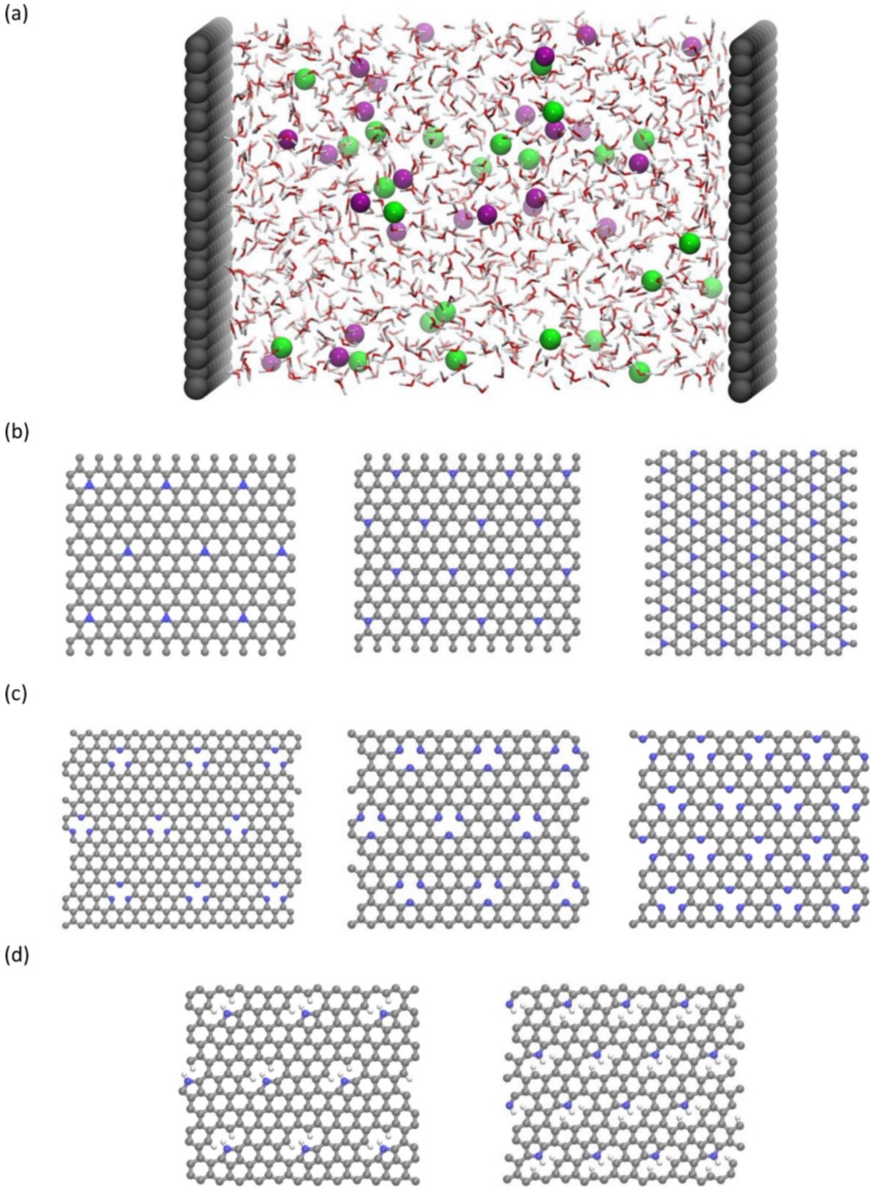

Figure 4.1 (a) Snapshot of the MD simulation system; (b) graphitic N-doped graphene; (c) pyridinic N-doped graphene; (d) pyrrolic N-doped graphene. Grey, blue, purple, green, red and white balls denote the carbon, nitrogen, $Na^+$, $Cl^-$, oxygen and hydrogen atoms respectively.

## 4.3 Results and Discussion

### 4.3.1 EDL capacitance of N-doped graphene

Generally speaking, the EDL capacitance of carbon electrodes is around 20 μF $cm^{-2}$ in aqueous electrolytes,[104] and around 8 μF $cm^{-2}$ in ionic liquid electrolytes.[120,121] The voltage window is about PZC±0.6 V for an aqueous electrolyte, and about PZC±1.5 V for an ionic liquid electrolyte. Since the calculation of quantum capacitance is mostly reliable in PZC±0.6 V, we focus on the capacitance of N-doped graphene electrodes in an aqueous electrolyte.

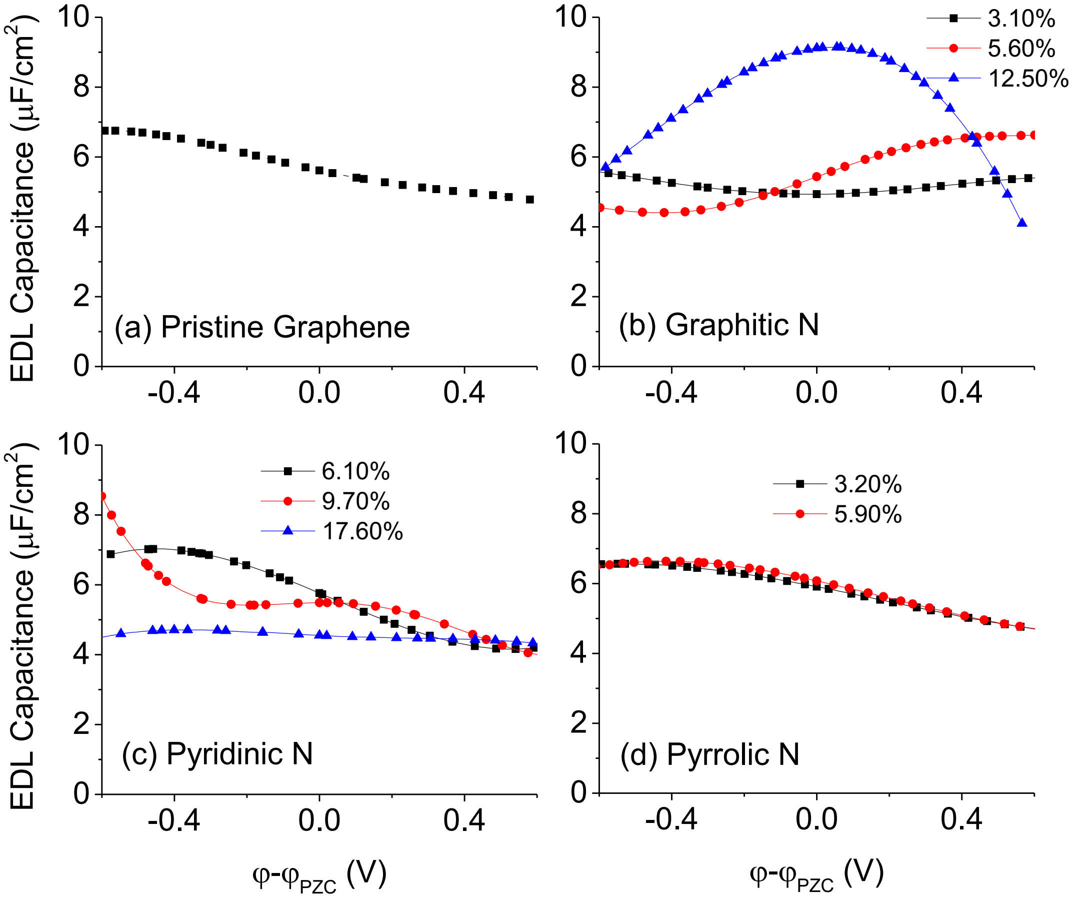

Figure 4.2 Electric double layer capacitance of (a) pristine graphene, and N-doped graphene, including (b) graphitic, (c) pyridinic, and (d) pyrrolic, with different doping concentrations.

Figure 4.2 illustrates the EDL capacitance calculated from MD simulations. One can see that comparing to pristine graphene, the EDL capacitance almost the same for the pyrrolic configuration, and perturbed to a small degree in the case of graphitic and pyridinic configurations. At high level of doping, we do see changes in the differential capacitance curves, as illustrated in Figure 4.2(b-c). The nitrogen dopants carry different partial charges from pristine carbon atoms, and a large concentration of the dopants changes the charge distribution on the electrode surface, hence affecting the differential capacitance. However, in most experimental studies, the total nitrogen content is lower than 10%. In this case, Figure 4.2 shows that the EDL capacitance does not change significantly in the N-doped graphene compared to pristine graphene. Similar result is also reported previously for N-doped graphene in an ionic liquid electrolyte.[122]

### 4.3.2 Quantum capacitance of N-doped graphene

Figure 4.3 shows the comparison between pristine graphene and three types of N-doped graphene. We observe that graphitic and pyridinic doping configurations greatly increases quantum capacitance, but pyrrolic doping configuration shows "V"-shaped curve, which is similar to the quantum capacitance curve of pristine graphene.

The quantum capacitance behavior of N-doped graphene can be explained by the n-doping and p-doping mechanism in the graphene sheets.[76] In the pyrrolic N-doping configuration, nitrogen atom can donate an extra electron in the $P_z$ orbital due to the formation of N-H bond, but the associated vacancy results in the loss of an electron in the delocalized $\pi$ bond. Thus, the total number of electrons does not change compared to pristine graphene. This explains why the pyrrolic N-doping configuration shows a "V"-shaped quantum capacitance that is similar to the pristine graphene. Graphitic N-doping can be regarded as an electron donator, which contributes additional electron to the delocalized π bond. Thus, the "Dirac Point" moves toward higher energy position and the DOS near the Fermi level increases. As a result, the quantum capacitance increases. In pyridinic N-doping, the number of electrons on the $P_z$ orbital does not change, but pyridinic N-doping causes a C vacancy, and the system loses an electron compared to the pristine graphene. Consequently, the system is like a p-doping semiconductor, which shifts the "Dirac Point" down, and the quantum capacitance increases.

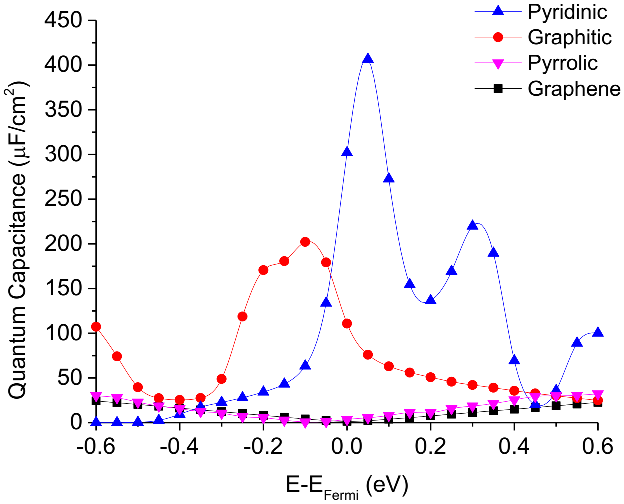

Figure 4.3 Quantum capacitance pristine graphene, and different configuration of N-doped graphene, with mole fraction of nitrogen at 3.1%, 9.7%, and 5.5% respectively.

### 4.3.3 Total capacitance of N-doped graphene

Now that we have computed the EDL capacitance and quantum capacitance separately, we can combine them to obtain the total capacitance. To compare with experimental results more clearly, we use the capacitance curve based on $C_{EDL}$ and $C_Q$ to calculate the integral capacitance from -0.6 V to 0.6 V (Table 4.1). Compare to the pristine graphene, the graphitic configuration increases the capacitance by about 63%, and the pyrrolic configuration increase the capacitance by about 82%. The capacitance enhancement predicted in our calculations is in good agreement with Fu's experimental work, which shows that the capacitance increases by about 50% after doping the nitrogen with graphitic- and pyridinic-dominated configurations.[123] Choi et al. applied nitrogen plasma to treat the graphene samples, which might introduce more defects, and hence found larger increase (over two times).[44]

Table 4.1 Integral capacitance (-0.6 V to 0.6 V) of different types of N-doped graphene.

| N-type | Integral Capacitance ($\mu$F/cm$^2$) |
|---|---|
| Pristine Graphene | 2.93 |
| Graphitic | 4.79 |
| Pyridinic | 5.34 |
| Pyrrolic | 3.05 |

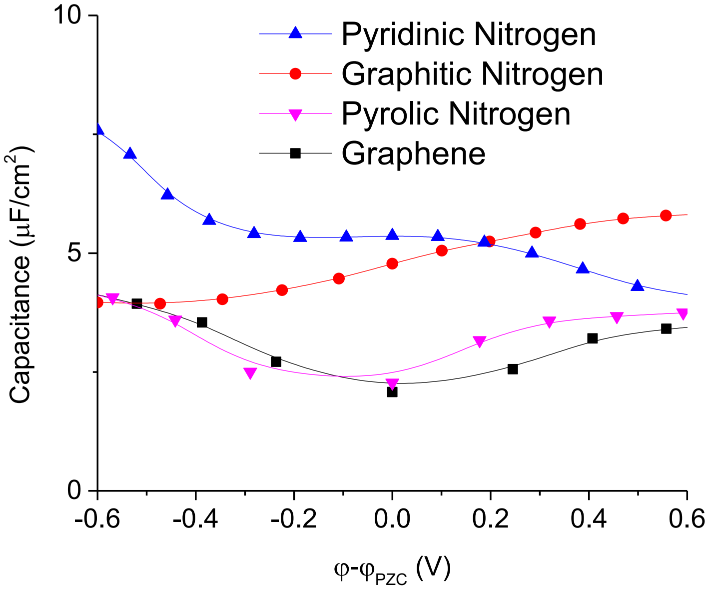

Figure 4.4 Total differential capacitance of different configurations of N-doped graphene.

We obtain further insights from the total differential capacitance plotted in Figure 4.4. Graphitic and pyridinic N-doped graphene both have high and similar integral capacitance, but very different differential capacitance distribution. Graphitic N-doped graphene shows a stable and flat differential capacitance curve across the voltage window. Pyridinic N-doped graphene exhibits higher differential capacitance than that of graphitic N-doped graphene under negative surface potential, but its differential capacitance drops as the electrode potential increases. In addition, the calculated total differential capacitance curves of graphitic and pyridinic are very close to the EDL capacitance from MD simulation. This is because the quantum capacitance in both cases is much larger than the EDL capacitance. Thus, the charge storage in the EDL constitutes the major part of total charge storage. Unlike the graphitic and pyridinic N-doped graphene, pyrrolic N-doped graphene shows a "V"-shaped differential capacitance, similar to that of pristine graphene, and is in good agreement with the experiment.[107]

### 4.3.4 Relevance to real N-doped carbon electrodes

In real carbon materials, the electrode structure is very complicated. Experiments measure BET surface area and pore size distribution to obtain some porosity information in carbon materials. For N-doped graphene, the commonly used way to identify different doped nitrogen configurations and their relative concentration is XPS measurement of N(1s) binding energy (B.E.). Our calculation has shown that different N-doping configurations have EDL capacitance and quantum capacitance. In real materials, experimentally obtained N-doped graphene contains a mixture of different N-doping configurations. Accordingly, the integrated capacitance should depend on the relative proportion of each configuration, which can be controlled by synthesis methods,[124,125] and characterized by XPS. It has been shown both experimentally and theoretically that pyridinic and pyrrolic doping configurations have stronger thermal stability than the graphitic configuration at high temperatures.[44,112,126,127] Combination of these thermal stability studies and our computational results shed lights on the enhancement on N-doped graphene supercapacitors. The most implication is to increase the concentration of pyridinic and graphitic doping configurations, and reduced the percentage of pyrrolic doping configuration. Since the graphitic doping configuration is much less stable than the other two configurations, one should focus on the pyridinic doping configuration if high-temperature treatment is needed in synthesis.

Our calculated EDL capacitance (Figure 4.2) and quantum capacitance (Figure 4.3) of pyrrolic N-doped graphene both show a "V"-shaped capacitance curve as a function of biased voltage, which is very similar to that of the pristine graphene. This calculation shows a very good agreement with Rutoff's experimental measurements in aqueous electrolytes, where the pyrrolic configuration is the major doping configuration shown in their XPS analysis.[107] The large capacitance enhancement observed by Choi[44] and Liu[108,128] is probably attributed to the graphitic and pyridinic doping configurations.

## 4.4 Conclusions

We have calculated the electric double layer, quantum, and total capacitance of nitrogen-doped graphene with different doping configurations and concentrations to investigate their effects on capacitance. The EDL capacitance was calculated by classical MD simulation and quantum capacitance by Kohn-Sham DFT. Classical MD simulations of the doped graphene electrodes in 1 M NaCl aqueous electrolyte shows that nitrogen doping does not change the EDL capacitance notably for the doping concentration examined. On contrast, the quantum capacitance of graphene is significantly increased when nitrogen is doped with the graphitic or pyridinic configuration. The combination of the EDL capacitance and quantum capacitance yields estimates for the total capacitance, which is in good agreement with experimental results. When the pyrrolic configuration is dominant, the differential capacitance shows a “V”-shaped curve, similar to that of the pristine graphene. When the graphitic or pyridinic configuration is dominant, a large enhancement of capacitance is observed. In conclusion, the graphitic and pyridinic nitrogen doping configurations can greatly increase the total capacitance by increasing the quantum capacitance, however, the pyrrolic configuration exhibits similar capacitance compared to the pristine graphene. Given that the pyridinic and pyrrolic nitrogen doping configurations have higher thermal stability than the graphitic doping configuration, a good strategy is to dope the nitrogen with the pyridinic configuration and avoid the pyrrolic configuration.

# CHAPTER V

# GRAPHENE EDGES

In Chapter IV, we have demonstrated that through nitrogen doping, we could substantially increase the capacitance of graphene, which is a combination of EDL capacitance and quantum capacitance. Recent experiments have shown that electric double layer capacitors with graphene edge electrodes exhibit higher capacitance than those with graphene basal planes. However, theoretical understanding of this capacitance enhancement is still limited. In this chapter, we further decompose the total capacitance into electrical double layer capacitance, quantum capacitance and dielectric capacitance, and evaluate their contributions to the total capacitance. Two common types of graphene edges are studied here, including the zigzag edge and the armchair edge, which all show higher total capacitance than the graphene basal plane. In additional, the zigzag edge shows higher capacitance than the armchair edge. Molecular dynamics simulations are conducted to study the EDL capacitance, and the graphene edges are found to exhibit higher EDL capacitance than the basal planes due to their better adsorption of counter-ions on the rough surfaces. We rely on a self-consistent joint density functional theory to estimate the quantum capacitance and dielectric capacitance, and the electronic structure plays an important role. Our work therefore elucidates the capacitive energy storage of graphene edge supercapacitors that take into account both the EDL structure and the electrode's electronic structure.

This work has been published in Ref. 180.

## 5.1 Introduction

To effectively implement electric double layer capacitors, many efforts have explored the sp2-based carbon materials, such as graphene, owing to their large specific surface areas, high conductivity, good chemical stability.[1] Recent experimental[45,104] and theoretical[47] researches on graphene-like electrodes has focused on elucidating the fundamental molecular behavior at the electrode-electrolyte interface. Both the EDL capacitance ($C_{EDL}$) and quantum capacitance ($C_Q$) contributes to the total capacitance ($C_{Total}$). The EDL capacitance can be obtained from classical methods, such as molecular dynamics simulation, classical DFT, or Monte Carlo simulation. And the quantum capacitance can be separately computed through electronic density functional theory.[105,129,130] The capacitance of graphene is found to be limited by its low electronic density of states at the Fermi level.[45,46,102,131] But several studies have proposed structrural[53,132,133] and chemical[109,121] modifications on graphene-like electrodes to increase the quantum capacitance. Particularly, one effective way, as described in Chapter IV, is to increase the electronic density of states at the Fermi level via nitrogen doping.[109]

These previous studies have limited the scope to the graphene basal planes, where most ion adsorption mostly occurs. But recent experiments have indicated that the graphene edge planes could have higher capacitance than the graphene basal plane.[39,134–137] For one thing, the EDL structure can be noticeably perturbed by the edge sites, hence affecting the EDL capacitance. For another thing, the edge sites might also modify the electric structure, and subsequently affect quantum capacitance. In addition, there is a study showing that the dielectric screening also contributes to the total capacitance.[138] While the potential applications of high-quality graphene edges has been proposed by researchers,[139] theoretical understanding of the impact of edge defects on the EDL, quantum, and dielectric capacitance is still limited.

In this chapter, the total capacitance is presented as the sum of three parts, including EDL capacitance, quantum capacitance, and dielectric capacitance. We apply classical molecular dynamics simulations to investigate the contribution of the EDL capacitance to the total capacitance. In addition, our collaborators calculate the quantum capacitance and dielectric capacitance by a self-consistent joint density functional theory. Combining all three parts of the capacitance, we provide a comprehensive computational insight into the capacitive performance of graphene edges.

## 5.2 Computational Methods

Figure 5.1 shows the structure of the zigzag edge and armchair edge, where the $sp^2$ carbon atoms at the edge sites are terminated by H atoms. Molecular dynamics simulations are conducted in the canonical NVT ensemble using the MD package GROMACS.[140] As illustrated in Figure 5.2, each simulation system consists of a slab of 6 M NaCl aqueous electrolyte enclosed between two electrodes, which are set at least 5.0 nm away from each other to guarantee a bulk-like behavior of the electrolyte in the channel center. The SPC/E model is used for the water molecules,[114] while the Lennard-Jones (LJ) parameters for $Na^+$ and $Cl^-$ are taken from the work of Smith et al.[115] A polymer consistent force field (PCFF) describes the carbon atoms in pristine graphene and the edge sites.[113,115] The positions of the electrode atoms are fixed during the simulation.

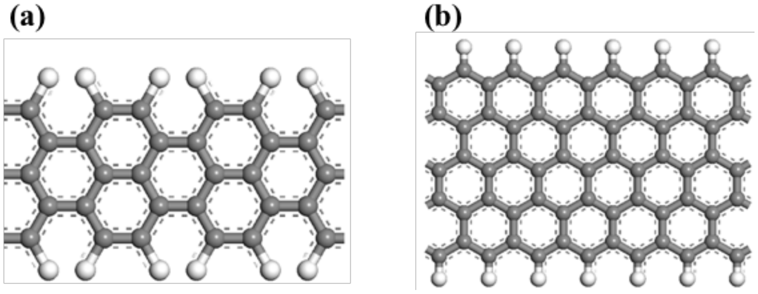

Figure 5.1 The top view of the (a) armchair edge and (b) zigzag edge.

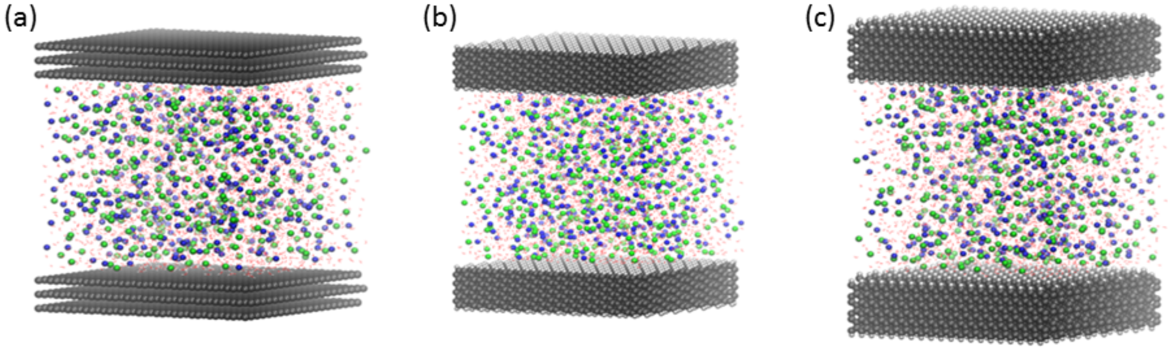

Figure 5.2 Snapshots of classical molecular dynamics simulations of 6 M NaCl aqueous solution enclosed between two graphite electrodes: (a) basal plane; (b) armchair edge; (c) zigzag edge.

To simulate the charged electrodes, external charges need to be added onto the electrodes. As shown in Figure 5.2, the DFT calculation shows that the excess charge mainly distributed on the H atoms at the interface. Thus, in MD simulations, the net surface charges are evenly distributed on the surface H atoms at the interface. The slab-PME method[116] was used to compute the electrostatic interaction, and the dimension vertical to the electrode surface was set to be 5 times of the separation distance of the two electrodes, in order to ensure that the accuracy of the electrostatic calculation is comparable to that of the two-dimensional Ewald method.[117] Each simulation is initiated at 800 K for 2 ns, followed by 8 ns of annealing to 298 K, and then equilibrated at 298 K for 10 ns. Another production run of 10 ns is then performed for data analysis. The temperature of the system is maintained by a Berendsen thermostat.[141] The time step of 1 fs is applied. Each simulation is repeated three times with different initial configurations to reduce statistical errors.

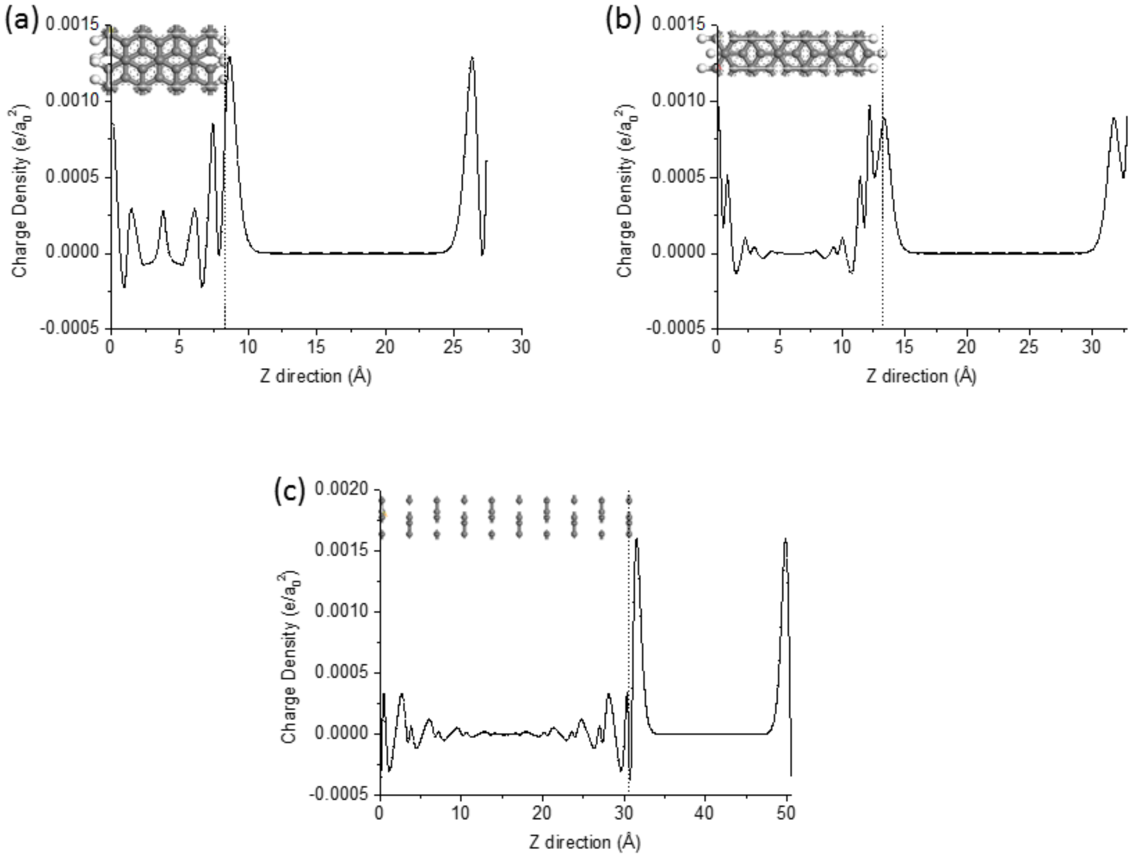

Figure 5.3 Excess charge distribution of positively charged electrodes: (a) armchair edge; (b) zigzag edge; (c) 10-layer graphene. The surface charge density is fixed at 20 μC/cm$^2$.

Of note, a constant-potential MD method, which allows the charge on the surface to fluctuate according to its local environment, can avoid the arbitrariness in assigning charges to the surface atoms, and describes the EDL more accurately than the constant-charge method used here.[35] We choose the latter for its faster speed and simpler implementation, yet it can still capture the influence of surface morphology on the EDL capacitance and estimate the EDL contribution in the total capacitance.

The quantum capacitance and dielectric capacitance is computed by JDFT. Please refer to Ref. 180 for computational details. The total has the following relationship with the EDL capacitance, quantum capacitance, and dielectric capacitance:

$$\frac{1}{C_{Total}} = \frac{1}{C_{EDL}} + \frac{1}{C_Q} + \frac{1}{C_{Dielectric}} \tag{5.1}$$

The dielectric capacitance arises from the dielectric screening of the electrode, where the charge exhibit a distribution inside the electrode.

## 5.3 Results and Discussion

### 5.3.1 MD results on EDL capacitance

To find out how the surface morphology would influence the EDL capacitance, we charge the surface in two different ways: (i) the surface carbon atoms are assigned with the partial charges from the force fields (labled as FF); (ii) the partial charges on the surface carbon atoms are manually set to zero (labeled as non-FF). In both cases, additional electrode charges are homogeneously added to the surface H atoms when charging the electrodes. The non-FF case can directly show how the surface roughness affects the EDL capacitance, while the FF case gives a combined consequence of surface morphology and partial chares inside the electrode.

The differential EDL capacitance from MD simulations is plotted in Figure 5.4. Because the graphene edge planes are non-flat, we need to consider the effect of solvent accessible surface area (SASA; Table 5.1). We plot both SASA-normalized (Figure 5.4(a)) and un-normalized (Figure 5.4(b)) EDL capacitance. One can see that the edge plane always has higher EDL capacitance than the basal plane, but the difference is smaller for the SASA-normalized one. Since the edge planes have higher SASA, so the SASA is one of the reasons for the higher EDL capacitance of the edge planes. Figure 5.4(a) shows that the EDL capacitance of edge planes is 20-25 μF $cm^{-2}$ near PZC, and decreases as the potential goes up. When there is less surface inhomogeneity (non-FF), the differential capacitance is smaller at low potentials.

Table 5.1 Solvent Accessible Surface Area (SASA) relative to that of the basal plane

| Electrode | Solvent Accessible Surface Area (SASA) |
|---|---|
| Basal Plane | 1 |
| Armchair Edge | 1.2 |
| Zigzag Edge | 1.41 |

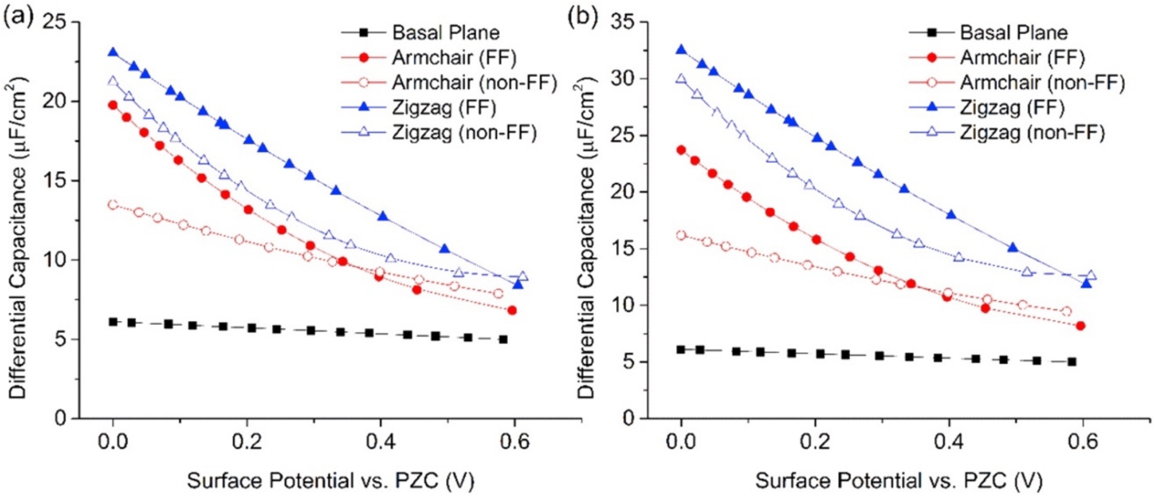

Figure 5.4 Differential capacitance of graphene basal and edge planes from classical molecular dynamics simulations: (a) solvent accessible surface area (SASA)-normalized; (b) un-normalized, surface area determined by the lateral cell size.

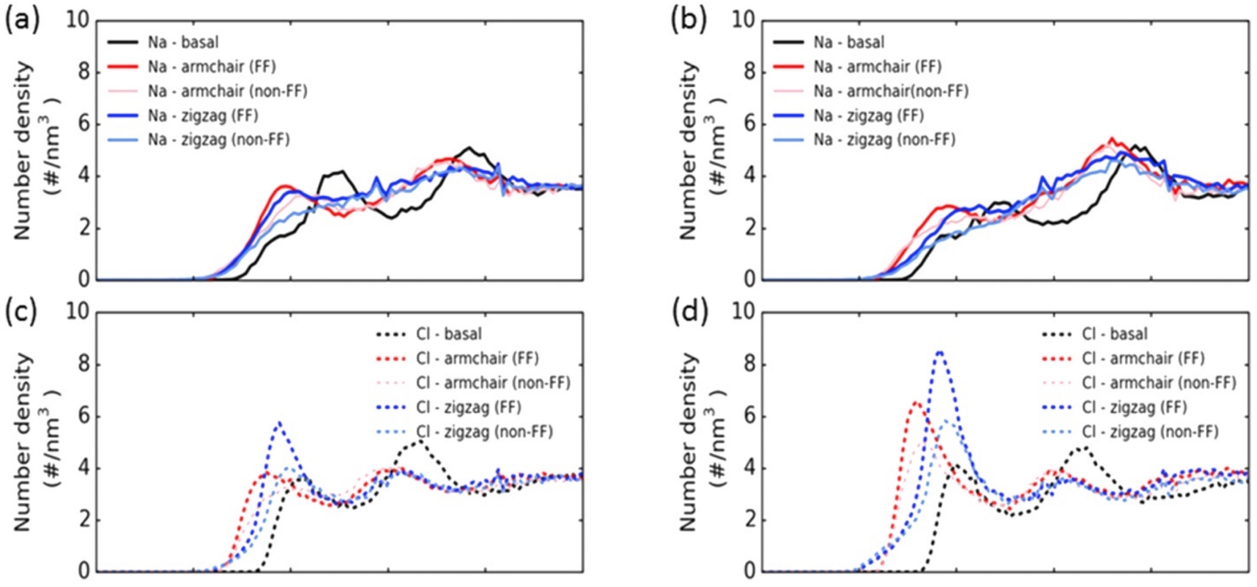

Figure 5.5 $Na^+$ (a, b) and $Cl^-$ (c, d) distributions in the electrolyte at PZC (left panel) and 0.3 V vs PZC (right panel) from classical MD simulations for various electrodes.

The ion distribution and EDL structure at various potentials are plotted in Figure 5.5. With the same potential drop, the responses of counter-ions are shown in Figure 5.5(c-d). One can see that the edge planes have higher counter-ion ($Cl^-$) concentrations near the edge surface than the basal plane, which means that the edge planes could form a thinner Helmholtz layer that yields higher EDL capacitance. Thus, there are two factors causing the increase of EDL capacitance on the graphene edge planes compared to the graphene basal plane. First, the surface morphology of graphene edge favors the adsorption of $Cl^-$. The counter-ion in the FF case also has higher peaks than that in the non-FF case, indicating that surface charge inhomogeneity also makes the EDL capacitance higher. Second, the corrugation on the edge planes leads to higher SASA, which also induce a stronger counter-ion response under the same biased potential, thereby yielding higher EDL capacitance.

### 5.3.2 JDFT calculations of the quantum capacitance and dielectric capacitance

The electronic structure of the solvated electrode in implicit electrolyte is solved by JDFT. To understand the charging inside the graphene edge planes, we calculate the planar-average total electrostatic drop, $\Delta\psi(r)$, of positively charged edge planes. As shown in Figure 5.6(a), $\Delta\psi(r)$ of the armchair edge keeps increasing in the electrode region, meaning that the electrode cannot completely screen the external electric field from the Helmholtz layer at the electrolyte/electrode interface. This phenomenon is the same as the screening effect in the few-layer graphene electrodes, as shown in Figure 5.6(c). The $\Delta\psi(r)$ in Figure 5.6(a) still shows a trend to increase in the center region of the electrode. We expect that increasing the thickness of the edge planes will make $\Delta\psi(r)$ continue to increase until it reaches a critical thickness. From this perspective, the armchair edge is not a promising candidate as the electrode material of EDLCs. On the other hand, the zigzag edge shows different $\Delta\psi(r)$ distribution: $\Delta\psi(r)$ increases steeply within the vicinity of the edge, and then becomes stable inside the electrode. The external electric field only penetrates into a small distance into the zigzag edge, before it is completely screened. Consequently, the zigzag edge has a higher capacitance than the armchair edge and the basal plane.

Unlike the case of few graphene where we can clearly distinguish three contributions (quantum, dielectric, and EDL), it's hard to distinguish the EDL screening and dielectric screening parts in the potential drop for the edge planes. This is because it's hard to define the electrode-electrolyte interface (dashed lines in Figure 5.6(a-b)). Thus, we group the potential drops caused by the EDL screening and dielectric screening together as the non-quantum potential drop, shown in Figure 5.6(d). The armchair edge has a similar potential contribution to a 10-layer graphene, and both contain significant contributions from quantum capacitance.

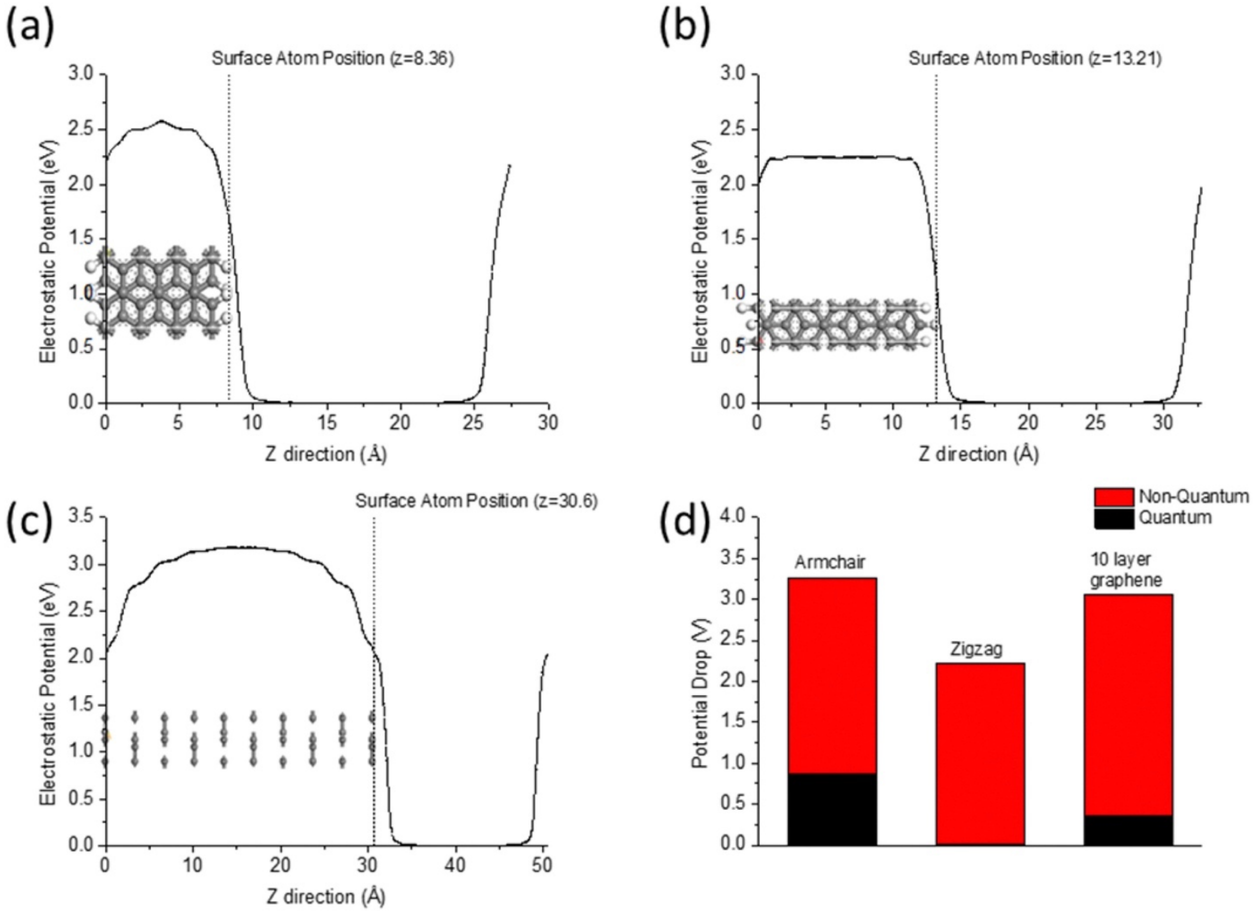

Figure 5.6 Planar-average electrostatic potential drop in the electrode, $\Delta\psi(r)$, along the electrode surface normal at a fixed surface charge density of 20 μC/cm$^2$ for: (a) armchair edge, (b) zigzag edge, and (c) 10-layer graphene; (d) is the corresponding total potential drop including both quantum (Fermi level shift) and non-quantum (band shift) contributions.

The calculated areal capacitance of each electrode is listed in Table 5.2. The predicted total capacitance of the armchair edge is 6.1 μF cm$^{-2}$, which is lower than the capacitance of the 10-layer graphene (6.52 μF cm$^{-2}$). We notice that the armchair edge has higher non-quantum capacitance, but its quantum capacitance is less than half of that of the 10-layer graphene. Zigzag edge, however, has much higher capacitance (9.04 μF $cm^{-2}$), due to its high quantum capacitance and low electrostatic potential drop inside the electrode.

Table 5.2 JDFT results of total capacitance and quantum and non-quantum contributions

| Electrode | $C_{tot}$ ($\mu$F/cm$^2$) | $C_Q$ ($\mu$F/cm$^2$) | $C_{NQ}$ ($\mu$F/cm$^2$) |
|---|---|---|---|
| Armchair | 6.12 | 22.83 | 8.37 |
| Zigzag | 9.04 | 1142 | 9.11 |
| 10-layer graphene | 6.52 | 56.18 | 7.38 |

Recent experiment shows that the edge-enriched graphene exhibit about 50% enhancement of capacitance over the graphene basal plane.[136] Previous theoretical understanding on this enhancement focuses mainly on the increase of quantum capacitance.[142] Our work here shows that the enhancement actually depends on the type of edge planes.

### 5.3.3 Combination of MD and JDFT results

From previous session, the MD simulations provide the EDL capacitance, while the JDFT calculations offer the total capacitance together with quantum and non-quantum contributions. To estimate the third contribution due to the electric screening, we plot the potential drops by combining both MD and JDFT results in Figure 5.7. The dielectric contribution is separated from the non-quantum potential drop (obtained from JDFT) by subtracting the EDL contribution (obtained from MD). The calculated dielectric capacitance is 19.28 μF $cm^{-2}$ for the armchair edge, and 13.33 μF $cm^{-2}$ for the zigzag edge. Here again, we note that due to the less-defined electrolyte-electrode boundary for the edge planes, the separation of the dielectric and EDL contributions can be subject to large uncertainty.

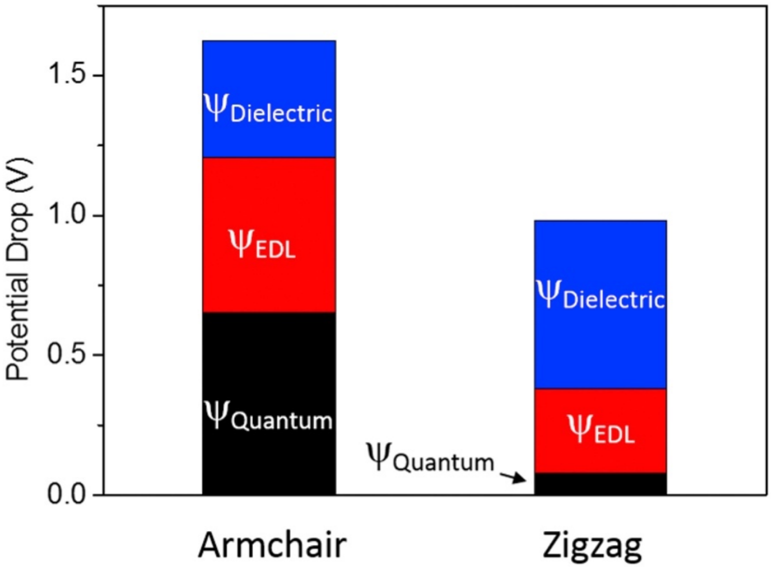

Figure 5.7 Comparison of the potential drop contributions between armchair and zigzag edges by combining JDFT and CMD data. The surface charge density is 8 μC cm$^{-2}$ in both cases.

The areal capacitance of pristine graphene is about 6μF cm$^{-2}$, which has been reported by many experimental studies.[94,104,143] Liu's experimental measurements on edge-enriched graphene nano-ribbons shows that the areal capacitance at low scanning rates is about 10 μF cm$^{-2}$,[136] which shows good consistency with our calculation on the capacitance of zigzag edges in Table 5.2. Experimental work by Cen et al. also found that the edge planes have higher capacitance than the basal plane.[134] More recently, Yang et al. studied the EDL capacitance of carbon-terminated graphene edge planes via MD simulations, and found that the EDL capacitance is enhanced at the edge planes, especially for an interlayer spacing around 5.0 Å.[144] Unlike the planar surfaces, the role of edge sites in nanoporous carbons can be different. For example, Merlet et al. used MD simulations to study the EDL structure in porous carbons, and found that edge sites (carbon electrode with concave curvatures) tends to retain lower local charge than other configurations, indicating the importance of nanoconfiment.[94]

As indicated by atomic level imaging[145] and DFT calculations,[146,147] zigzag edges are more favorable than armchair edges on metal surfaces. The experimental synthesis of the pure zigzag edge has been achieved by Fasal et al.[148] We think that the experimentally observed capacitance enhancement in graphene nano-ribbons may be attributed to the zigzag edges, rather than the armchair edges.[136]

## 5.4 Conclusions

In this chapter, we have studied the capacitance of graphene edge planes in contact with an electrolyte. Classical molecular dynamics simulations explicit electrolytes reveal that graphene edges have higher EDL capacitance than the graphene basal plane. The increase of capacitance is resulted from two reasons: the surface inhomogeneity of edge surfaces favors the adsorption of counter-ions; the edge planes have higher solvent-accessible surface area. Of the two types of edges studied, the zigzag edge exhibit higher EDL capacitance than the armchair edge. In addition, the joint density functional theory calculations with implicit solvation models shows that the zigzag edge has higher total capacitance than the armchair edge and the basal plane. The quantum capacitance, dielectric screening, and EDL responses all contribute important roles in the total capacitance. Our theoretical work provides a complete picture of various factors influencing the capacitive performance of graphene edges, and suggests that the zigzag edge could potentially increase the capacitance of graphene-based supercapacitors.

# CHAPTER VI

# SURFACE OXIDIZATION

Previously, most experimental and computational studies have treated carbon electrodes as idealized surfaces with no remarkable, heterogeneous features. In fact, experimentally produced porous and nonporous carbons feature edge sites, semiconductive electronic band structures, and synthesis-dependent robust surface chemistries. In Chapter IV and V, we have shown that modifications of the graphene surface by changing its surface chemistry or surface morphology could potentially enhance the performance of graphene-based supercapacitors. In this chapter, we further discuss the effects of surface oxidization and ion confinement on the capacitance and electrosorption dynamics of ionic liquids in carbon-based supercapacitors. We employ different electrode models to represent different confinements: the planar electrode models are used to represent the graphene nanoplatelets (GNPs), and the slit-pore models are used to represent the carbide-derived carbons. First, we study a neat ionic liquid on planar surfaces, and find the surface oxygen groups result in lower charge accumulation densities on the planar surface, which diminishes capacitance. Second, simulations of two solvated ionic liquids on planar surfaces, and the solvent is found to play a vital influence on the capacitance. And finally, neat ionic liquids are confined inside slit-pores, where different capacitance behaviors are observed depending on the pore size. Our MD results are complemented by experimental measurements, including electrochemical cyclic voltammetry, quasi-elastic neutron scattering (QENS), and inelastic neutron scattering (INS), which validates the capacitance performance and probes the structure, dynamics, and orientation of ions confined in divergently functionalized pores. With this integrated approach, we obtain a fundamental and comprehensive understanding of the significance of surface oxidization on ion orientations, accumulation densities, and capacitance not only on simple planar surfaces, but also in hierarchical pore architectures of carbon electrodes.

Part of this work has been published in Ref. 195 and Ref. 217. In addition, a manuscript is accepted as a peer-reviewed publication.

## 6.1 Introduction

The fundamental charge storage mechanism in supercapacitors involves voltage-driven electrosorption of ions from bulk electrolyte into layers of co-ions and counter-ions on electrode surfaces.[149] Although recent insights have broadened the understanding of this charging process and assessed the electrolyte-electrode interface beyond the classical Gouy-Chapman-Stern double layer approach (section 3.1.2),[74,150] computational and experimental findings still struggle to identify and decouple all relevant parameters.[151,152] Most studies have focused on the ratio of ion size to pore size,[82,153] along with electrode curvature effects,[51,94,154] to describe the fundamental influence of electrolyte dynamics on capacitance. However, very few studies have investigated the influence of surface composition and structure, including chemical species and structural defects, on interaction of electrolytes with electrode under (1) neutral conditions, (2) static applied potentials, and (3) dynamic fluctuating voltage processes. Approaches that tackle this information gap must decouple ion confinement from functionalized surface effects and correlate experimental findings with computational models to provide novel comprehensive insights into supercapacitor charging process.

Surface nonideality might affect the supercapacitance in the following ways. First, previous efforts, which defunctionalized porous carbons via vacuum annealing, contradicted conventional wisdom and underscored the beneficial influences of surface groups and graphitic defects on capacitance.[49] Surface functional groups (−O, −N, −H, etc.) may distort ideal graphene's π−π bonding symmetry and increase theoretical quantum capacitance by 15-50 μF cm$^{-2}$.[53,155,156] Second, specific chemical species (−OH, −R−O−R−, etc.) may interact with ions and selectively influence their orientation on the functionalized pore wall, impeding their mobility and depressing specific capacitance by 2-3 μF cm$^{-2}$.[151,157] Finally, center groups (−HCOO, −O−C=O, etc.) may sterically hinder ion movement by electrosorbing ions at narrow pore openings and blocking rapid electrolyte transport.[158,159] At the same time, functional groups depress intrinsic metallic-like conductivity of carbon electrodes. Electrically resistive pore walls cannot effectively screen co-ion via image forces and, subsequently, exhibit lower charge storage densities.[88]

Ion confinement and pore size have a strong influence on the net effects of surface chemistry and disorder at the electrolyte-electrode interface. Electrolytes assemble into short-range clusters inside of pores to minimize the free energies of systems. Although confined ions typically exhibit lower mobilities than their bulk counterparts,[160] lower electrolyte densities ($\rho \approx 0.8\rho_{bulk}$) maximize ion transport rates.[161] Furthermore, lower pore loading results in localized clustering of ions and heterogeneous pore filling in terms of local densities.[162] Such strong composition variations may yield unexpected effects, and confined ions may become more mobile than bulk electrolyte species.[163] Finally, surface functional groups, which may attract (or repel) such charge agglomerations, influence ion density and resulting electrolyte dynamics.

The density of electrolyte filling in porous systems depends on the intrinsic properties of electrosorbed electrolytes. Ionic liquids, such as [EMIm$^+$][TFSI$^-$], do not require solvent to exhibit fluid-like mobility and dynamics in pores. However, they demonstrate degree of ion-ion correlation in the bulk state and weak solvation radii of cations and anions around each other.[159,164]

The molecules typically feature functional groups with strong dipole moments (C−F, S=O, −S−N−S−, etc.) that interact with surface charges and functional groups. Depending on the matching electrolyte-electrode surface chemistries, the FSI may be either ionophilic or ionophobic, which, in turn, may align the ions in parallel or perpendicular configurations with respect to pore walls.[165–167] Although prior research has demonstrated improved ionophilicity of oxygen-rich pores and has correlated functional group content with rate handling capabilities,[168] differences in ion dynamics between oxidized and defunctionalized pore systems are not yet certain. Since the cation and anions of ionic liquids typically feature different sizes and functional groups, simulations and experiments predict different dynamics for each. MD simulations predict that alkyl chains take advantage of lower pore filling and occupy leftover void space in the pores.[169] These significant ion density and dynamics transformations likely govern capacitive behavior.

To date, most computational analyses of electrosorption have relied on coarse-grained approximations of ions and tailored the simulated porosities of corresponding electrodes to match the electrolyte dimensions.[170,171] This approach fails to take into account the complex dimensions and chemical properties of ions. In particular, neat ionic liquids include large functional group chains and adopt non-spherical configurations in confined states.[169] The sizes of anions and cations are often mismatched, and carbon electrodes with a single, well-defined pore diameter may not be optimal for co-ion and counter-ion electrosorption. Therefore, tailoring electrolyte ions to electrode pore may require non-trivial approaches, including complex pore architectures with multiple pore dimensions. Such an approach might facilitate ion partitioning and higher packing densities.

Such an approach will be needed to investigate the electrosorption of asymmetric ions with different dimensions into hierarchical porous architectures. Few studies have analyzed the state and correlations of ions in confinement, factored in the effects of electrodelyte-electrode interactions, or attempted to reconcile experimental characterization with computational modeling. Scattering measurements based on neutron or synchrontron X-rays can provide length- and time-scale information with high levels of atomic resolution and molecular motions. A comprehensive analysis can provide insight into ion orientation, densification, and dynamics in confinement.

In this chapter, to determine the influence of electrode surface composition on capacitance and ion dynamics, we evaluated nonporous and porous carbon structures with surface oxygen functional groups. Our work focuses on the influence of oxygen-containing moieties since they are very common in experimental electrode materials, such as activated carbons or reduced graphene oxides. We integrate MD simulations with multiple experimental measurements to characterize behaviors of ions on nonporous carbons surfaces or inside porous carbons.

## 6.2 Computational Methods

### 6.2.1 Simulation of a neat ionic liquid on oxidized graphene

We “oxidized” graphene with hydroxyl groups to study the effects of surface oxidization on the performance and ion dynamics of nonporous carbon supercapacitors. As shown in Figure 6.1(a), each simulation consisted of an electrolyte in a channel enclosed by two electrodes. The walls were set 8 nm apart so that the density in the channel center is close to that in bulk. Figure 6.1(b) shows the all-atom model used for the ionic liquid, whose force field was derived from Lopes et al.[172,173] The simulation of oxidized graphene differs from those of pristine graphene by incorporating hydroxyl groups on both sides of the former, which covers 2.8% of surface carbon atoms (Figure 6.1(c)). The configuration of hydroxyl groups was taken from the DFT work of Yan et al,[174] and the non-bonded parameters were defined by the AMBER force field.[175] The Lorentz-Berthelot combining rule was used to calculate the Lennard-Jones parameters for unlike atoms. Net charges were added uniformly to the atoms on the electrode surface. The charge neutrality of the system was maintained by assigning same amount but opposite sign of net charges to the electrodes.

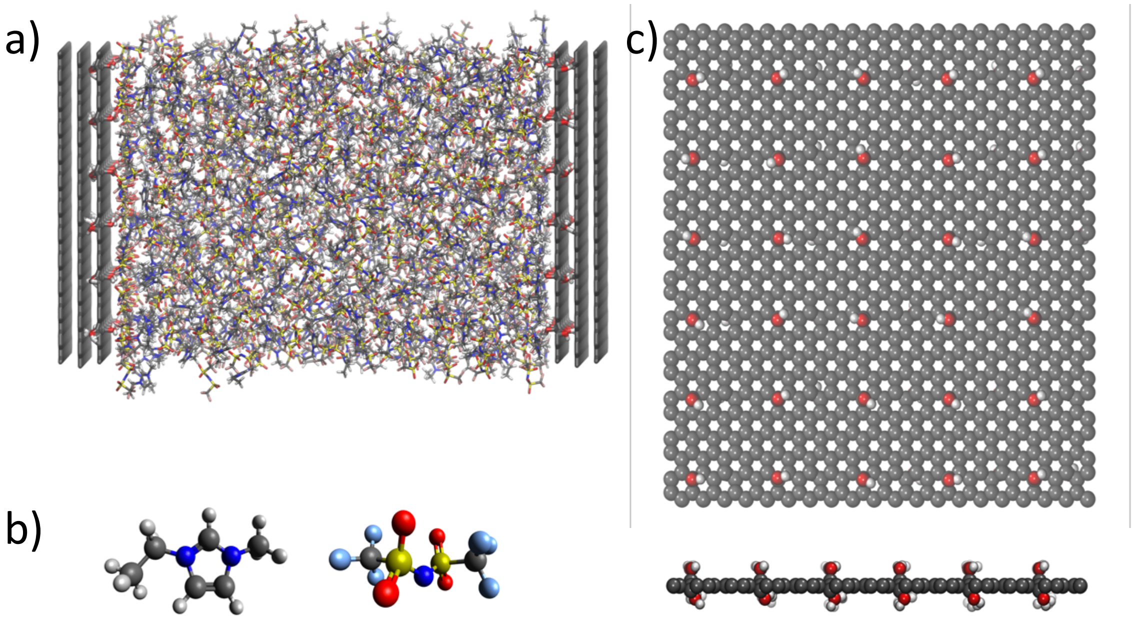

Figure 6.1 Snapshots from the simulation of the neat ionic liquid on oxidized graphene. (a) Simulation channel. (b) Molecular structures of [EMIm$^+$] and [TFSI$^-$]. (c) Hydroxylated graphene.

The simulations were conducted in MD package GROMACS.[140] The slab-PME method was used to compute the electrostatic interaction in the two-dimensional periodic geometry.[116] The vertical box length was set to five times of the electrode separation distance to ensure the accuracy of electrostatic force calculation was comparable to that calculated from a two-dimensional Ewald method. Each simulation was initialized at 800 K and was, subsequently, annealed to 298 K over

8 ns. After 8 ns of equilibration at 298 K, 10 ns production runs were carried out. The temperature was controlled by the Nose-Hoover thermostat with relaxation time of 0.4 ps. During the simulation, all $sp^2$ carbon atoms remained rigid, while $sp^3$ carbon atoms and the hydroxyl groups were allowed to rotate and bend. Each simulation was repeated three times with different initial configurations to ensure the reproducibility of simulation results. The corresponding experiments were done on graphene nanoplatelets. Details on materials synthesis, intrinsic characterization, and electrochemical measurements can be found in Ref. 195.

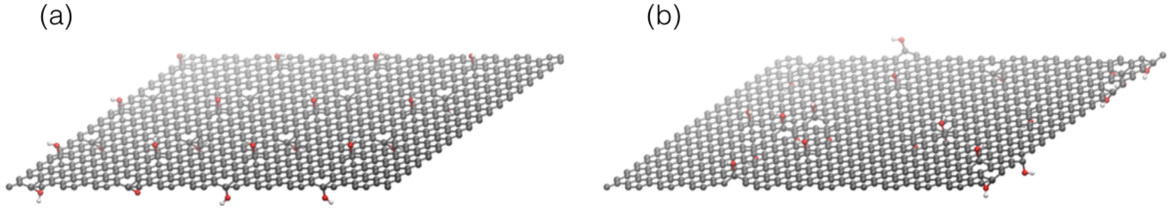

Figure 6.2 Snapshots of hydroxylated graphene with (a) regular pattern, and (b) random pattern.

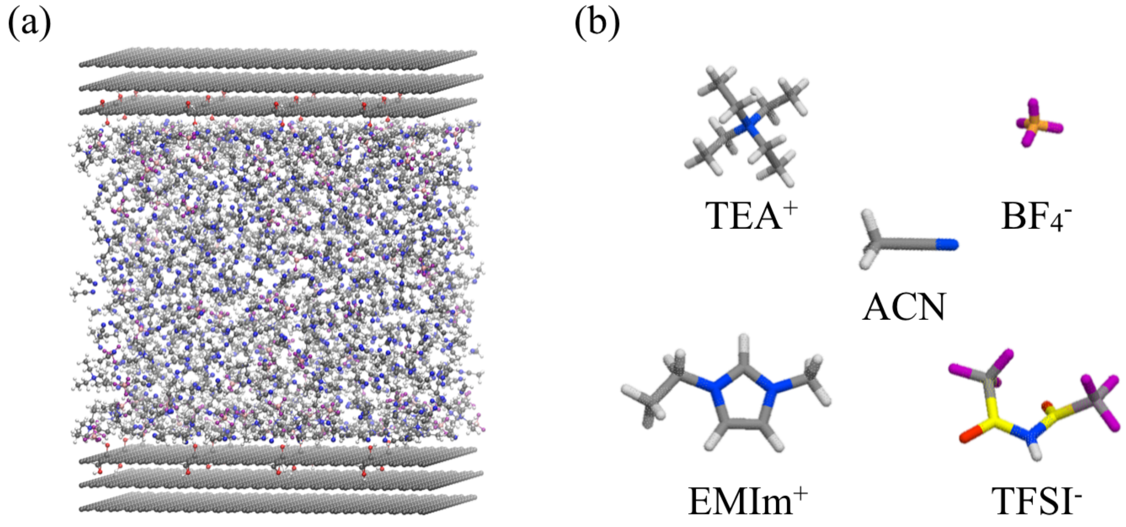

Figure 6.3 Snapshots from the simulation of solvated ionic liquids on oxidized graphene. (a) channel simulation. (b) Molecular structures of the ions and solvent.

### 6.2.2 Simulation of solvated ionic liquids on oxidized graphene

The simulation setup is similar to that in section 6.2.1, with only some small differences. In the previous section, the hydroxyl groups on the graphene surface are regularly distributed. Here, we further examine the random distribution of hydroxyl groups (configurations shown in Figure 6.2). The simulation system and the electrolyte composition are shown in Figure 6.3. The electrodes were set 5 nm away from each other to achieve a bulk-like behavior in the channel center. The electrolytes used are ionic liquid solutions in acetonitrile. Besides a equimolar solution of [EMIm$^+$][TFSI$^-$] in acetonitrile, we also include 1.5 M tetraethylammonium tetrafluoroborate ([TEA$^+$][BF$_4^-$]) solution in acetonitrile (ACN) as the electrolytes. The force fields for [TEA$^+$][BF$_4^-$] and ACN were adopted from literature.[176] Experimental measurements were also carried out for the same solvated ionic liquid electrolytes on graphene nanoplatelets. We skip the details about the measurements here.

### 6.2.3 Simulation of neat ionic liquids inside porous carbons

The porous carbons used here are the carbide-derived carbons, which are synthesized via $Cl_2$ etching of metal carbides at 300−1200 ℃, and allows precise tuning of subnanometer pore distributions.[177] The slit-pore model has been used in MD simulations to represent a typical pore in CDCs.[82,178] As shown in Figure 6.4, the simulation box consisted of two slit-pores immersed in the ionic liquids. The slit-pores had a length of 12 nm in the axial direction. Each pore was separated by 7 nm from the neighboring pore, which simulated a reservoir between the electrodes of sufficient size that allowed unconfined electrolyte ions to reach bulk behavior in the middle of the reservoir. Oxidized CDCs were modeled by adding −OH groups to the surface layers of slit-pores. This slit-pore model was constructed for two different pore sizes, including 0.8 nm and 2.6

nm. We also studied ionic liquids with different cation sizes, including [EMIm$^+$][TFSI$^-$] and [OMIm$^+$][TFSI$^-$]. [EMIm$^+$][TFSI$^-$] was only confined in the 0.8-nm slit-pore, while [OMIm$^+$][TFSI$^-$] was used for both the 0.8-nm slit-pore and the 2.6-nm slit-pore. Corresponding CDCs were synthesized and characterized by our experimental collaborators. More details about experimental setups can be found in Ref. 195 and Ref. 217.

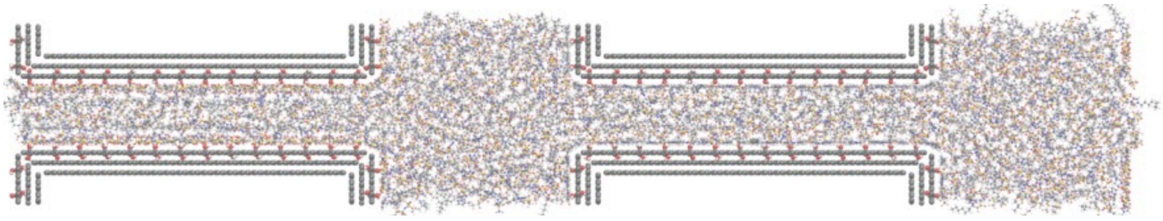

Figure 6.4 Snapshot of the slit-pore model.

## 6.3 Results and Discussion

### 6.3.1 Neat ionic liquids on nonporous carbons

As shown in Figure 6.5, electrochemical tests of [EMIm$^+$][TFSI$^-$] with nonporous defunctionalized and oxidized GNPs decoupled the influence of oxygen groups from ion confinement. Defunctionalized GNP surfaces exhibits superior performance during both dynamic and static electrochemical cycling conditions. Oxygen-free planar electrodes demonstrate greater capacitance and superior rate handling abilities (Figure 6.5(a)) than their oxidized counterparts. The CV sweeps (Figure 6.5(b)) for external surface GNP electrodes do not show any ion sieving or noticeable charge impedance. Static CA voltage-dependent specific step charge accumulation densities for bare, defect-free graphene nanoflakes noticeably exceed those of oxidized surfaces

(Figure 6.5(c)). Furthermore, charge accumulates at the same rate, regardless of electrode surface chemistries. Electrochemistry analysis concludes that defunctionalized, flat electrodes with no ion confinement outperform the charge storage densities of oxidized surfaces and do not suffer from hindered ionic liquid dynamics.

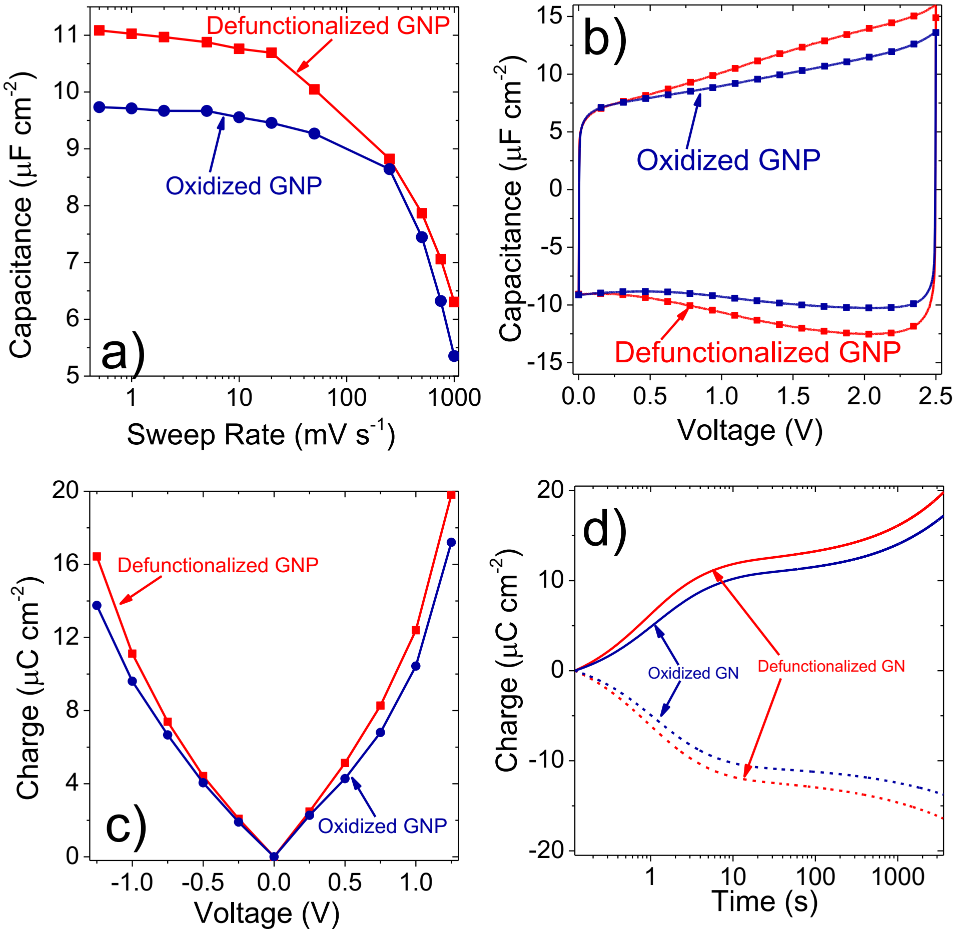

Figure 6.5 (a) Rate handling comparison of performance of non-porous oxidized and defunctionalized GNPs in the 0.5–1000 mV s$^{-1}$ sweep range. (b) Cyclic voltammetry plot showing differences in capacitance of [EMIm$^{+}$][TFSI$^{-}$] for defunctionalized vs. oxidized GNPs at a 5 mV s$^{-1}$ sweep rate. (c) Step charge accumulation for differently functionalized GNPs in the -1.25 V↔+1.25 V range. (d) Charge accumulation vs. time during a square wave 0⟶±1.25 V step.

In MD simulations, we focus on the ion number density and capacitance on defunctionalized and oxidized graphene, as shown in Figure 6.6. In addition, we are also curious about the orientation of adsorbed ion on the electrode surfaces. Figure 6.7 shows how the orientation angle is defined: (1) the agnleformed by the normal vector of the electrode surface and the normal vector of the imidazolium ring of [EMIm$^+$]; (2) the angle between the normal vector of the electrode surface and the vector connecting the two carbon atoms in [TFSI$^-$]. The angle distributions of ions are shown in Figure 6.8.

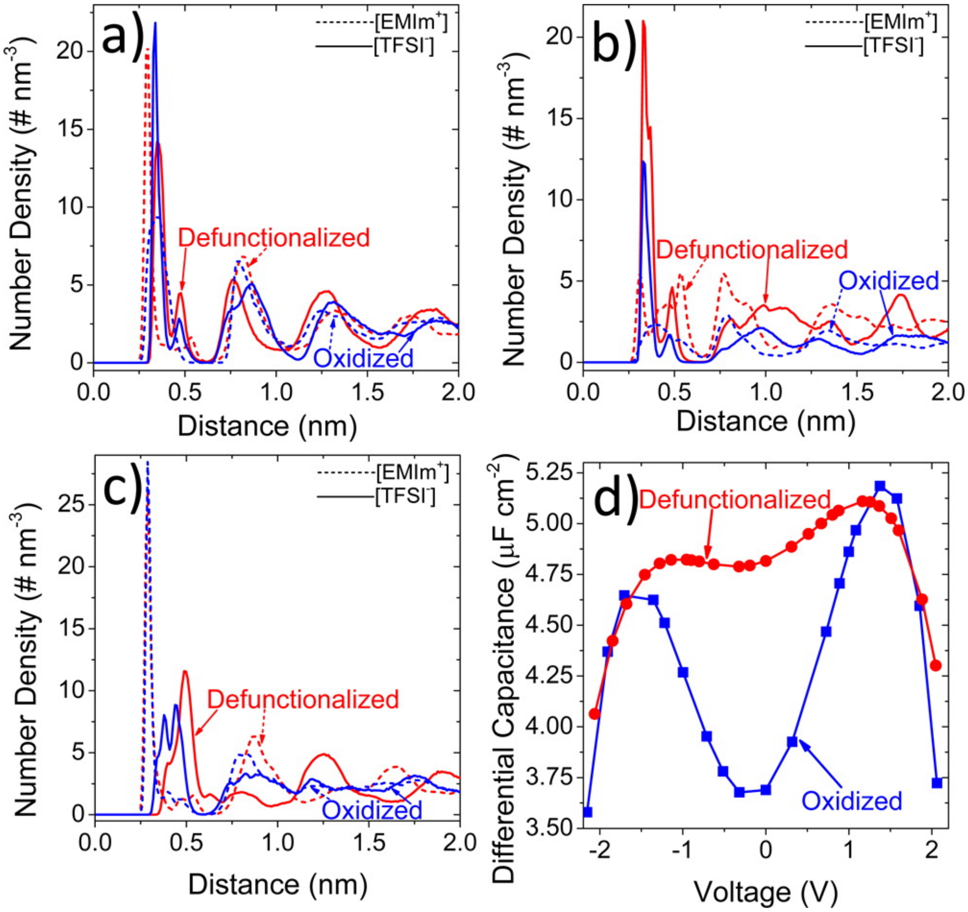

Figure 6.6 MD simulations of ion number densities for nonporous electrodes under (a) neutral potential, (b) +1.00 V applied potential, and (c) −1.00 V applied potential. (d) Differential

capacitance as a function of potential for defunctionalized/oxidized graphene. Integral $C_{sp}$= 4.89 μF cm$^{-2}$ for defunctionalized graphene and 4.31 μF cm$^{-2}$ for the oxidized surface.

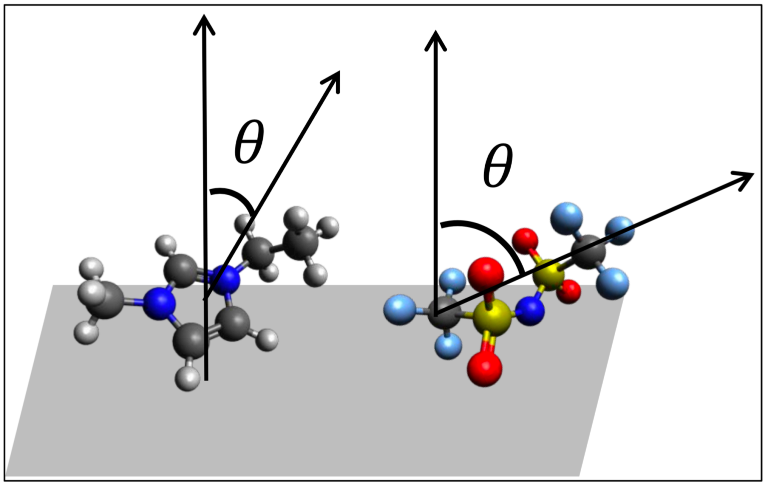

Figure 6.7 Orientation angles of (a) [EMIm$^+$] and (b) [TFSI$^-$].

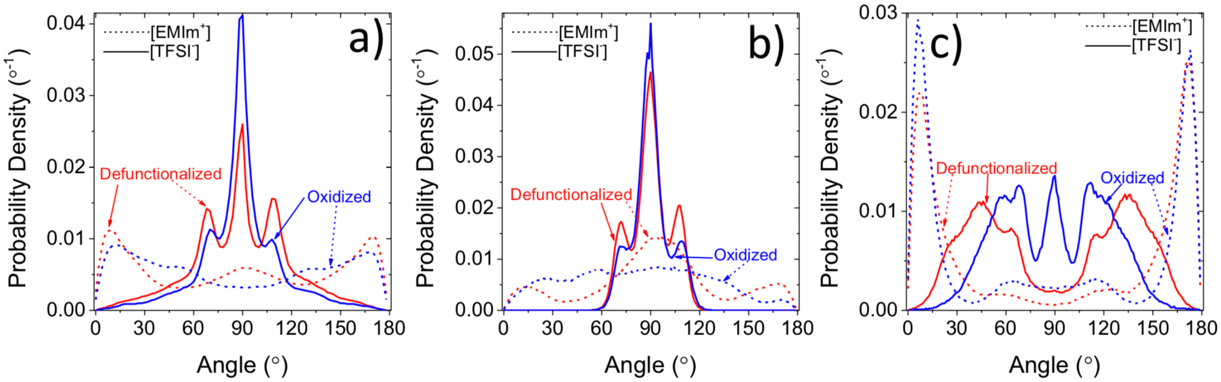

Figure 6.8 MD simulation of orientation angles of cations and anions on planar graphene electrode under (a) 0.00 V, (b) +1.00 V, and (c) −1.00 V.

After oxidization, the first peak of [EMIm$^+$] shifts away from the surface and becomes less intense, while the peak of [TFSI$^-$] draws closer to the surface and becomes more prevalent. Since

[$\text{EMIm}^+$] leaves the surface, its orientation is more evenly distributed after oxidization. [$\text{TFSI}^-$] lies parallel ot the surface with a close-packed arrangement.

While the counter-ion ([$\text{TFSI}^-$]) maintains a similar orientation distribution at a positively charged surface (+1.00 V, corresponding to surface charge density of 4.0 μC $\text{cm}^{-2}$), its number density decreases (Figure 6.6(b)). The first co-ion ([$\text{EMIm}^+$]) peak is pushed out of the first ion layer and creates a more disperse orientation. At a negatively charged surface (−1.00 V, corresponding to surface charge density of −4.0 μC $\text{cm}^{-2}$), the first number density peak and ion orientations remain unchanged for the [$\text{EMIm}^+$] counterion (Figure 6.6(c)). However, the first peak of [$\text{TFSI}^-$] is much closer to the oxidized surface than the defunctionalized electrode. It is accompanied by corresponding orientation distribution changes: a 90° peak indicates a parallel arrangement of [$\text{TFSI}^-$] ions with respect to the surface. Therefore, the hydroxyl group decreases the capacitance of negative electrodes by lowering counter-ion accumulation densities, and decreases that of positive electrode by attracting more co-ions into the electrosorbed layer. As shown in Figure 6.6(d), the capacitance of oxidized graphene is lower than the defunctionalized graphene, especially at low potentials. Electrostatic interaction likely dominates the electrode-ion interaction at charged surfaces, and subsequently decreases contribution from functional groups. These results agree well with the electrochemical experiments on GNP electrodes, which also shows higher $C_{sp}$ for defunctionalized surfaces.

### 6.3.2 Capacitive performance of solvated ionic liquids on nonporous carbons

In section 6.3.1, we discussed the effects of surface hydroxylation on the performance of supercapacitors when the electrolyte is a neat ionic liquid. In this section, we will study the effects of surface hydroxylation when ionic liquids are solvated in acetonitrile. Figure 6.9 shows the comparable experimental electrochemistry results for pristine graphene and oxidized graphene electrode, as normalized by the accessible SSA of each active material, in solvated organic salt electrolytes. The low-rate sweep of [EMIm$^+$][TFSI$^-$] solvated in ACN (Figure 6.9(a)) shows greater charge storage capacity of the defunctionalized pristine graphene electrode compared to the hydroxyl-rich oxidized electrode. This behavior holds true over the entire potential sweep range; Figure 6.9(b) shows approximately 3 μF cm$^{-2}$ (roughly 30%) higher charge storage density values for pristine graphene vs oxidized graphene. As described by the EIS-derived Nyquist plot (Figure 6.9(c)), the dynamics of [EMIm$^+$][TFSI$^-$] in ACN are similar for both pristine graphene and oxidized graphene, with only a slight difference in the ionic impedance near the “knee” frequency region. In that regime, [EMIm$^+$][TFSI$^-$] showcases less impedance during electrosorption onto pristine graphene electrodes. However, the differences in dynamics are negligible in the low-frequency regime (where capacitive contributions to impedence are more dominant). This suggests that the equilibrium number of ions that electrosorb on the surface, rather than intrinsically different dynamics, primarily account for the improved performance of the pristine graphene over its hydroxylated counterpart.

As shown in Figure 6.9(d), the [TEA$^+$][BF$_4^-$]/ACN electrolyte exhibits similar behavior and showcases higher capacitance on the pristine graphene compared to the oxidized graphene. The difference, as measured across the entire CV sweep range (Figure 6.9(e)), shows a more significant increase in charge storage density for defunctionalized electrodes compared to the aforementioned [EMIm$^+$][TFSI$^-$]/CAN system. Furthermore, both pristine graphene and oxidized graphene shows better performance on positive electrodes than negative electrodes of each respective system. This property is also more apparent than in the [EMIm$^+$][TFSI$^-$]/ACN-based electrolyte system. Electrolyte dynamics (Figure 6.9(f)) shows a slightly higher change transfer resistance for OG and suggested that increased resistance in the system stemmed from hydroxylated surface groups. While the “knee” frequency regions for both electrodes are similar, the oxidized electrodes exhibit slightly higher impedance in the low-frequency, purely capacitive region.

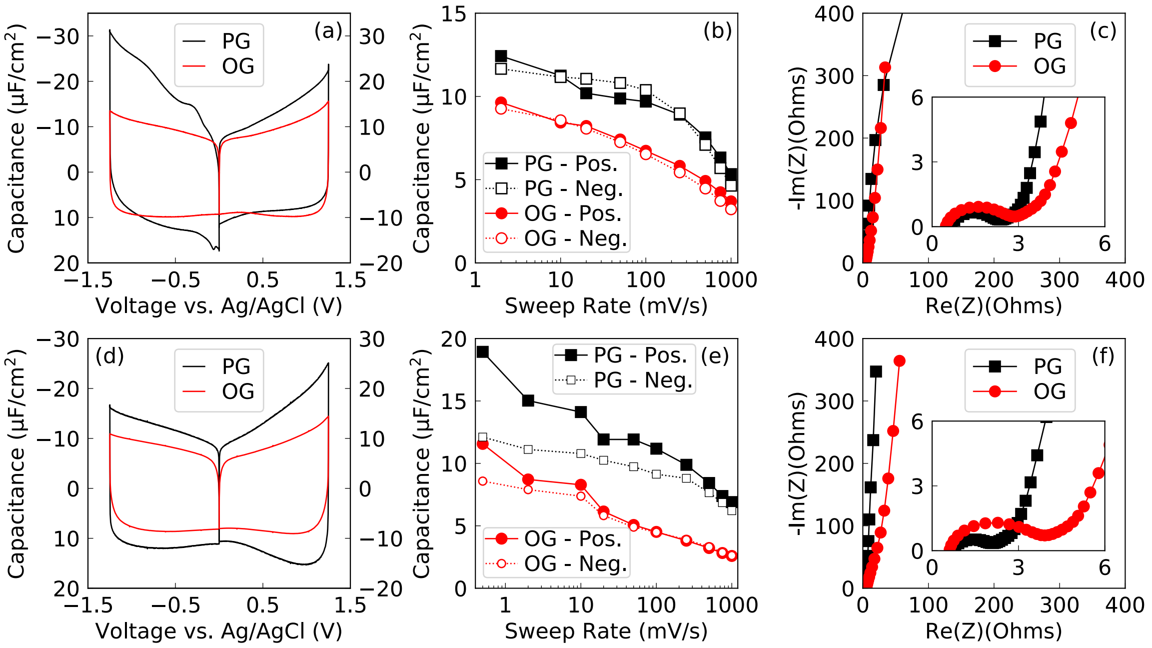

Figure 6.9 (a) Cyclic voltammogram sweep of pristine (PG) and oxidized (OG) graphene nanoplatelet electrodes in [EMIm$^+$][TFSI$^-$]/ACN at 2 mV s$^{-1}$. (b) Rate handling comparison for individual positive and negative electrodes for PG and OG in [EMIm$^+$][TFSI$^-$]/ACN in the 2 mV s$^{-1}$ – 1000 mV s$^{-1}$ sweep range. (c) Nyquist impedance plot that compares electrosorption dynamics of [EMIm$^+$][TFSI$^-$]/ACN in PG and OG. (d) 2 mV s$^{-1}$ CV sweep of PG and OG in [TEA$^+$][BF$_4$$^-$]/ACN electrolyte. (e) Range of CV sweeps for PG and OG in [TEA$^+$][BF$_4$$^-$]/ACN. (f) Nyquist impedance plot for PG and OG in [TEA$^+$][BF$_4$$^-$]/ACN.

The MD-derived computational comparisons of capacitance between pristine graphene and oxidized graphene electrode are shown in Figure 6.10. Note that all electrode potentials from MD simulations are relative to the potential of zero charge (PZC). In agreement with experimental electrochemistry results, the oxidized graphene always yields lower differential capacitance than the pristine graphene for both electrolytes. We also observe higher capacitance in the positive potential range than in the negative potential range. In both electrolytes, the size of anion is smaller than cation, which results in a thinner electrical double layer at the anode compared to that at the cathode, and yields higher capacitance at the anode.[84,179] In addition, the differential capacitance discrepancy between pristine graphene and oxidized graphene is more pronounced at positive potentials than at negative potentials. This is particularly apparent for the [TEA$^+$][BF$_4^-$]/ACN system: the differential capacitance is quite similar at potential below −0.5 V. This indicates that the anode is more significantly affected by the hydroxyl groups than the cathode.

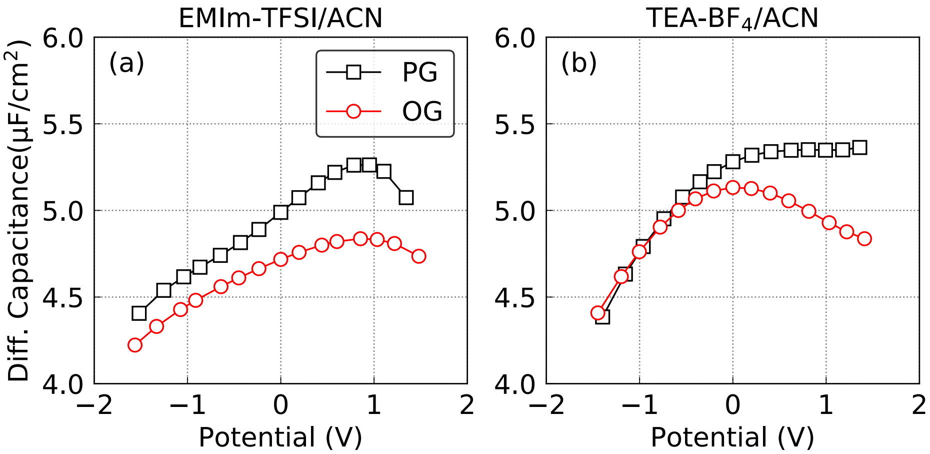

Figure 6.10 Differential capacitance of (a) [EMIm$^+$][TFSI$^-$]/ACN and (b) [TEA$^+$][BF$_4^-$]/ACN.

We also examined the effects of hydroxyl patterns on the capacitance. As shown in Figure 6.11, regularly and randomly patterned oxidized graphene surfaces have very similar differential capacitance, but regularly distributed oxidized graphene shows slightly lower capacitance than the randomly distributed surface in both electrolytes. This is likely to be caused by the lower ion accessibility to the patterned oxidized surfaces.[151] The results for oxidized graphene in this section are averaged results from both regularly patterned and randomly distributed oxidized graphene.

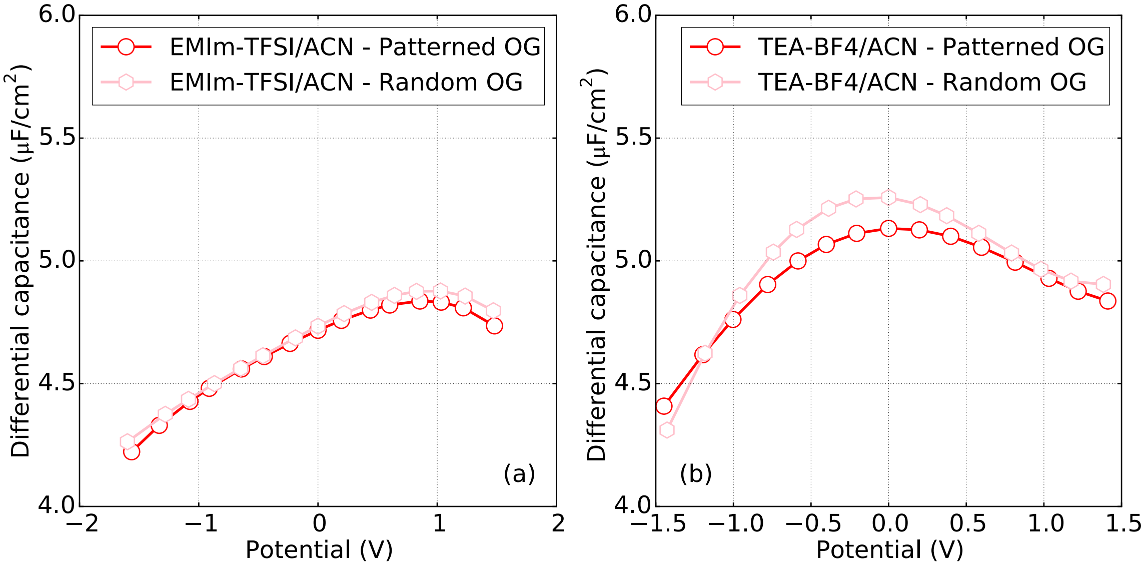

Figure 6.11 Differential capacitance of (a) $[EMIm^+][TFSI^-]$/ACN and (b) $[TEA^+][BF_4^-]$/ACN on hydroxylated graphene with regular pattern and random pattern.

Comparisons of the experimental results (Figure 6.9) with computational findings (Figure 6.10) highlight certain differences between experimental and MD-derived takeaways. In particular, we noticed that the experimental capacitance at slow sweep rates is two to three times higher than the MD-calculated capacitance. Certain intrinsic differences between the model and the experimental configuration most likely account for these deviations. Our MD systems represent graphene nanoplatelet surfaces as perfect basal planes. We incorporate hydroxyl groups on these (initially) flawless surfaces to simulate oxidized nanoplatelets. The experimental counterparts include additional structural factors that might affect capacitance but are convoluted, difficult to identify and quantify, and, therefore, essentially impossible to be implemented in our simulation model to the same extent. First, nanoplatelets are multilayered graphene flakes, and feature edges and surface curvature, which might yield higher capacitance.[63,180] Second, assembly of platelet flakes into bulk binder-bound electrode films may create ion confinement in the form of interparticle slits. Previous results have demonstrated significant capacitance increases in cases of matching electrolyte and micropore dimensions.[82,98] Finally, our simulation model used the fixed charge method, where net charges were evenly distributed on the surface atoms. A constant potential method, where each atomic charge is permitted to fluctuate according to its local environment, might yield a more accurate representation of the potential distribution of the system.[35] In this and the following section, instead of quantitatively predicting the capacitance of oxidized graphene, we focus more on discussing the qualitative change in capacitance due to surface oxidization.

### 6.3.3 EDL structure of solvated ionic liquids on nonporous carbons

To understand the capacitance behavior in section 6.3.2, in this section, we will look into the EDL structure of the electrolytes on the pristine and oxidized graphene. Figure 6.12 shows number densities of both electrolytes on pristine graphene and oxidized graphene at PZC. The PZC of [EMIm$^+$][TFSI$^-$]/ACN electrolyte dropped from 0.05 V to −0.09 V after hydroxylation. Similarly, the [TEA$^+$][BF$_4^-$]/ACN electrolyte has a PZC of 0.19 V on pristine graphene, and decreased to 0.03 V on the oxidized graphene. The decrease of PZC denotes the drop of excess charge in the EDL, indicating higher affinity of anions to the oxidized surface. In addition, hydroxylated surfaces attract more anions, and bring electrolyte species closer to the surface (Figure 6.12(c-d)), likely through the interaction between the hydroxyl groups and the polar F atoms in the anions. However, the cations behave differently in these two electrodes. [EMIm$^+$] has very similar distribution on both surfaces, whereas [TEA$^+$] was observed to have a much higher peak at 0.5 nm on the oxidized surface. The [TEA$^+$] layer at such a distance is likely formed due to the attraction of the first [BF$_4^-$] layer at around 0.4 nm (Figure 6.12(d) in SI), whose peak is significantly higher on the oxidized graphene than on the pristine graphene. Since the oxidized graphene accommodates higher ion concentrations in EDL, ACN is less concentrated in the first layers at PZC.

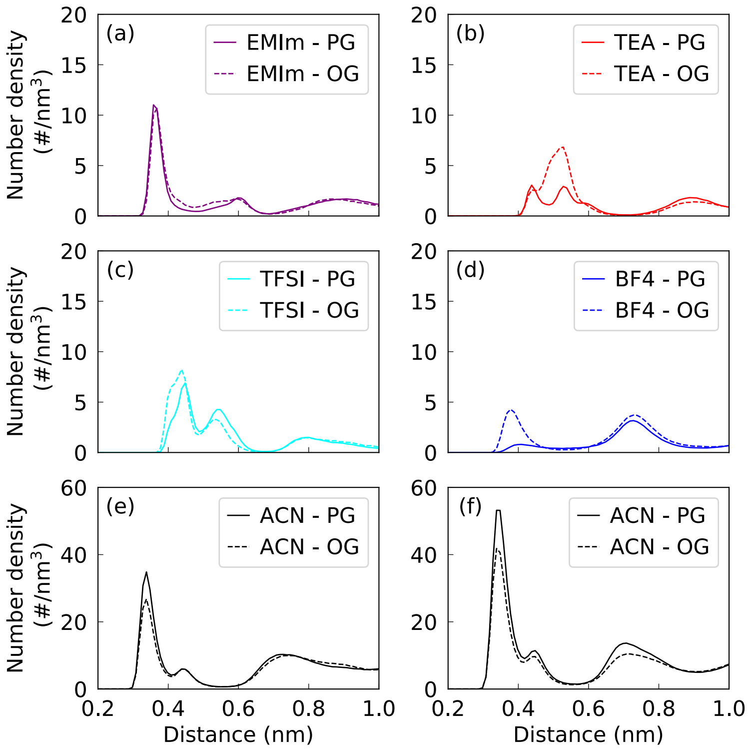

Figure 6.12 Number densities of the two electrolytes at PZC: [EMIm$^+$][TFSI$^-$]/ACN (a, c, e) and [TEA$^+$][BF$_4^-$]/ACN.

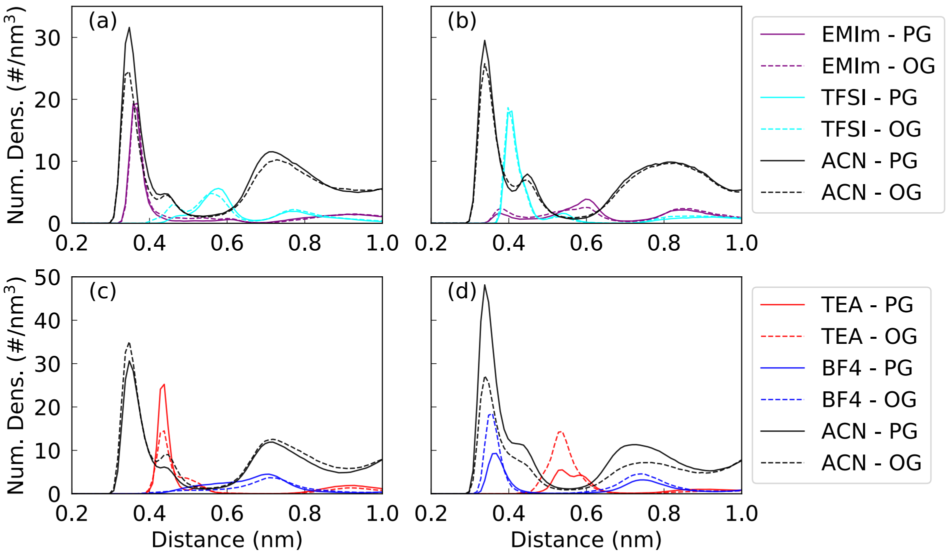

Figure 6.13 Number densities of [EMIm$^+$][TFSI$^-$]/ACN on (a) negative electrodes (-5 μC cm$^{-2}$), and (b) positive electrodes (5 μC/cm$^{-2}$). Number densities of [TEA$^+$][BF$_4$$^-$]/ACN on (c) negative electrodes (-5 μC/cm$^{-2}$), and (d) negative electrodes (5 μC/cm$^{-2}$).

The comparison of number densities at charged surfaces is shown in Figure 6.13. Of note, these number densities also contain contributions from PZC. To exclude these biases, Figure 6.14 shows the relative number densities of the two electrolytes on charged surfaces by subtracting their corresponding number densities at PZC. Figure 6.14(a-b) show the relative number densities of [EMIm$^+$][TFSI$^-$]/ACN. By comparison, the cation shows relatively similar distribution between the pristine graphene and oxidized graphene, whereas the anion appears to have observable differences. More specifically, on the negative electrodes, anions act as co-ions and deplete from the surface during charging. Thus, the anion curves have negative valleys in Figure 6.14(a). While the depths of the anion valleys are similar, the anion is much closer to the oxidized graphene than to the pristine graphene. As shown in Figure 6.13(a), there is an anion peak at around 0.45 nm, which impedes efficient charge screening and decreases capacitance of the oxidized graphene electrode. On the positive electrodes, the anion has slightly low peak heights, but is also slightly closer to the electrode surface. This is likely due to the competition between strong interaction between anion and the surface hydroxyls and the steric hindrance introduced by these hydroxyls. While the former draws the anion closer to the surface, the latter repels some anions from the EDL.[151] The overall results as shown by the capacitance curve is that the capacitance decreases.

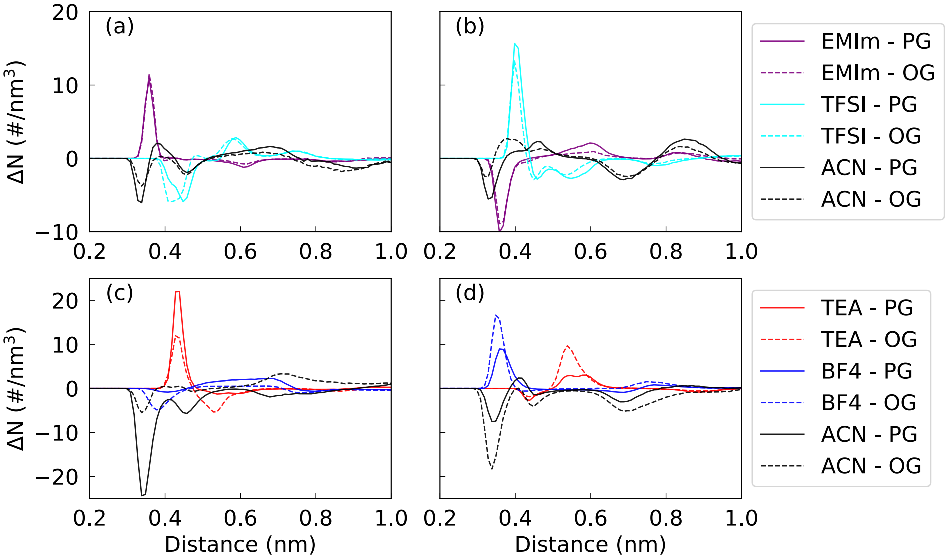

Figure 6.14 Number densities relative to PZC: $[EMIm^+][TFSI^-]$/ACN on (a)negative electrodes (-5 μC cm$^{-2}$) and (b) positive electrodes (5 μC cm$^{-2}$); $[TEA^+][BF_4^-]$/ACN on (c) negative electrodes (-5μC/cm$^{-2}$) and (d) positive electrodes (5μC/cm$^{-2}$).

The EDL structure of the $[TEA^+][BF_4^-]$/ACN system is shown in Figure 6.14(c-d), where both cation and anion behave differently on the pristine graphene and oxidized graphene. Figure 6.14(c) shows that the counter-ion ($[TEA^+]$) have lower peak heights after hydroxylation on negatively charged surfaces. The decreased $[TEA^+]$ peak on the oxidized graphene surface is likely a result of steric hindrance created by the surface hydroxyls, which may be more significant for big ions like [TEA$^+$] than for smaller ions within the scope of this study. The effect of steric hindrance could also be inferred from the more dispersed distribution of [TEA$^+$] between 0.4–0.6 nm in Figure 6.13(c). Accordingly, the co-ion has deeper valley on the oxidized graphene, meaning that less co-ions are presented in the EDL. On the contrary, Figure 6.14(d) shows that the peak of counter-ion [BF$_4^-$] nearly doubled after hydroxylation and the peak is also slightly closer to the surface. Anion has a peak height around 10 # nm$^{-3}$ at 0.38 nm on the pristine graphene, which, considering the small size of [BF$_4^-$], is far from saturation. Thus, the anion-affinitive oxidized surface has the capability to attract more anions to its interface. This intensified counter-ion layer also strengthens the co-ion ([TEA$^+$]) layer at 0.53 nm. As a result, both counter-ions and co-ions have higher concentrations in EDL on the oxidized graphene than on the pristine graphene. The synchronous increase or decrease of cation and anion complicate things, make it hard to interpret the capacitance from EDL structure.

To better decode the charge storage mechanism in the TEA-BF$_4$/ACN systems, the charge screening factor[181] was calculated:

$$f_s(z) = -\frac{1}{\sigma}\int_0^z \Delta\rho_e(u)\,\mathrm{d}u \tag{6.1}$$

where $\sigma$ is the surface charge density, while $\Delta\rho_e(u)$ is the variation of charge density as the surface charge density changed from 0 to $\sigma$. If charge overscreening happened at the interface, $f_s$ will exceed 1. As described by Kornyshev *et al*[181], overscreening is pronounced at a small voltage and, at higher potentials, is gradually replaced by the crowding of counter-ions until complete lattice saturation (at very large voltages).

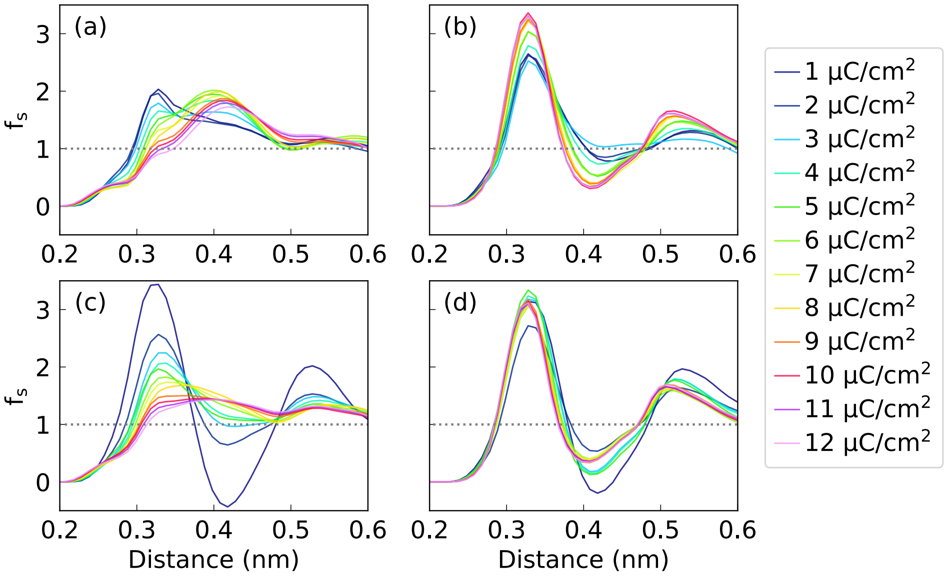

Figure 6.15 Screening factor as a function of distance to (a) negative pristine electrode surface, (b) positive pristine surface, (c) negative oxidized surface, and (d) positive oxidized surface. The legend denotes the absolute surface charge density of each curve.

The charge screening factors with different surface charge densities can be found in Figure 6.15. Let's first look at the positive electrodes (Figure 6.15(b) and (d)), the peak first increases ads charging begins, but then decreases as the surface charge density becomes large, which matches aforementioned Kornyshev's theory.[181] Because the oxidized surface is more occupied with counter-ions, the crowding of counter-ions happens at a lower surface charge density on the oxidized surface, which leads to earlier drop of peak height on the oxidized surface as the surface charge increases. As a result, the screening factor is higher on the oxidized surface than on the pristine graphene when the surface charge density is low, and lower when the surface charge is high. On negative electrodes (Figure 6.15(a) and (c)), both pristine graphene and oxidized graphene exhibit decreased peak heights at 0.32 nm as charging processes, where the oxidized graphene shows more substantial drops. According to Figure 6.13, there are no significant counter-ion or co-ion peaks at 0.32 nm, but only ACN has high peaks at this distance. Considering the high dipole moment of acetonitrile (3.92 D), the distribution and orientation of ACN molecules near the electrode surface may play an important role on charge screening, and hence capacitance. Besides the decreasing first peaks in Figure 6.15(a) and (c), there are also nonnegligible peaks at 0.4 nm, which are the results of the overcreening of counter-ions at such distance. For both pristine and oxidized graphene, the peak at this distance shows an initial upward trend and followed by a downward trend, in response to growing surface charge densities.

In an effort to further decouple the structure of ACN layer on electrode surfaces, the orientation order parameter is introduced to study the alignment of ACN along the direction perpendicular to the surface:

$$P_2(cos\theta) = \frac{1}{2}(3\langle cos^2\theta \rangle - 1) \tag{6.2}$$

Where the angle $\theta$ is formed by the normal vector of the surface and the vector from methyl C to N in ACN. <…> denotes ensemble average. The range of orientation order parameter is from -0.5 to 1. If $P_2(cos\theta)$ is -0.5, ACN lies parallel to the surface; if $P_2(cos\theta)$ is 0, ACN adopts random orientation distribution; if $P_2(cos\theta)$ is 1, ACN lies perpendicular to the surface. Figure 6.16 in SI shows the order parameter as a function of distance to the surface. Each curve starts with a value around -0.5 near the surface, suggesting a parallel orientation of ACN with respect to the surface, and then oscillates between negative and positive values, and, finally, converges to zero. This behavior implies that the ACN molecules orient themselves according to their local environments, resulting in local potential drop.

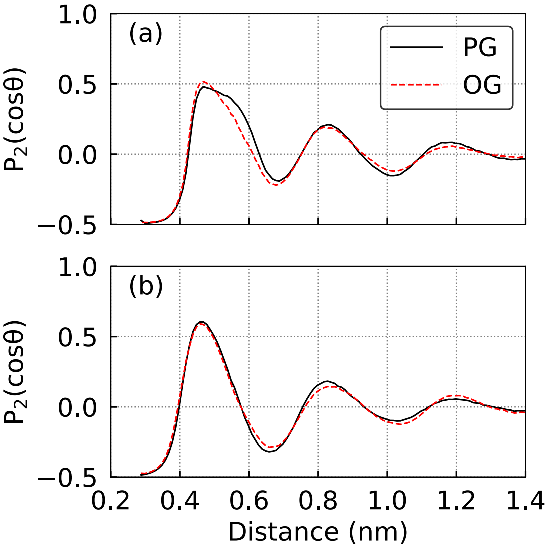

Figure 6.16 Order parameter $P_2(\cos\theta)$ of ACN on (a) negative electrode (-5 μC $cm^{-2}$) and (b) positive electrode (5 μC $cm^{-2}$).

To quantify the potential drop induced by ACN, we decomposed the total spatial charge in equation (3.4) into 2 parts: IL charge density and solvent charge density, respectively.

$$\rho_e = \rho_e^{IL} + \rho_e^{ACN} \tag{6.3}$$

Then equation (3.4) can be rewritten as:

$$\emptyset(z) = \left(-\frac{1}{\varepsilon_0}\int_0^z (z-z')\rho_e^{IL}(z')\mathrm{d}z' - \frac{\sigma}{\varepsilon_0}z\right) + \left(-\frac{1}{\varepsilon_0}\int_0^z (z-z')\rho_e^{ACN}(z')\mathrm{d}z'\right) \tag{6.4}$$

In equation (6.4), the total potential drop is the sum of partial potential drop from IL and ACN. Figure 6.17 shows the potential contributions generated from ACN with different surface charges.

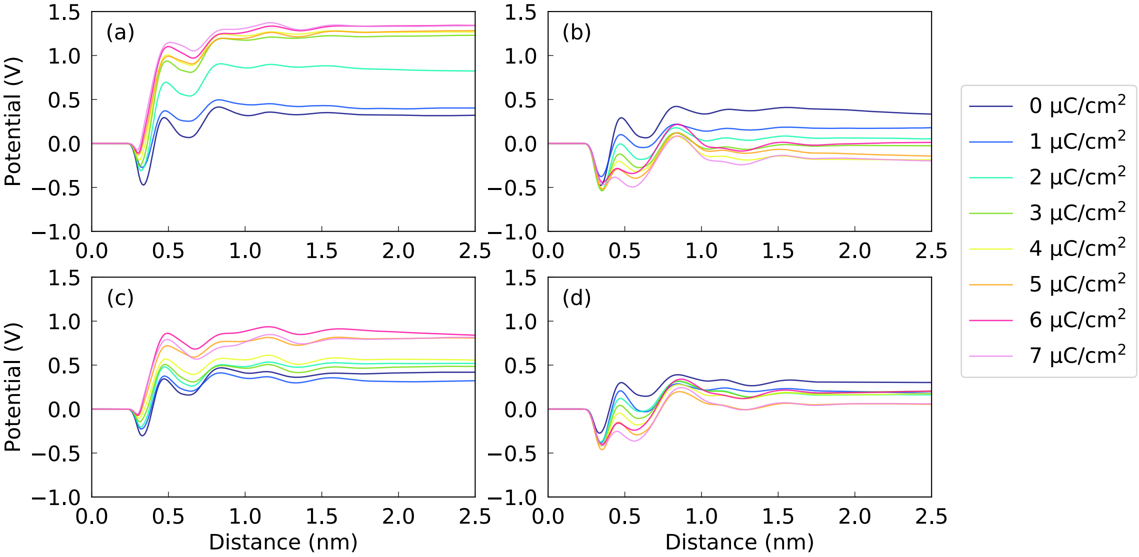

Figure 6.17 Partial potential distribution of ACN on the pristine graphene with (a) positive surface charge, and (b) negative surface charge. Partial potential distribution of ACN on the oxidized graphene with (c) positive surface charge, and (d) negative surface charge. The legend denotes the absolute surface charge density of each curve.

The partial potential drops from IL and ACN with regard to different surface charge densities were summarized in Figure 6.18. Figure 6.18(a) shows the partial potential drop contributed by IL, where the potential drops on the oxidized surface are closer to 0. The specific capacitance is directly related to the inverse of the potential drop:

$$C = \frac{\sigma}{\varphi} \tag{6.5}$$

where $\sigma$ is the surface charge density and $\sigma$ is the potential drop. Based on this, the capacitance contributed purely by IL is higher on the oxidized surface than on the pristine surface. However, the presence of ACN in EDL reverses the relative total capacitance.

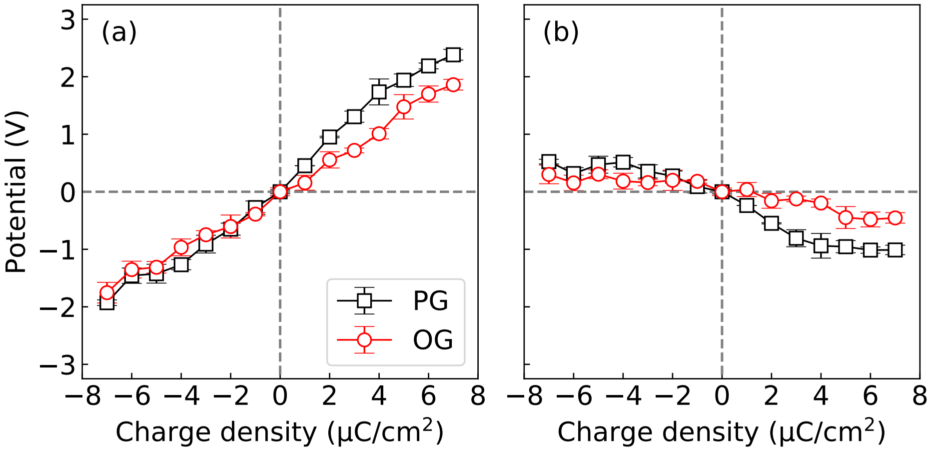

Figure 6.18 Partial potential drop contributed by (a) IL and (b) ACN.

As shown in Figure 6.18(b), the potential drop contributed by ACN has the opposite sign to the potential drop by IL, which reduces the absolute value of the total potential drop and thus enlarges capacitance according to equation (6.5). Put in another way, the electrode could store the amount of charge at a lower potential, yielding higher capacitance. Previous findings have also shown that adding appropriate solvents to the ionic liquids electrolyte may help to increase the capacitance.[66,69,182] The work presented herein confirmed the integral role of the distribution and orientation of polar solvent species near electrode surfaces. Furthermore, the total capacitance has both contributions from IL and ACN. While the pristine surface has lower partial capacitance from IL, its total capacitance is higher, especially at positive potentials. From Figure 6.16, we know that the orientation distribution of ACN does not differ obviously between the pristine graphene and the oxidized graphene. The reason that the pristine graphene has much higher potential contribution from ACN at positive electrode is attributed to difference in ACN concentrations. As shown in Figure 6.13(d) and Figure 6.14(d), the positive oxidized surface accommodates more ions than the pristine surface, squeezing out ACN molecules, and the ACN peak is almost halved. Similarly, the negative electrodes adsorb bulky cations ([TEA$^+$]), leading to decreased ACN concentrations. As a result, the potential drop yielded by ACN on these surfaces is less prominent.

Our approach comprehensively dissected the structure of double layers to decouple the relative influence of key factors on capacitance of pristine and oxidized graphene. While the anion played the major role in the drop of capacitance of [EMIm$^+$][TFSI$^-$]/ACN after hydroxylation, the capacitive behavior of [TEA$^+$][BF$_4^-$]/ACN involves the participation of both IL and solvents. ACN exhibits an oscillatory orientation distribution across the EDL and significantly influences capacitance, especially on positive electrodes.

### 6.3.4 Ion and solvent dynamics of solvated ionic liquids on nonporous carbons

In previous two sections, we mainly talk about the effects of surface hydroxylation on the EDL structure and capacitance. We are also interested to examine the effects of hydroxylation on the ion and solvent dynamic at the interface. Since the ions and solvent form layered structure near electrode surfaces, heterogeneity of ion and solvent dynamics can be observed in the direction perpendicular to the electrode surface. Ion density is conventionally considered a major factor that influences the ion dynamics. Subsequently, in order to find a way to boost charging dynamics, previous studies have correlated ion density in slit pores with diffusion coefficients.[183,184]

In an effort to more clearly understand the ion and solvent dynamics, we divided the simulation channel into different regions. Three regions were defined based on the number densities: interfacial, transitional, and bulk-like. Figure 6.19 shows the scheme of dividing simulation box of [TEA$^+$][BF$_4^-$]/ACN on the charged pristine graphene. The average location representing each region is calculated by

$$z_{avg} = \frac{\int_{z0}^{z1} z\rho_n(\mathrm{z})\mathrm{dz}}{\int_{z0}^{z1} \rho_n(\mathrm{z})\mathrm{dz}} \tag{6.6}$$

where $\rho_n$ is the center-of-mass number density.

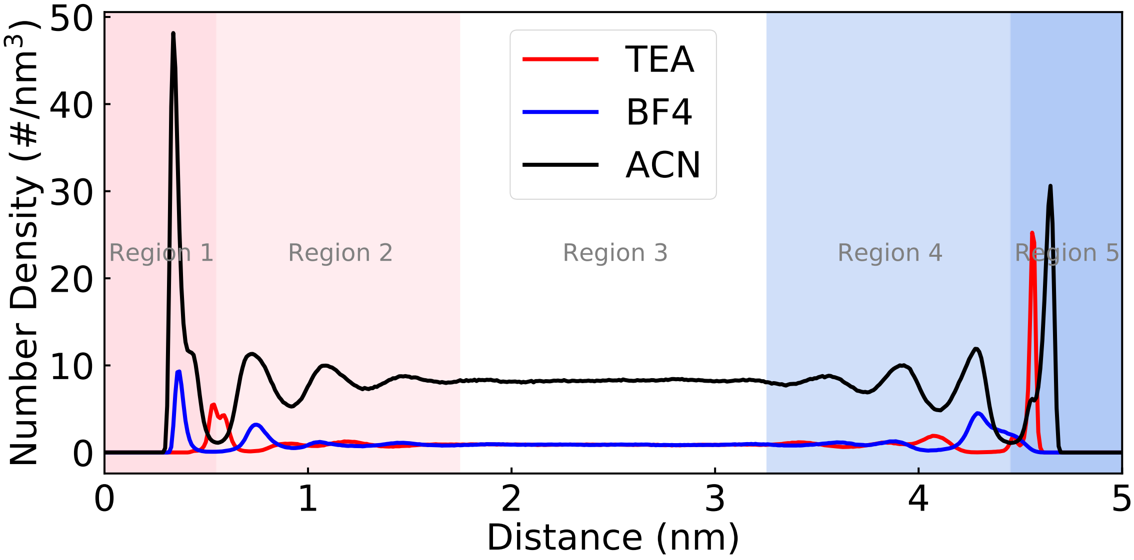

Figure 6.19 Division of solvent regions by its number density profile. Region 1 and 5 are interfacial regions; region 2 and 4 are transitional regions; region 3 are bulk-like region. The surface charge densities for this system are ±5 μC cm$^{-2}$.

The diffusion coefficients in each region were computed using the Einstein relation, and only the lateral mean square displacement (MSD) was considered. These 2-D self-diffusion coefficients can be obtained using the following formula:

$$D = \lim_{t\to\infty} \frac{\langle (\boldsymbol{r}(t) - \boldsymbol{r}(0))^2 \rangle}{4\boldsymbol{t}} \tag{6.7}$$

where $\boldsymbol{r}(t)$ represents the lateral position at $t$. Note that since molecules may enter and leave each region, we only selected molecules that stayed in each region during the production run.

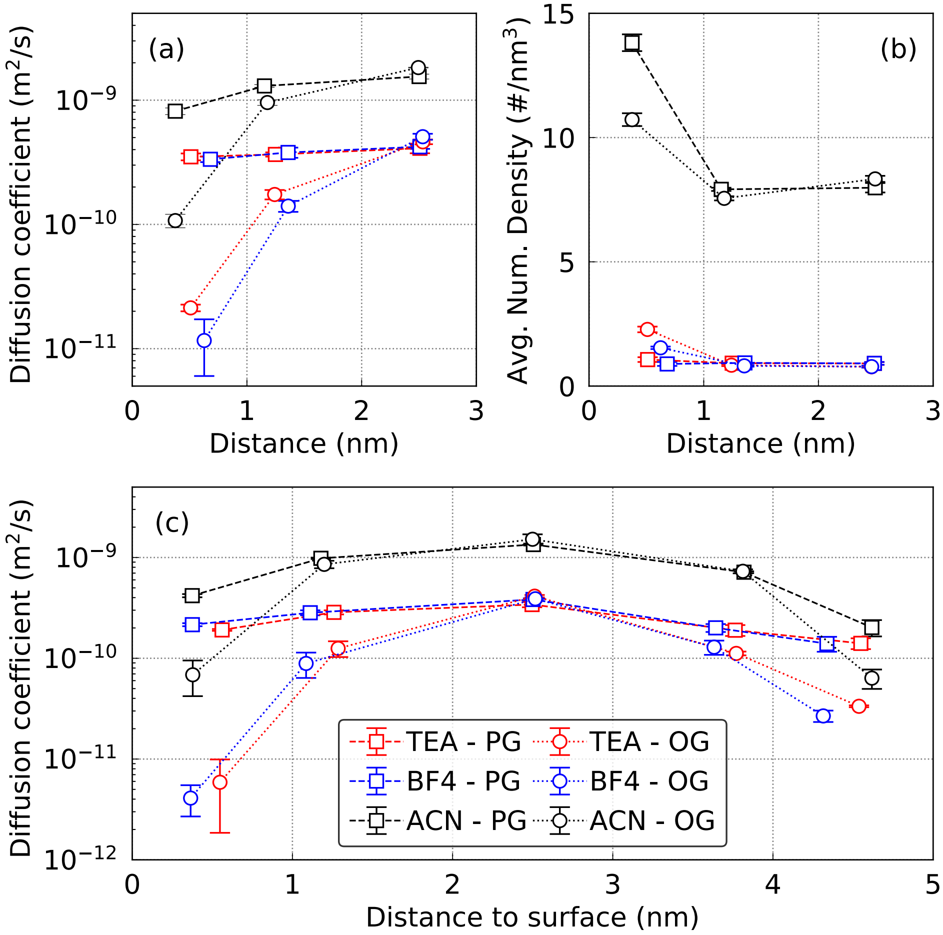

Figure 6.20 (a) Diffusion coefficients and (b) average number densities of [TEA$^+$][BF$_4^-$]/ACN at PZC. (c) Diffusion coefficients in different regions with surface charge densities of ±5 μC cm$^{-2}$ (left side is positively charged and right side is negatively charged).

As shown in Figure 6.20(a), the self-diffusion coefficients drop when ion/solvent approaches surface. This trend is more significant on the oxidized surface, as the diffusion coefficients in the interfacial region decrease by more than an order of magnitude compared with those in bulk-like region. As a comparison, the diffusion coefficients on the pristine graphene exhibit only slight decreases during the transition from bulk-like region to interfacial region. In addition, the diffusion coefficients of cation and anion are very similar, suggesting strong correlations between cation and anions. Figure 6.20(b) shows the average number densities in each region. In the interfacial region, the oxidized graphene brings ions closer to the surface, resulting in higher ion concentrations near the oxidized surfaces. These conditions prohibit fast ion dynamics. In the bulk-like region, as the number densities recover to bulk number densities, the diffusion coefficients are similar for both pristine and oxidized graphene. However, in the transitional region, even though the number densities are similar to bulk-like regions, the diffusion coefficients are still much lower than those in the bulk-like region. This suggests that a number of intricate factors that convolute the diffusive behavior of ion/solvent in the interface. It cannot be solely explained by the ion density, and both ion-ion and ion-wall interactions play an important role. Similar trends are observed when the surfaces are charged. As shown in Figure 6.20(c), ions that approach surfaces exhibit lower diffusion coefficients, and this trend is more obvious on OG.

The lateral diffusion coefficients presented above only illustrate how fast ions move in the directions parallel to the surface. However, the mobility of ions in the direction perpendicular to the surface is also important. To that end, the residence time autocorrelation functions examine the time scale during which ions/solvents remain within the interfacial region. The function was calculated using the following formula:

$$C_R(t) = \frac{\langle R(0)R(t)\rangle}{\langle R(0)R(0)\rangle} \tag{6.8}$$

where $R(t)$ is a binary function that equals to 1 if a molecule within the interfacial region at time 0 is also found in the interfacial region at time t, and 0 otherwise.

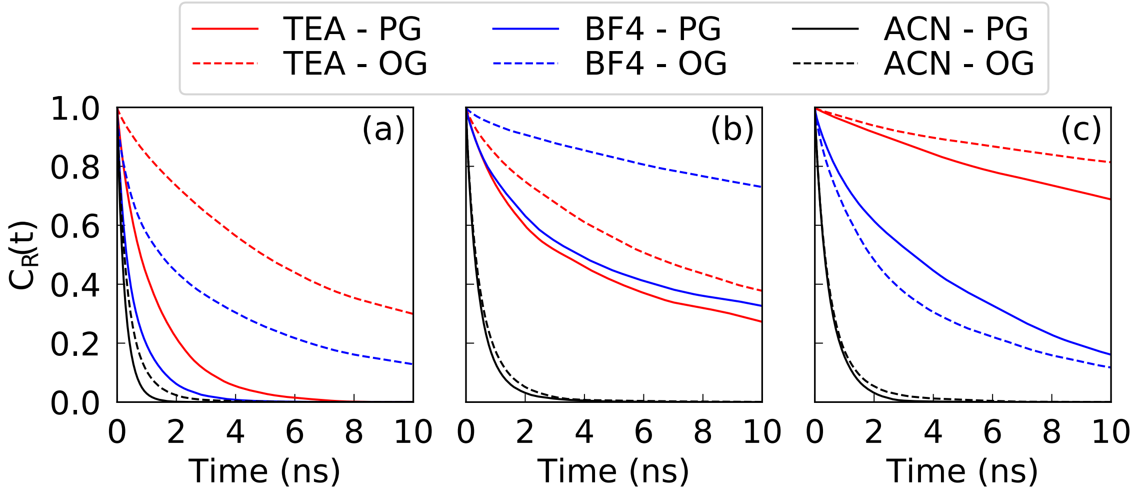

Figure 6.21 Residence time autocorrelation function of [TEA$^+$][BF$_4^-$]/ACN at (a) PZC, (b) positive electrode (5 μC cm$^{-2}$), and (c) negative electrode (-5 μC cm$^{-2}$).

Figure 6.21 shows $C_R(t)$ at PZC, positive electrode, and negative electrode, respectively. At PZC, [TEA$^+$] has higher residence time, as shown in Figure 6.21(a). Therefore, even though [TEA$^+$] has higher lateral diffusion coefficients than [BF$_4^-$], it is less mobile in the direction perpendicular to the surface. The curves of the oxidized graphene are higher than those of the pristine graphene, which indicates longer residence time and lower mobility for ions and solvent on the oxidized graphene. On charged surfaces, counter-ions always exhibit the longest residence time, indicating that they are strongly adsorbed by the electrodes, and reluctant to swap with ions in the transitional region. Moreover, the hydroxyl groups increase the residence time of counter-ions in the interfacial region. The dynamics results for [EMIm$^+$][TFSI$^-$]/ACN systems are similar, and can be found in Figure 6.22.

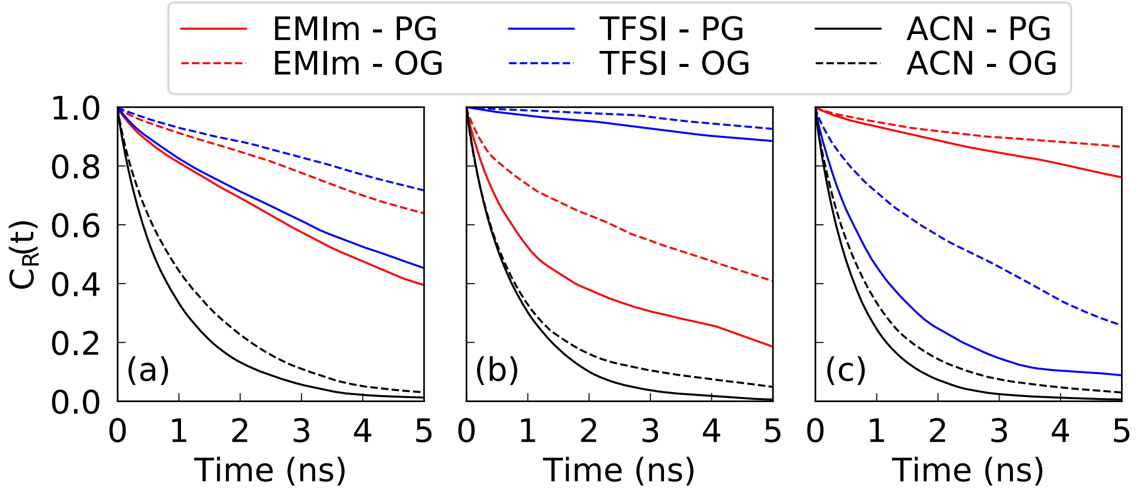

Figure 6.22 Residence time autocorrelation function for [EMIm$^+$][TFSI$^-$]/ACN (a) at PZC, (b) positive electrode (5 μC cm$^{-2}$), and (c) negative electrode (-5 μC cm$^{-2}$).

### 6.3.5 Neat ionic liquid confined in 0.8-nm slit-pores

In the following sections, we focus on the effects of surface hydroxylation on the performance of ionic liquids confined in CDCs. Ionic liquids with different cation sizes are studied: [EMIm$^+$][TFSI$^-$] and [OMIm$^+$][TFSI$^-$] respectively. In this section, we look into the case when the 0.8-nm CDCs are immersed in [EMIm$^+$][TFSI$^-$]. Cyclic voltammetry recorded significantly greater capacitance of oxidized CDC electrode with [EMIm$^+$][TFSI$^-$]. As shown in Figure 6.23(a), the oxygen-containing electrodes shows rectangular CV curves that are indicative of ideal capacitive behavior and stored 4.6 μF cm$^{-2}$ (67.7 F g$^{-1}$) at 50 mV s$^{-1}$. Conversely, ionic resistance distorted the CV profile for defunctionalized CDCs, and their $C_{sp}$ reaches only 1.4 μF cm$^{-2}$ (16.8 F g$^{-1}$) at the same sweep rate. Defunctionalized CDCs exhibit drastic capacitance decays over the entire 0.5–250 mV s$^{-1}$ CV sweep range (Figure 6.23(b)); oxidized pores clearly offer superior [EMIm$^+$][TFSI$^-$] rate handling abilities.

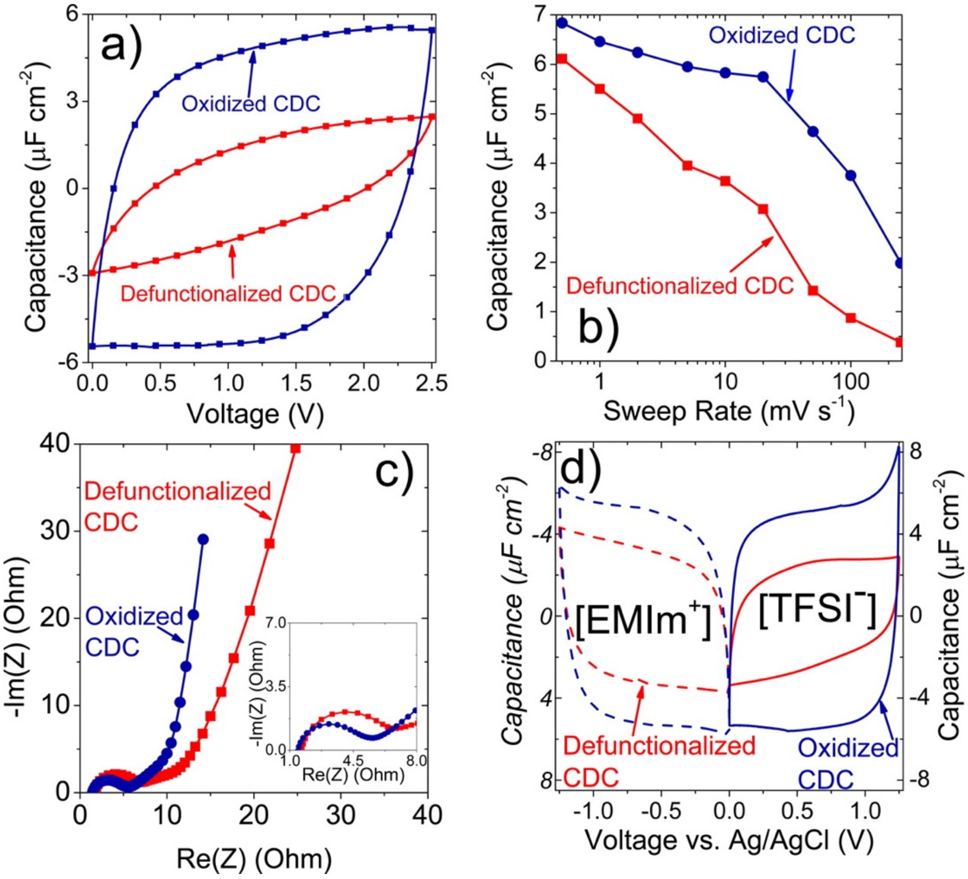

Figure 6.23 (a) Cyclic voltammetry plot for [EMIm$^{+}$][TFSI$^{-}$] at 50 mV s$^{-1}$ sweep rate. (b) Rate handling comparison of oxidized and defunctionalized pores. (c) Nyquist plot that compared ionic resistance differences. (d) A 3-electrode sweep conducted at 1.00 mV s$^{-1}$.

As shown in the EIS-derived Nyquist plot in Figure 6.23(c), oxidized pore surfaces significantly reduces ionic impedance of [EMIm$^{+}$][TFSI$^{-}$]. While the resistance contribution dominates the electrochemical impedance of defunctionalized CDC, oxidized CDCs become significantly more capacitive at mid-to-low frequencies. Although oxidized carbon has a lower intrinsic electrical conductivity than defect-free graphene,[185] this effect is not significantly pronounced in electrode films. The 4-point probe conductivity measurements showed that oxidized electrodes ($\sigma = 1.42 \pm 0.09$ S cm$^{-1}$) are only slightly more resistive than the defunctionalized films ($\sigma = 1.68 \pm 0.09$ S cm$^{-1}$).

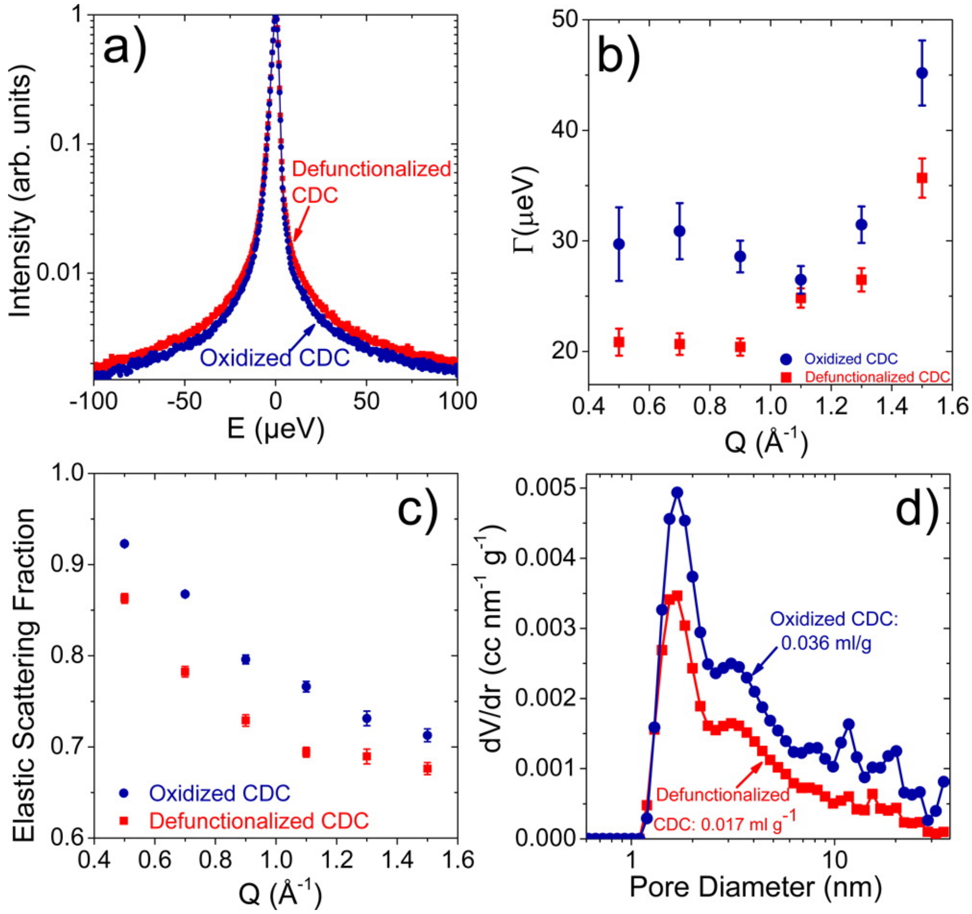

Figure 6.24 (a) QENS signal for pores 100% filled with [EMIm$^+$][TFSI$^-$]. (b) QENS signal width (boad component). (c) The fraction of elastic scattering in the QENS signal measured for the two systems. (d) N$_2$ sorption isotherm of the sample completely filled with [EMIm$^+$][TFSI$^-$].

EIS measurements, correspondingly, shows nearly identical equivalent series resistance for the two materials and suggests that poor ion exchange and transport limiting factor that hindered electrosorption in pristine CDCs. Three-electrode measurements (Figure 6.23(d)) investigate the standalone influences of cation and anions. While the trends resembled those for two-electrode cells, defunctionalized CDCs demonstrate significantly greater ionic resistance and ion sieving of the [TFSI⁻] anion than the [EMIm⁺] cation. Oxidized CDC does not show such asymmetry. The [TFSI⁻] anion shos the greatest rate limitation in defunctionalized pores, so its repulsion by defunctionalized surfaces more noticeably lowers $C_{sp}$ in annealed pores. This finding agrees with prior results.[161,168]

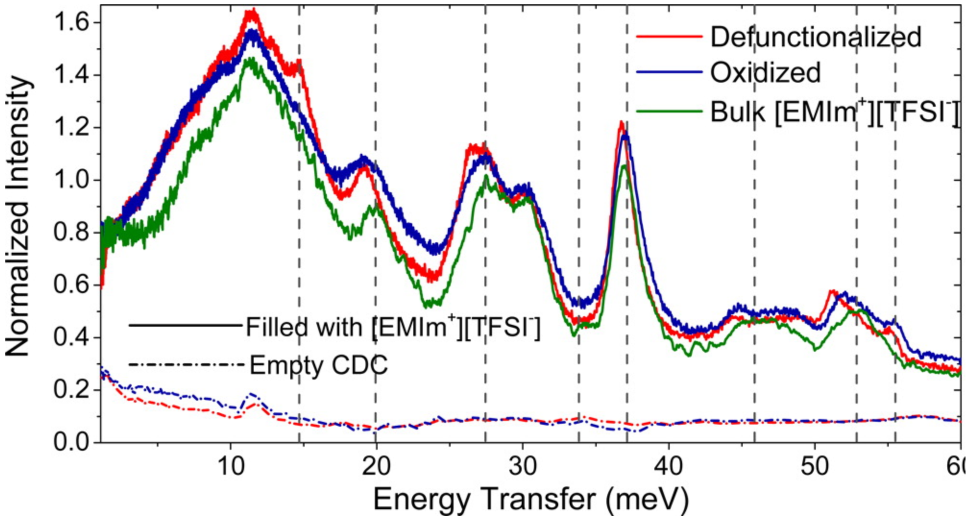

Figure 6.25 INS spectra obtained at 5 K on the empty and IL-filled pores.

In addition QENS measurements provide insights into the relative mobilities of [EMIm⁺][TFSI⁻] ions (more specifically, hydrogen-bearing cations) inside the uncharged CDC pores. As shown in Figure 6.24(a-b), the width of the QENS signal is systematically broader for ions confined in oxidized pores than that in defunctionalized pores, which indicates improved mobility and reduced resistance during self-diffusion of ions through ionophilic pores. The analysis of the elastic scattering fraction in the QENS signal (Figure 6.24(c)) indicates greater degree of scattering perceived as elastic for ions confined in oxidized pores. Porosimetry analysis of filled pores (Figure 6.24(d)) further confirmed the tight confinement of ions in both defunctionalized and oxidized CDCs: all subnanometer pores were filled with [EMIm$^+$][TFSI$^-$]. Moreover, INS measurements at 5 K provides information on the relative vibrational density of states (VDOS) of [EMIm$^+$][TFSI$^-$] in the bulk and confined states as well as VDOS of the used empty CDCs samples. As Figure 6.25 shows, all vibrational modes of IL confined in defunctionalized pores are lower than those in the oxidized CDCs. This suggests a more uniform local bonding environment and/or lower mobility of ion confined in defunctionalized pores.

Table 6.1 Summary of integral number densities confined in slit-pores

| Electropotential State | Material | Integral Number density / # nm$^{-2}$ | | | |
|---|---|---|---|---|---|
| | | [EMIm$^+$] | [TFSI$^-$] | Total | Ion Accumulation |
| Neutral | Defunctionalized | 1.96 | 1.84 | 3.80 | 0.12 |
| | Oxidized | 1.61 | 1.62 | 3.23 | -0.01 |
| Positive (+5.0 μC cm$^{-2}$) | Defunctionalized | 1.29 | 1.85 | 3.14 | -0.57 |
| | Oxidized | 1.25 | 1.94 | 3.18 | -0.69 |
| Negative (-5.0 μC cm$^{-2}$) | Defunctionalized | 1.98 | 1.33 | 3.31 | 0.64 |
| | Oxidized | 2.08 | 1.61 | 3.70 | 0.47 |

Subsequent MD simulations compare influences of hydroxyl groups in slit-pores. Figure 6.26 shows the ion number densities inside slit pores under neutral conditions (i.e., identical conditions as neutron scattering experiments). The peak heights of [EMIm$^+$] and [TFSI$^-$] decrease after oxidization. Especially, the cation peaks near 0.35 nm and 0.75 nm diminishes in the oxidized slit-pores. The angle distributions (Figure 6.26(d)) further suggest a vertical arrangement of [EMIm$^+$] with respect to oxidized slit surface. To quantify this effect, we integrate the number densities over the entire slit distance and obtain the integral number densities, shown in Table 6.1. The concentrations of [EMIm$^+$] and [TFSI$^−$] decreases by 18% and 12% respectively, after oxidization; oxidized pores exhibit 15% net lower filling densities than the defunctionalized ones.

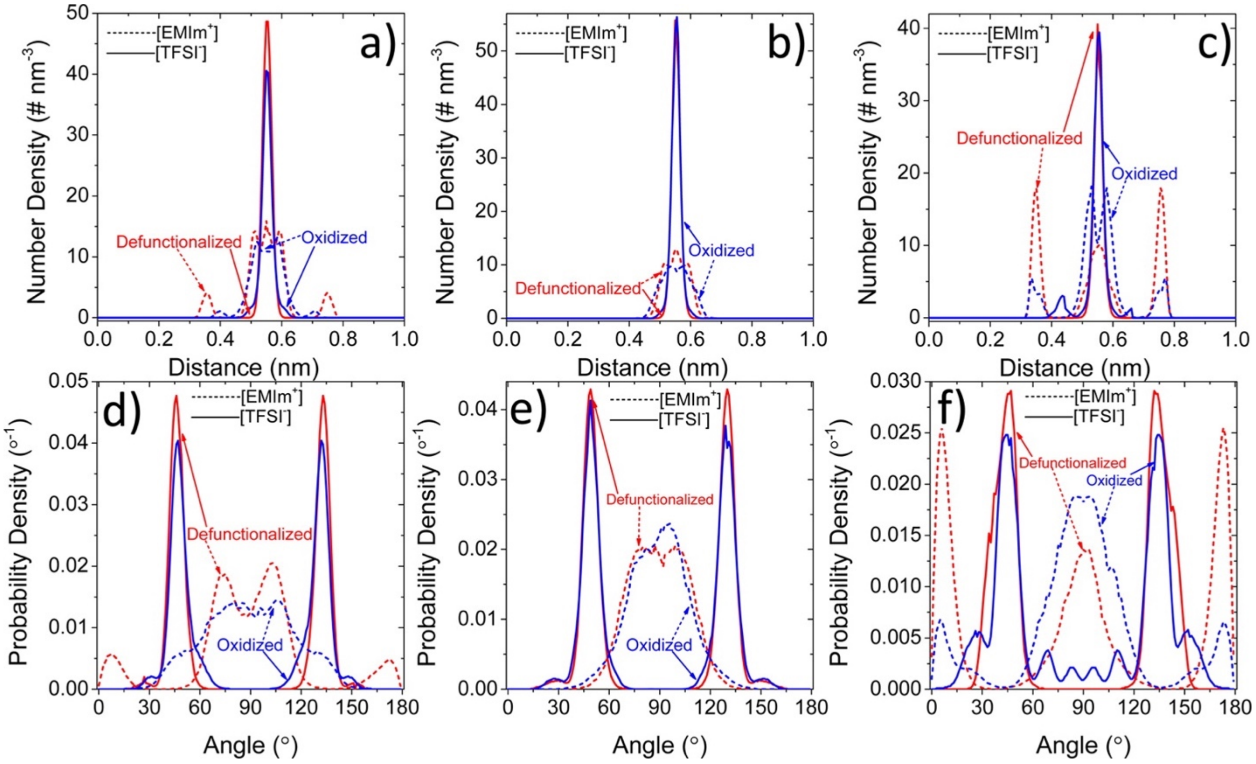

Figure 6.26 Ion accumulation densities inside of oxidized or defunctionalized pores under (a) no applied charge, (b) +5.0 μC cm$^{−2}$, and (c) −5.0 μC cm$^{−2}$. Corresponding ion orientations in the pores are given in (d), (e), and (f).

Under an applied positive voltage (+5.0 μC cm$^{-2}$ surface charge), the ion number densities and orientation distributions are similar inside defunctionalized and oxidized slit-pores (Figure 6.26(b)). The net result yields slightly lower ion accumulation in the oxidized lit pores than in defect-free ones. This finding agrees with experimental square-wave measurements. However, an applied negative potential (−5.0 μC cm$^{-2}$ surface charge) yields some distinct differences (Figure

6.26(c)). [$EMIm^+$] was more likely to accumulate near the center of the slit pores (Figure 6.26(d)), which gave rise to the appearance of a high double-peak near the center in the number density distribution and decreased peak heights at 0.35 nm and 0.75 nm. As the [$EMIm^+$] ions move to the pore center (Figure 6.26(e)), they adjust their orientations form parallel (0°) to the surface to vertical to the surface (90°) (Figure 6.26(f)). Although the change for [$TFSI^-$] is less prominent, small peaks appears in the density profile at 0.43 nm and 0.75 nm in the oxidized slit-pores.

The overall result for [$EMIm^+$][$TFSI^-$] confined in 0.8-nm slit-pore (summarized in Table 6.1) shows that the oxidized slits pore accommodates more ions. However, since oxidized slit pores favors the adsorption of [$TFSI^-$], the ion accumulation does not increase. Subsequently, oxygen groups increase the ionophilicity of charged slit pores, Simulations also shows decreased ion densities in uncharged oxidized pores, in agreement with the neutron scattering results. Under positive applied potentials, the hydroxyl groups attract more counterion into pores. Under negative applied potentials, the presence of oxidized carbon atoms let go relocation and reorientation of the ions and maximizes the IL density in the confined state. The MD simulation results agree well with electrochemical measurements, which show high $C_{sp}$ values for oxidized, ionophilic pores.

### 6.3.6 Neat ionic liquid confined in bimodal (0.8 nm and 2.6 nm) slit-pores

In this section, we investigate the electrochemical behavior and ion dynamics of [$OMIm^+$][$TFSI^-$] confined in bimodal CDCs. The electrochemical impedance measurements are shown in Figure 6.27. The Nyquist plot comparison (Figure 6.27(a)) shows higher [$OMIm^+$][$TFSI^-$] mobilities under a dynamic potential field in the presence of surface oxygen groups. Despite exhibiting near-identical equivalent series resistance ($R_s$) parameters, the mid-range ionic impedance is 8.1 Ω higher for defunctionalized CDCs than for oxidized CDCs. Although impedance is almost identically capacitive-dominated at 10 mHz (-81.9° for oxidized CDCs and -80.9° for defunctionalized CDCs), oxidized CDCs are more predominantly capacitive at mid-to-high frequencies (Figure 6.27(b)). The equilibrium time constant (Figure 6.27(c)) is 27% lower for the electrolyte in oxidized CDC pores, which suggests more rapid electrosorption processes for electrodes with oxygen-rich surfaces.

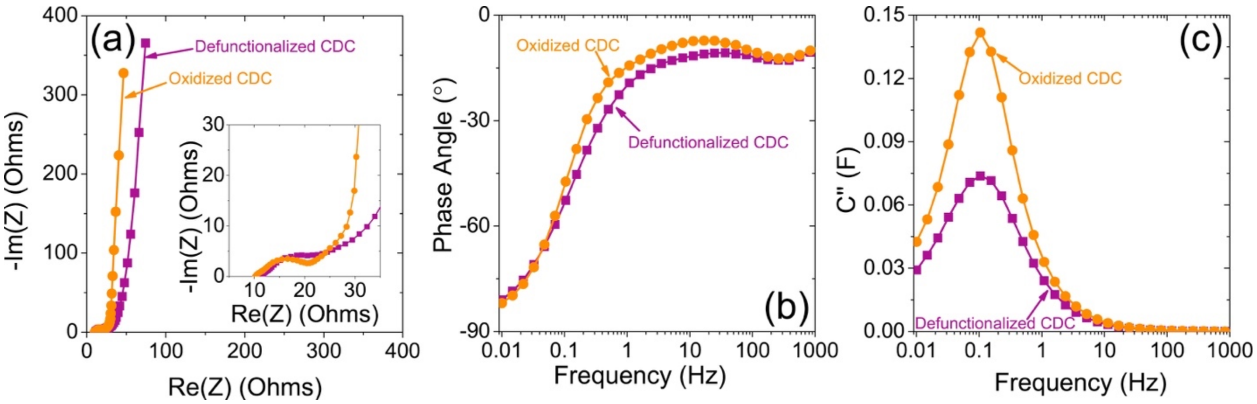

Figure 6.27 (a) Nyquist plot comparison. (b) Phase angle vs. frequency relationship for electrochemical impedance. (c) Bode impedance plot.

Figure 6.28 shows that the SSA-normalized capacitance is greater for the oxidized CDCs than for the defunctionalized CDCs. Cyclic voltammograms at low sweep rates (Fig. 6.28(b-c)) show inflection points during charge/discharge processes around +0.25 V. Figure inserts highlight this effect. Greater capacitance at lower potentials, followed by a dip at that voltage, and, subsequently, by an increase in capacitance at greater potentials signifies possible charge saturation and surface chemistry-dependent partial ion de-filling.[186] Furthermore, a drop in capacitance at low potentials is more pronounced for the defunctionalized CDC and underscores its ionophobic pore-electrolyte interface. The effect becomes more "smeared" at higher charge/discharge rates (Figure 6.28d). Previous experiments have confirmed codependent, unidirectional mobilities of both cations and anions during electrosorption.[187] Therefore, any pore de-filling process involves both co-ions and counterions.

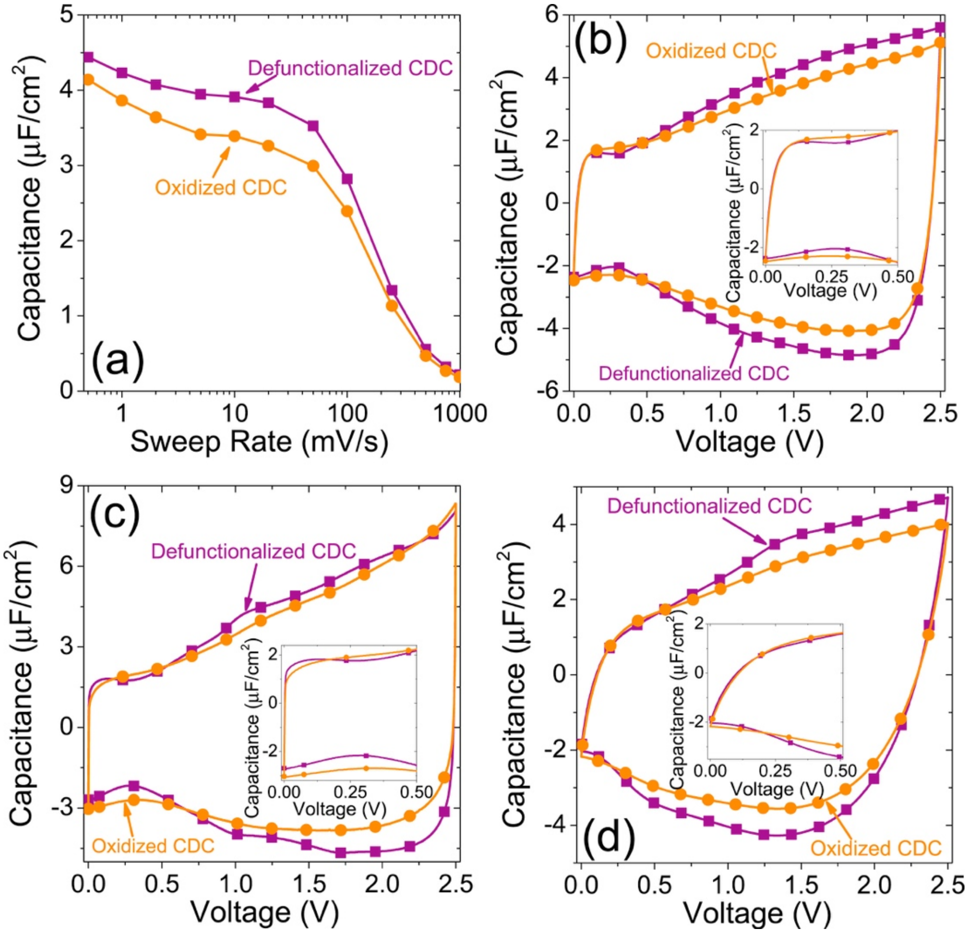

Figure 6.28 (a) Rate handling comparison of capacitance of [OMIm$^+$][TFSI$^-$]. Specific cyclic voltammograms are shown for (b) 0.5 mV s$^{-1}$, (c) 10 mV s$^{-1}$, and (d) 50 mV s$^{-1}$ sweep rates.

QENS results were obtained from porous CDCs filled with [OMIm$^+$][TFSI$^-$] using the vacuum infiltration approach. The procedure yielded near-complete pore filling of both micropores and mesopores, with only 0.002 cm$^3$ g$^{-1}$ void volume left in both defunctionalized and oxidized

CDCs. Note that QENS results reflect the dynamics of hydrogen-containing species of [OMIm$^+$] cations. The QENS spectra and Q-resolved width parameters for both defunctionalized and oxidized CDCs are shown in Figure 6.29. The diffusion coefficients, obtained from the low-Q slopes of the plots in Figure 6.29(b), is higher for the IL confined in oxidized CDCs than for IL confined in defunctionalized CDCs. More precisely, self-diffusive mobility of [OMIm$^+$] [TFSI$^-$] in oxidized pores is 2.6 times larger compared to defunctionalized pores. This finding agrees with our previous results in section 6.3.3. Since the bimodal CDCs possess sufficiently large pores that exceed the dimensions of the both cations and anions, they allow translational and rotational, as well as longer-range random walk motions. Although ions are expected to move in pairs, it is unclear whether the large cations (with a long hydrophobic tail) or the smaller anions are the main drivers of mobility.

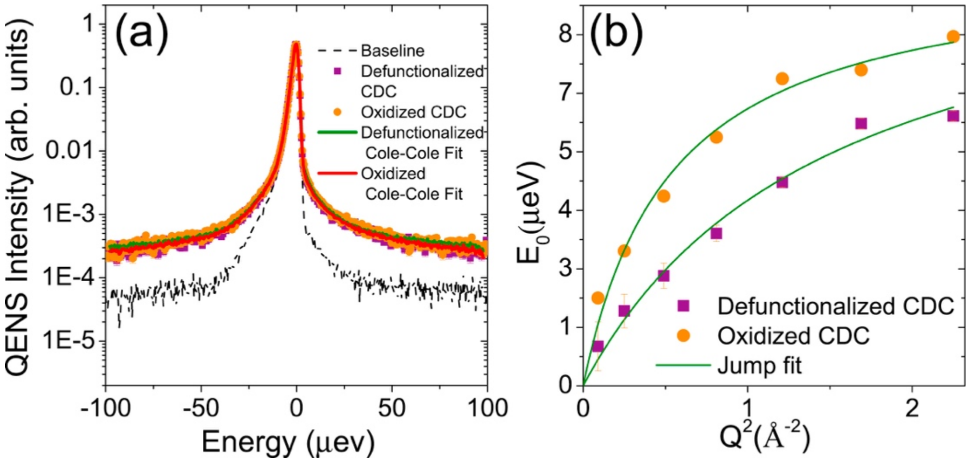

Figure 6.29 (a) QENS spectra for [OMIm$^+$][TFSI$^-$] confined in CDCs (b) Dependence of the width parameter of QENS spectra extracted from the Cole-Cole model function.

The increased mobility of ions in oxidized surfaces, which contains more hydrophilic −O−C=O− and C=O groups, may be attributed to more complete "wetting" of the pore surfaces by the ionic liquid molecules. Oxidized surfaces exhibit attractive intermolecular interactions with the polar groups of the [TFSI⁻] anion and draw more ions closer to the pore surfaces. Consequently, oxidized pores contain fewer ions in centers of pores (i.e. not directly bound to pore surfaces) than defunctionalized pores. This arrangement leaves more room for ions to move around each other and makes them more mobile. A similar concept had described the fast diffusion of ionic liquids confined in mesoporous carbon.[188]

In addition, we rely on X-ray pair distribution function (PDF) data to contrast changes in ion-ion correlations between bulk and confined states of ionic liquids in CDCs. The most informative approach is done through the examination of the net difference PDFs ΔG(r), which subtracts empty CDC scattering from each IL-filled CDC configurations:

$$\Delta G(r) = G(r)_{IL-filled-CDC} - G(r)_{empty-CDC} \tag{6.9}$$

Direct X-ray PDF analysis (plotted as r·G(r) vs. r) shows nearly identical structures for both empty CDCs and no influence of surface chemistry on the degree of graphitization (Figure 6.30(a-b)). The total PDF is dominated by the structural correlations of nanoporous carbon, which matches previously described diverse local C−C ordering.[189–191] Since surface functional groups constitute a relatively low fraction of total materials, low elemental sensitivities of X-ray scattering technique does not allow any discernible signals from these moieties. In comparison, the total PDFs of each IL-filled CDC exhibits extra intensities that augment signals from their corresponding empty carbon counterparts (Figure 6.30(c-d)). The first peak at ~1.4 Å in IL-filled CDC data becomes much more intense due the presence of C−C and C−N bonds (in [OMIm⁺]), and C−F, C−S and S−N, and S=O bonds (in [TFSI⁻]) from IL molecules (all have similar bonding distances).

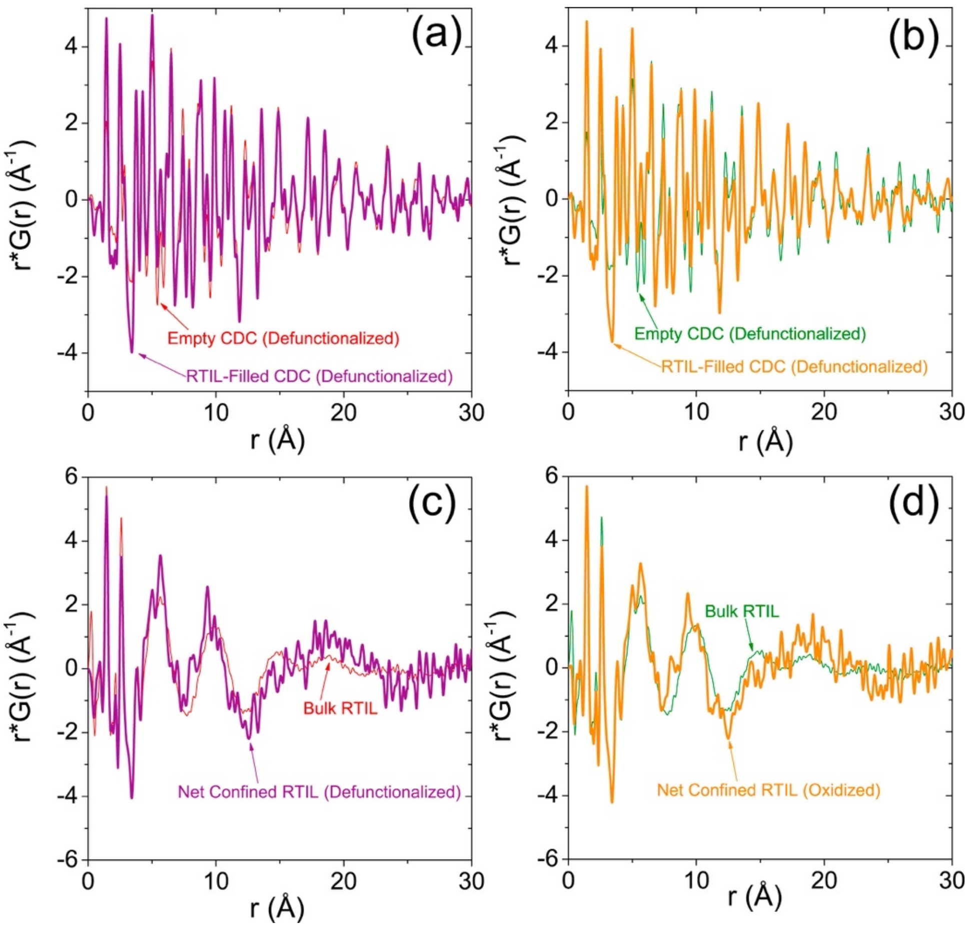

Figure 6.30 (a) Experimental X-ray PDFs of empty CDCs and (b) IL-filled CDC. Normalized difference PDFs of confined ILs in comparison with bulk IL data is shown for (c) defunctionalized CDC and (d) oxidized CDC. In all plots, the y-axis is presented as r*G(r) to emphasize signals in the high-r region.

The ΔG(r) analyses highlight ion-ion correlation differences between states of bulk (unconfined liquid) and confined (pore-filled) [OMIm$^+$][TFSI$^-$]. While pore surface chemistry does not alter the structure of the confined RTIL (within analysis errors), the confinement process significantly alters the properties of the ionic liquid. The broad and intense ‘bump’, which is featured at ~15−24 Å in all confined RTIL PDF samples, is absent in bulk RTIL PDF.

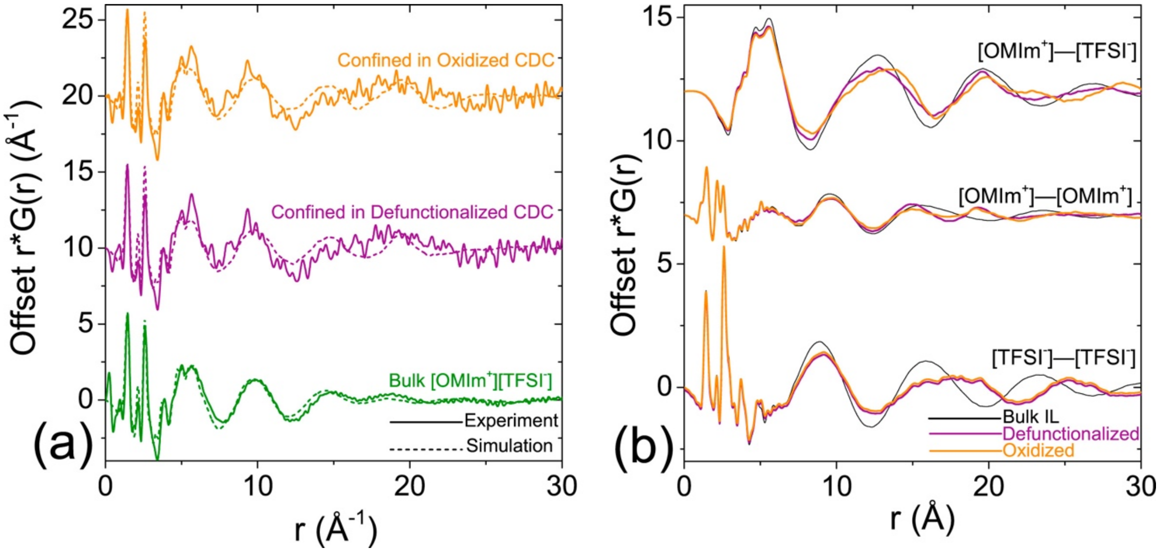

Figure 6.31 (a) MD-generated PDFs of bulk and confined ILs compared against to experimental observations. (b) MD-generated partial PDFs of bulk and confined ILs, showing changes in ion-ion correlations upon the confinement.

In order to further identify the origin of the variations seen in the different PDFs, MD models are developed using a simplified 2.6-nm slit-pore morphology. We benchmark bulk IL experimental PDF with simulated PDF from MD model (Figure 6.31(a)) to compare experimental and simulated PDFs of ions confined in pores with defunctionalized and oxidized surfaces. Structural properties of force-field generated bulk IL demonstrate good qualitative agreement with the experimental observations and correctly describe the shape/oscillations of the long-r range features (Figure 6.31(a) bulk RIL curve). For confined ions, the simulated PDFs also accurately exhibit the ‘bump’ features at ~15−24 Å (Figure 6.31(a)), albeit narrower in width than their experimental counterparts. This is likely due to the simpler single-size slit geometry used in the

MD calculation. Further investigations of surface chemistry effects are made possible via partial PDF analysis (Figure 6.31(b)). This approach splits the total PDF into a sum of three partials: [$TFSI^-$]-[$TFSI^-$], [$OMIm^+$]-[$OMIm^+$], and [$OMIm^+$]-[$TFSI^-$] correlations. The [$OMIm^+$]-[$TFSI^-$] correlation clearly oscillates in an opposite phase in contrast to the other two correlations. Comparisons between each set of partial PDFs reveal distinguishable, surface chemistry-specific interactions between ions and surfaces. For instance, oxidized surfaces shift [$OMIm^+$]-[$TFSI^-$] correlations toward the high-r region.

An interesting takeaway from the MD-generated PDFs is the fact that, in agreement with experimental results, surface chemistries do not alter cumulative ion behaviors. However, this description of ion-ion correlations is independent from their spatial orientations inside pores. Since PDF's diffraction method measures ensemble average of all intermolecular ion-ion correlations, it can neither separate partial correlations from the experimental data nor distinguish between ion-ion and ion-surface interactions. Given the complexity of this system, PDF helped us benchmark against molecular dynamics simulations. This is vital for our efforts to extract predictive information about the ion orientations, ion-surface interactions, and dynamics of ions in confinements.

Figure 6.32(a) shows the number density distribution inside of 2.6-nm slit-pores at the point of zero charge (PZC). Base on peak locations, we divided the plots into 2 regions. Region 1 accounts for the condition of strong ion adsorption, which significantly increases the number density over the bulk density. In this region, as compared to defunctionalized pores, oxidized pores show more affinity to [$TFSI^-$] ions than to [$OMIm^+$] ions ([$TFSI^-$] peaks are higher and closer to the surface, while the [$OMIm^+$] peaks are lower and more dispersed). While ions exhibit similar layered structures in region 2, the number density is only slightly higher than the bulk density.

Subsequently, oxidized pores demonstrate less prominent ion peaks than defunctionalized pores in this region. The MD results closely correspond with the SANS results described above: even though the oxidized pores attract more ions, especially the [TFSI⁻] ions to the surface, they contain fewer ions in the middle of the pore, and the overall number of ions inside is lower than that in the defunctionalized pore.

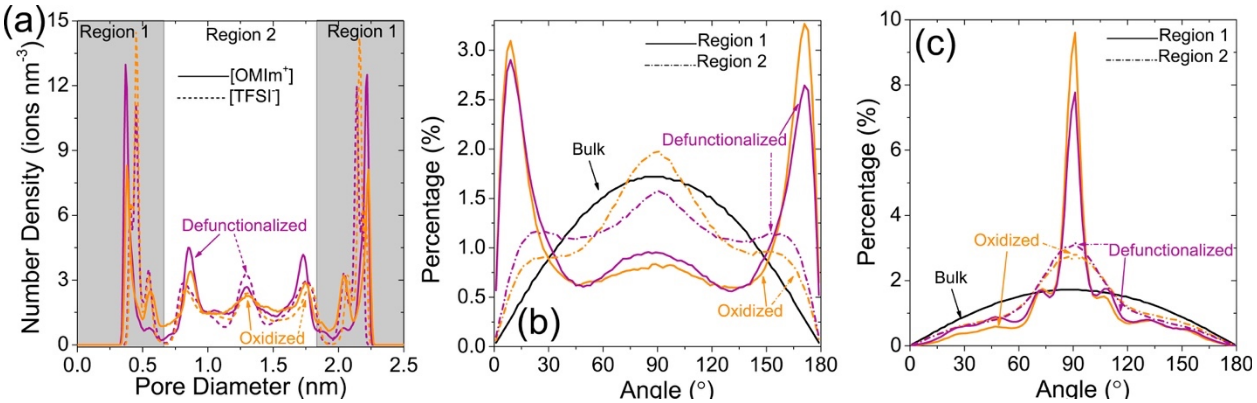

Figure 6.32 (a) Ion number density distribution in the direction perpendicular to the surface inside 2.6nm slit-pores with neutral surface charge. Angle distribution of (b) [OMIm⁺] and (c) [TFSI⁻].

As shown in Figure 6.32(b-c), these regions influence ion orientations (angles formed by the vector connection 2 C atoms and the normal vector of the slit surface). In region 1, due to π−π interactions, the imidazolium ring in cations more favorably arrange parallel to the electrode surfaces, which accounts for the location of first [OMIm⁺] peak near the electrode surface (Figure 6.32(b)). The significant angle distribution of [TFSI⁻] around 90° also suggests anions orient themselves along electrode surfaces in region 1 (Figure 6.32(c)). Oxidized surfaces intensify both effects. While region 2 features more random ion configurations, oxidized surfaces induce more perpendicular [OMIm⁺] orientations in pore centers.

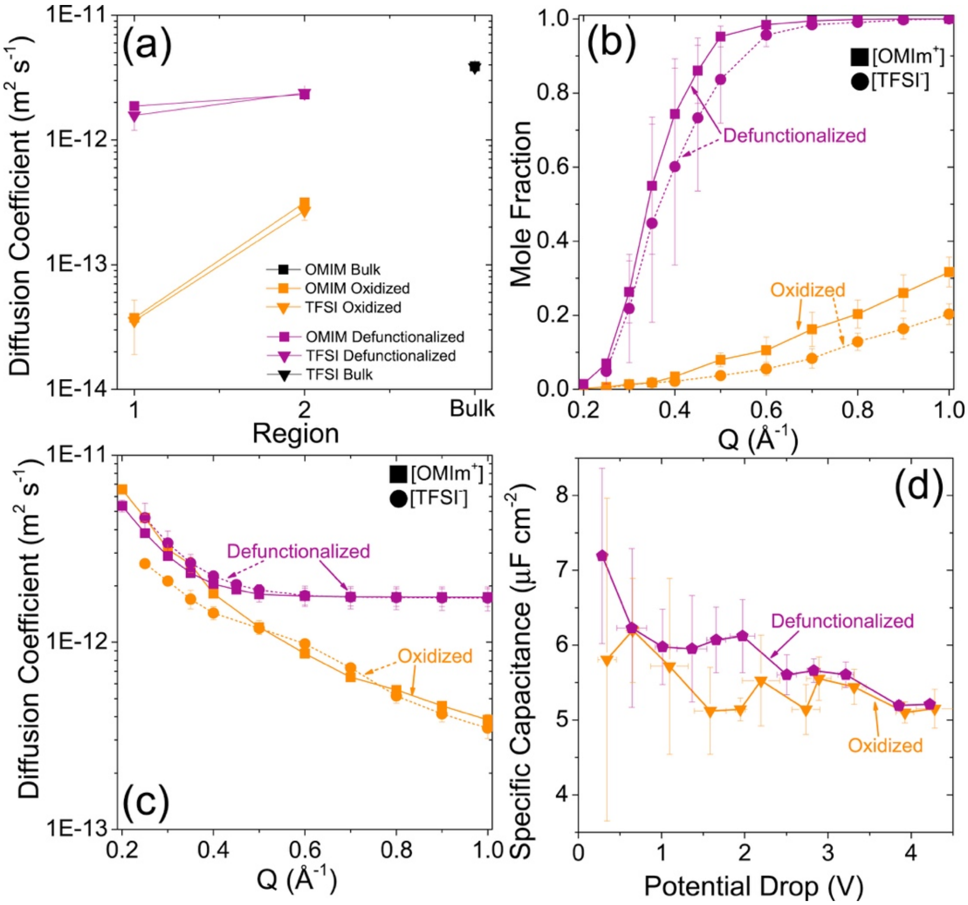

Figure 6.33 (a) Ion diffusion coefficients in different regions and bulk. (b) Mole fraction of selected ions as a function of Q. (c) Diffusion coefficient of selected ions as a function of Q. (d) Specific capacitance as a function of potential.

The diffusion coefficients of ions in different regions are shown in Figure 6.33(a). Confinement of ions in slit-pores noticeably decreases the overall diffusion coefficients, and smaller distances between ions and surfaces further expand that trend. Electrode-ion interactions strongly drive surface ions to pore interfaces and prevent facile diffusions. Furthermore, high ion densities near the wall imped ion mobility out of their respective shells. Oxidized surfaces make this effect more significant: diffusion coefficients in oxidized pores are nearly two orders of magnitude lower than in defunctionalized pores in region 1 and one order of magnitude lower in region 2. These results correlate with the QENS-derived observations that ions are more strongly attached to the oxidized surface, which yields more elastic scattering.

In an effort to thoroughly explain the QENS results, we adopt a similar strategy to define the observable mobility of ions in slit pore models. First, this approach calculates the MSD of each ion. For a given Q, an ion is considered to be mobile if its MSD, within a certain time period, exceeds $(\pi/Q)^2$. Second, an average MSD of all mobile ions yields the diffusion coefficients via a linear regression fit within the range of Q-values that are accessible to QENS. Shown in Figure 6.33(b), higher Q values captured more ion species. Moreover, as illustrated in Figure 6.33(c), at lower Q, oxidized pores yield lower diffusion coefficients than in defunctionalized pores. This trend is reversed at high Q, where the ion diffusion coefficients in oxidized pores are higher. This result further confirms our previous explanation that, while oxidized surfaces strongly attract ions, ionophilicity creates space for fast diffusion of ions in pore centers.

We calculate specific capacitance (Figure 6.33(d)) using the following equation:

$$C_{sp} = \frac{\sigma_{anode} - \sigma_{cathode}}{\phi_{anode} - \phi_{cathode}} = \frac{2\sigma}{\Delta\phi} \tag{6.10}$$

where $\sigma$ stands for the surface charge density, and $\Delta\phi$ stands for the potential differene between anode and cathode. The simulation predicts lower capacitance in the oxidized 2.6-nm pores, which may be related to reduced ability of functionalized pores to both accommodate ions and efficiently reorganize them into dense configurations.[151] To contrast the behavior of ions in mesopores with that in micropores, we also attempted to simulate [OMIm$^+$][TFSI$^-$] in 0.8-nm slit-pores. However, the resulting diffusion coefficients were found to be negligible (Figure 6.34(c)). Computational studies often report diffusion coefficients that are one order of magnitude slower in nanoconfined environments than those in the bulk.[17] These results agree with prior studies that show similar poor diffusion of confined ions in electrodes with neutral or slight surface charge. Furthermore, during the charging/discharging process, ions in nanoporous electrodes exhibited sloshing dynamics in slit channels[192] and an uneven distribution during rapid charging dynamics.[193] Therefore, the slow mobilities of ions in 0.8 nm slit pores preclude significant all-atom MD simulation analyses.

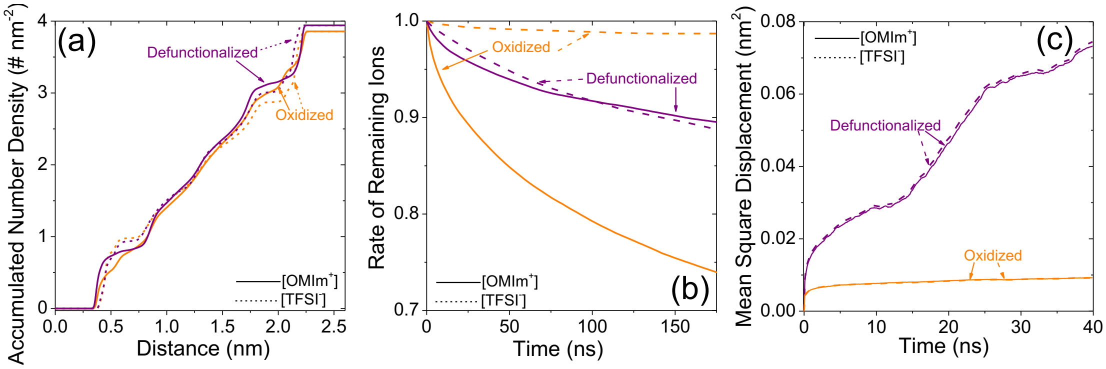

Figure 6.34 (a) The accumulated number density in the direction perpendicular to slit surface. (b) The remaining rate of ions inside region 1. (c) Mean-square displacement (MSD) as a function of time for 0.8 nm pristine/oxidized slit pore.

Our combined results underscore the intricate effects of pore size and surface chemistry on capacitance and ion dynamics. On the one hand, in agreement with QENS-derived ion diffusion measurements, surface oxidation improved the mobilities of the IL. This finding agrees with previous results, which had shown higher ionic mobilities in functionalized CDC pores.[194] On the other hand, this advantage does not translate into greater overall $C_{sp}$ of oxidized pores. This takeaway, in turn, agrees with previous results that demonstrated higher capacitance on defunctionalized surfaces in nonporous electrodes (with no ion confinement).[195] While oxygen groups improve the [TFSI$^-$]'s interface with pore surfaces, they repel the alkyl chain on the [OMIm$^+$] cations. In all likelihood, the net effect of this process reduces the number density of electrosorbed ions on accessible surfaces. Since the narrow pores don't provide sufficient degree of freedom for both translational and rotational diffusion of cations, ions inside the mesopores contribute most to the QENS signal.[188,196] Subsequently, even in larger pores with more bulk-like ion dynamic behaviors, oxidized pore surfaces improve pore ionophilicities and influenced electrolyte dynamics. Since the mesopores account for 78−79% of the total porosity of each sample, they constitute a larger fraction of the total capacitance.

## 6.4 Conclusions

In this chapter, we have used a combination of electrochemical testing, neutron scattering, X-ray scattering, and MD simulations to determine the influence of surface chemistry on electrosorption and capacitance of supercapacitors with nonporous and porous carbon electrodes. On nonporous graphene electrodes, the neat ionic liquid and solvated ionic liquids all show decreased capacitance when the surfaces were hydroxylated. In the neat ionic liquid case, the hydroxyl groups either diluted the counter-ion accumulation or attract co-ions into the EDL, which all decreases the capacitance. In the case of solvated ionic liquids, the distribution and orientation of acetonitrile across the system exerted vital influence on the capacitance, especially on the positive hydroxyl-free electrode. Furthermore, MD simulations of ion mobility with respect to electrode surface in the lateral and perpendicular directions revealed significantly slower diffusion performance on oxidized surfaces.

In the case of ion confinement in CDCs with small (0.8 nm) pores, oxygen-rich CDC pore surfaces allowed [$\text{TFSI}^-$] anions to align parallel to pore surfaces and decreased electrolyte density in uncharged pores. Subsequently, charges obtained greater room and mobility during electrosorption, and oxidized porous electrodes demonstrated higher capacitance, faster ion dynamics, and better rate handling ability. In the case of ion confinement in bimodal CDCs, the oxidized pore strongly attracted ions, which creates space for fast diffusion of ions in pore middles. But the oxidized pore failed to accommodate ions and reorganize ions into dense configurations inside the pore, and exhibited lower capacitance compared to defunctionalized pores. In all, our integrated approach provided a comprehensive picture of the effects of surface oxidization of carbon electrodes on the capacitance and ion dynamics.

# CHAPTER VII

# MODIFICATIONS ON ELECTROLYTES

In Chapter IV, V and VI, we discussed ways to modify electrodes and their influences on the performance of supercapacitors. In this chapter, we will consider ways to modify the electrolytes and evaluate how the change of electrolytes affects the performance of supercapacitors. First, we investigate the extent to which the alkyl chain on the cation of an imidazolium-based neat ionic liquid influences mobility and electrochemical behavior in nanoporous supercapacitors. Changing the cation chain length from an ethyl ($n = 2$) to a butyl ($n = 4$) to a hexyl ($n = 6$) group affects the electrolyte dynamics and their accumulation densities under dynamic charge-discharge processes. We contrast the different dynamics of ionic liquids in bulk and confined states and demonstrate the effect of the cation dimension on resulting arrangements of positive and negative ions in pores. Second, we investigate the effects of solvent concentration on the bulk properties of an ion liquid electrolyte and the electrochemical performance on carbon-based electrodes, including pristine graphene, oxidized graphene, graphene armchair edge, graphene zigzag edge, onion-like carbon, and slit-pore carbon. We find that diluting the electrolyte weakens ion correlations in the bulk, and improves ion dynamics. The capacitance of the two edge electrodes decreases monotonically as the solvent concentration increases, while the capacitance of other non-edge electrodes shows a non-monotonic behavior and a capacitance maximum is observed. Further analyses on the electric double layer reveals two competing factors: solvation reduces the charge overscreening effect, but it also causes the dilution of absorbed ion concentration. While the former increases the capacitance in the high ion concentration regime, the later decreases the capacitance in the low ion concentration regime. In addition, the dilution also significantly improves the ion dynamics at the interface. We correlate these results in an effort to design electrolytes that could potentially enhance the energy density and power density of ion-liquid-carbon supercapacitors.

Part of this work has been published in Ref. 199. In addition, a manuscript is in preparation for submission as a peer-reviewed publication.

## 7.1 Introduction

While an ever-growing number of viable room-temperature ionic liquids are available, supercapacitors typically rely on several select systems.[197] Cations are usually composed of aromatic heterocycles such as alkylimidazolium (alkyl chain attached to an imidazole, $C_3N_2H_4$)[198,199] or an alkylpyrrolidinium (two alkyl chains, typically a methyl and a propyl, attached to a pyrrole, $C_4H_4NH$), [200–202] a heterocyclic amine (such as N-methyl-N-propylpiperidinium),[203] a tetraalkylammonium (four alkyl chains attached to a quaternary nitrogen center),[94,98] or a simple lithium salt.[204] Anions of RTILs in energy storage devices are, typically, less diverse and feature either bis(fluorosulfonyl)imide (TFSI)[203] or tetra- fluoroborate (BF4).[205] Many additional ionic liquids in development will be implemented in supercapacitors in the future.[204] Intuitively, many anion/cation combinations are possible, and blends of two or more ionic liquids also endow electrolytes with enhanced temperature and operating potential ranges.[206,207] The alkyl chain lengths on the different cations are also customizable (from simple methyl groups to chains of over 12 carbon atoms long), and this option further expands the list of possible electrolyte systems.[208]Tunability of these RTILs is an essential property that allows optimal tailoring of electrolyte dimensions to porous electrodes in order to maximize capacitance,[209] improves ion dynamics in order to maximize power densities, and lowers the melting point of these liquids in order to expand the operating temperature range of resulting supercapacitors.[210]

Since the electrode and electrolyte parameter space is vast, and experimental study of every combination is inefficient, advanced research of IL-based supercapacitors requires a more in-depth approach that fully accounts for the physical properties of ionic liquids and electrosorption conditions.[211] As described above, ILs have highly complex structures with diverse functional groups and branched backbones and significantly diverge from simple, previously-used coarse-grained spherical models of ions.[17] Key properties of ionic liquids, such as viscosities and melting temperatures, depend on the molecular dimensions and ion-ion coordination and intermolecular forces (as determined by stereochemistry of cations and anions).[212–214] Even neat, solvent-free ionic liquids develop complex solvation shells that affect their arrangement inside and outside of porous electrodes.[166] While basic characterization tools can assess the bulk liquid behavior of these ions, geometrical confinement and dynamic applied potentials significantly influence the electrochemical behavior and stability.[215] Furthermore, electrodes exhibit hierarchical pore structures with varying degrees of ion confinement,[216] imperfect interfaces with surface defects,[34,180] moieties,[195,217] and quantum capacitance contributions.[49,109,156] Physical electrode materials contain defined internal and external surfaces and,[218] under dynamic potential conditions, involve both interactions between bulk and electrosorbed electrolytes as well as localized ion rearrangements.[187] This parameter space adds high complexity to experimental supercapacitor systems and requires advanced characterization techniques and computational methods that probe electrolyte dynamics and arrangements in light of all of these conditions and properly assess the significance of system variables.[219]

There are, however, limitations of using ionic liquids as electrolytes. Their slow transport properties and low electrical conductivities in their neat states may reduce power densities, especially when neat ILs are confined in nanoporous electrodes.[10,11] In practice, ILs are often mixed with organic solvents to enhance their rate handling capabilities.[58–61] While most researchers found that solvation of ionic liquids greatly increases conductivities and the power densities of EDLCs,[6,21,62–64] the effects of solvation on the energy density are less clear. On one hand, slightly narrower voltage windows are expected when organic solvent is introduced into the electrolyte, which might compromise the energy density.[62,65] On the other hand, it has been shown by both experimental and computational studies that the addition of solvent improves capacitance of graphene-based EDLCs.[66–69] Particularly, Bozym et al. found that by diluting 1-ethyl-3-methylimidazolium bis(trifluoromethyl- sulfonyl)imide (EMImTFSI) with a miscible organic solvent, the differential capacitance on glassy carbon increases and reaches a maximum when the ion concentration is 5-10 mol%.[68] Similarly, Uralcan et al. observed nonmonotonic behavior of the capacitance as a function of ion concentration using molecular dynamics simulations, where the capacitance on graphene exhibited a maximum at intermediate concentrations.[69] Nevertheless, the effects of solvent concentrations on the performance of other carbon electrodes, such as OLCs and CDCs, are less studied.

In this chapter, we first examine electrosorption of three ionic liquids in a single carbon electrode system. Specifically, we use an electrolyte system with a varying alkyl chain length (from a 2-carbon-atom (ethyl) to a 6-carbon-atom (hexyl)) on the cation of an imidazolium-based ionic liquid with a [TFSI$^-$] anion. We rely on a nanoporous CDC electrode material with a narrow pore size distribution (0.8 nm). We decouple the effects of ion dynamics from ion arrangements in confined environments to assess how specific chemical changes of ion structure and resulting dimensional constraints influence capacitance, ionic impedance, and rate handling abilities of electrochemical capacitors under high charge/discharge loads. In addition, we use MD simulations to explore the effects of solvent concentration on the performance of IL-carbon supercapacitors. We look into the bulk solutions of [EMIm$^+$][TFSI$^-$] in acetonitrile, and investigate their bulk structures and ion dynamics. Then we explore their performances on various carbon surfaces, including pristine graphene, oxidized graphene, graphene edges, OLC, and CDC. By examining the electric double layer structure and ion dynamics in the confined systems, we provide comprehensive analyses of the effects of solvent concentration on the energy density and power density of IL-carbon based supercapacitors.

## 7.2 Computational Methods

### 7.2.1 MD simulation of ILs with different cation lengths

Classical molecular dynamics simulations were carried out to investigate the IL dynamics in bulk and confined states. A slit pore model represented CDC confinement and the gap between 2 slit surfaces was set at 0.8 nm. The slit was 12 nm long and connected to a bulk reservoir at both ends, and periodic boundary conditions were applied to all three directions. To avoid complications due to entrance effects, only the central 8 nm was selected for analysis of structure and dynamics in the pore. All MD simulations were conducted in the canonical NVT ensemble (constant number, constant volume and constant temperature) using GROMACS.[140] During the simulation, temperature was maintained via the Nosé-Hoover thermostat.[220] We relied on a previously derived force field for ionic liquids,[221] and the electrode carbon atoms were defined by the AMBER force field.[175] Van der Waals interactions and electrostatic interactions in real space were cut off at 1.1

nm, and long-range electrostatic interactions were computed using the PME method with a grid space of 0.1 nm and a fourth-order interpolation.[222] Production runs lasted 50 ns for each bulk simulation. For ions in slit pores, each simulation was initialized at 800 K for 2 ns, followed by 8 ns of annealing to 300 K. After another 10 ns of equilibration at 300 K, a final 40 ns production run was conducted. Each simulation was repeated 3 times with different initial configurations, over which results were averaged to reduce statistical uncertainties. All simulations adopted a uniform time step of 2 fs, and the trajectories were saved every 5000 steps. A snapshot of the simulation is shown as Figure 7.1.

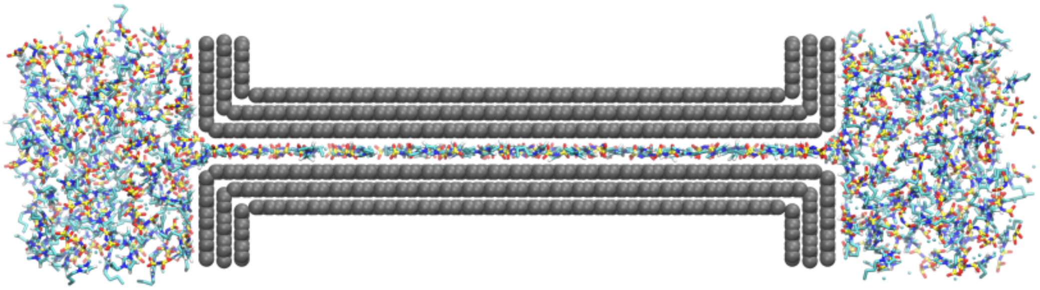

Figure 7.1 Snapshot of the MD simulation of ions confined in a 0.8 nm diameter slit pore.

### 7.2.2 Simulation of solvated ionic liquids on various carbon electrodes

Molecular dynamics simulations were conducted on EMImTFSI solvated in acetonitrile (ACN) with 9 different ACN weight percentages: 0% (neat IL), 2%, 5%, 10%, 25%, 50%, 75%, 90%, 100% (pure ACN), which corresponds to molar percentages of 0%, 16%, 33%, 51%, 76%, 91%, 99%, 100%, respectively. The force field for EMImTFSI were adopted from Lopes's work[172,173], and the force field for ACN were from Wu's work.[223] Figure 7.2 shows the electrode models used in this work. More specifically, three layers of graphene sheets were used to represent the pristine graphene electrode. The oxidized graphene model differed from the pristine model by adding hydroxyl groups on graphene surface. The hydroxyls cover 2.8% of surface carbon atoms, with configurations from Yan's work.[224] We adopted same graphene edge models from our previous computational work: both zigzag edge and armchair edge were capped with hydrogen atoms.[180] The onion-like carbon was modeled as three concentric fullerenes, with radius of 0.356 nm ($C_{60}$), 0.705 nm ($C_{240}$), and 1.018 nm ($C_{500}$). Slit-pore model was used to represent the CDC electrode, where the distance between inner slit surfaces was 0.8 nm. The non-bonded parameters for all electrode models except for the graphene edges were from OPLS-AA force fields,[225] and the graphene edge sites were described by the polymer consistent force field (PCFF).[113,226] We relied on Lorentz-Berthelot combination rule to calculate the Lennard-Jones parameters between different kinds of atoms.

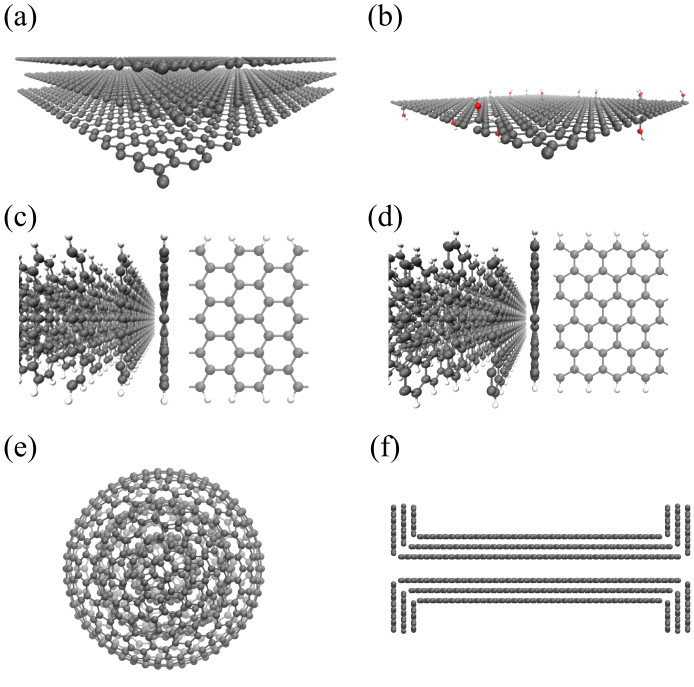

Figure 7.2. Electrode models used in this work: (a) three-layer pristine graphene; (b) oxidized graphene; (c) armchair graphene edge; (d) zigzag graphene edge.

The simulations of bulk electrolytes were conducted in isothermal-isobaric (NPT) ensemble using MD package GROMACS.[140] All bonds were constrained using the LINCS algorithm.[227] For each run, the system was initiated and maintain at 800 K for 5 ns, followed by an annealing process to cool the temperature to 300 K in 5ns. The system was further equilibrated at 300 K for 10 ns, and a final 20 ns production run was carried out, from which we collected data for analyses. The temperature of the simulation system was controlled by the Nose-Hoover thermostat with relaxation time of 0.4 ps, and the pressure was maintained at 1 bar by Rahman-Parrinello barostat with time constant of 1.0 ps. Simulations of electrolyte-electrode interfaces were conducted in canonical (NVT) ensemble. Figure 7.3 shows the simulation setup for each type of electrode. For graphene-based electrodes (pristine graphene, oxidized graphene, graphene edges), channel simulations were constructed. Each was composed of an electrolyte enclosed by two electrodes.

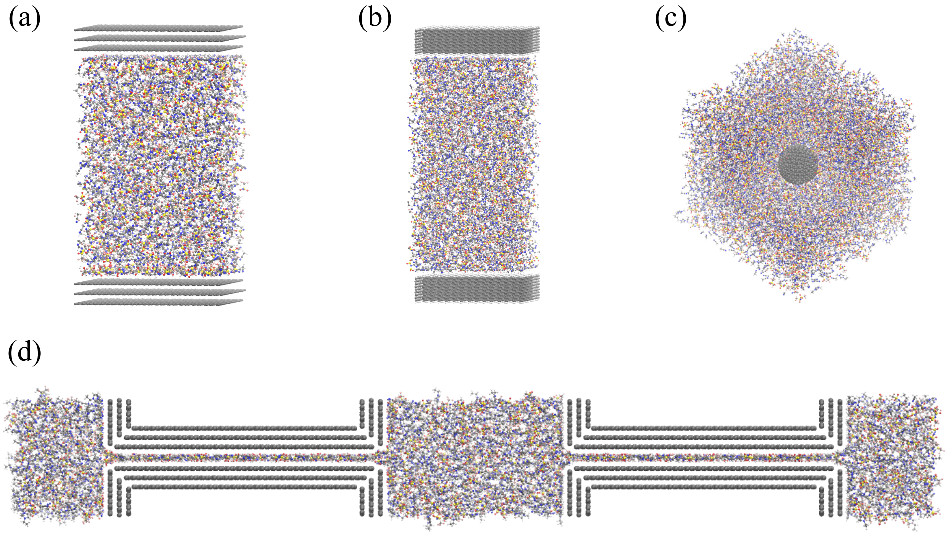

Figure 7.3 Screenshots from (a) channel simulation of graphene basal planes, (b) channel simulation of graphene edge planes, (c) simulation of an onion-like carbon in an electrolyte, (d) simulation of slit-pore carbon in an electrolyte.

For all channel simulations, the slab-PME method was used to compute the electrostatic interaction.[116] The distance between the two electrode surfaces was set to 8 nm, so that a bulk-like behavior of electrolyte was observed in the center. The box length in the direction perpendicular to the electrode surface was set to be 5 times of the electrode distance, so that the electrostatic calculation was accurate enough.[116] For the OLC, a single electrode was immersed in a cubic simulation box full of electrolyte. The box length was set as 4.5 times of the diameter of OLC, and this gave a bulk-like density near the box margin. For the slit-pore model, two slit-pore electrodes were immersed in a rectangular simulation box full of electrolyte. The distance between the two electrodes was set to 7 nm. All electrode atoms for these simulations were fixed in space, except for the hydroxyl groups on the oxidized graphene, which were set to rotate and bend. Net surface charges were uniformly distributed to the surface atoms on each electrode, and opposite surface charges on cathode and anode guaranteed charge neutrality when there are two electrodes in the system. For the OLC system, when the electrode was positively/negatively charged, corresponding number of anions/cations were removed. Same heating and annealing approaches were used as in the bulk simulations. All simulations used a time step of 2 fs, and were repeated 3 times with different initial configurations to ensure reproducibility of results.

## 7.3 Results and Discussion

### 7.3.1 Ion dynamics of ionic liquids with different cation sizes

The QENS spectra, depicted in Figure 7.4(a-b), show a decrease in quasi-elastic (QE) broadening that correspond with increased alkyl chain length of the cations, suggesting their reduced mobilities with increasing molecular size. Q-dependent QE broadening observed from the spectra further hints the presence of translational mobility of cations in confinement. Therefore, the measured dynamic structure factor was analyzed using a sum of two Lorentzians as a model function. Extracted values of HWHMs were plotted against $Q^2$, and are presented in Figure 2(c-d) for both fast and slow components.

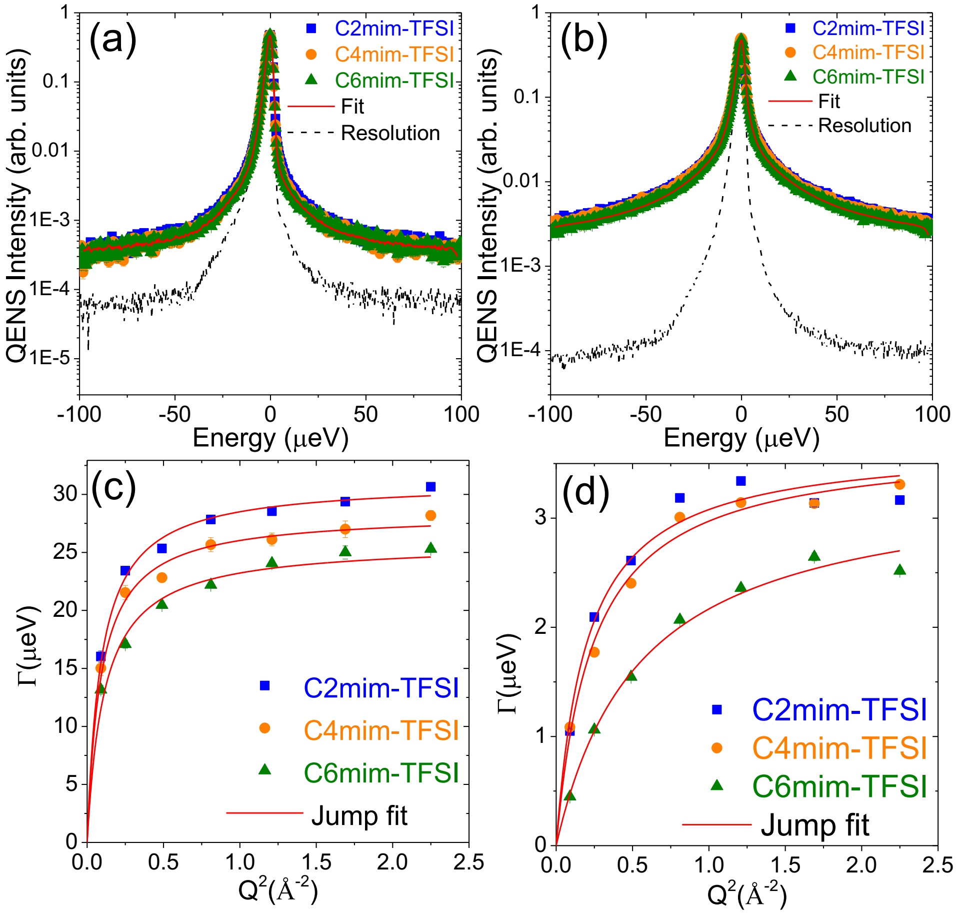

Figure 7.4 QENS spectra (a) Q = 0.3 $Å^{-1}$ and (b) Q = 1.1 $Å^{-1}$ at 300 K. The half width at half maxima (HWHM) extracted from the double Lorentzian fit of the data are shown for (c) fast diffusion and (d) slow diffusion.

MSD for each IL in its bulk state and its corresponding ion self-diffusion coefficients are shown in Figure 7.5. We find that diffusivities of cation and anion drop as the alkyl chain length increases, which matches with experimental neutron scattering results (Figure 7.4). Furthermore, the radial distribution functions (RDFs) between different ion pairs, shown in Figure 7.6, the intensity of the cation-anion correlation increases as the chain length grew, indicating more structure and less mobility for IL with larger alkyl chains. In addition, all the RDF peaks in Figure 7.6 shift slightly to larger distances at longer cation chain lengths. Larger cation sizes, which also increase cation-cation correlations and decreased anion-anion correlation, causes this effect.

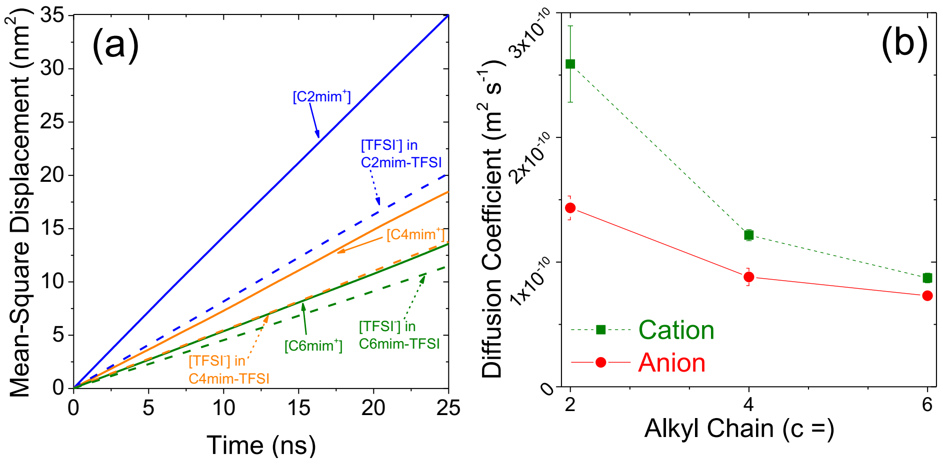

Figure 7.5 (a) MSD of [$C_2$MIm$^+$][TFSI$^-$], [$C_4$MIm$^+$][TFSI$^-$], and [$C_6$MIm$^+$][TFSI$^-$] in the bulk. (b) Ion self-diffusion coefficients.

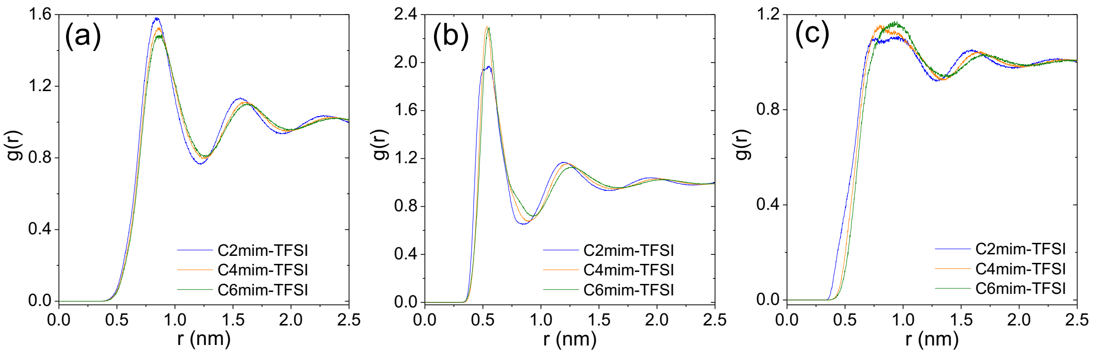

Figure 7.6 MD-derived RDF for (a) cation-anion, (b) cation-cation, and (c) anion-anion in bulk.

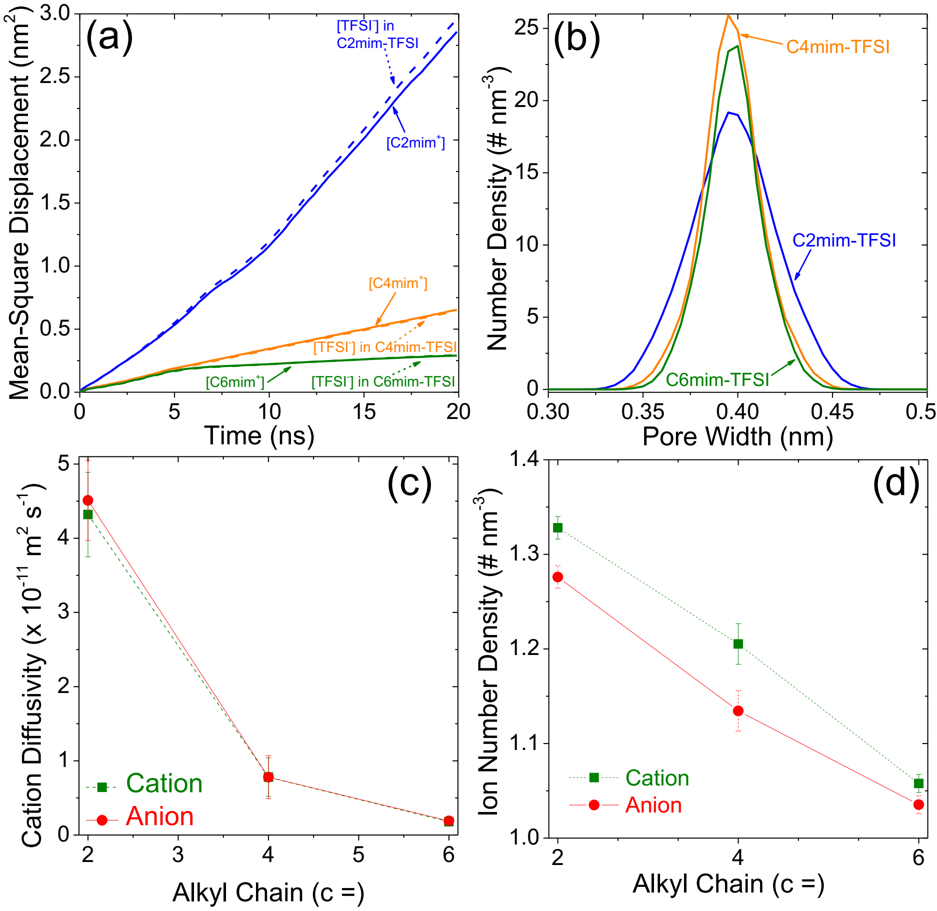

Figure 7.7 (a) MSD of ions in a 0.8-nm slit-pore. (b) Number density of cations across the pore surface. (c) Self-diffusion coefficients in slit pores. (d) Average number densities.

For ion confined in the slit-pores, Figure 7.7(a) shows decreased ion self-diffusion coefficients for both cation and anion associated with longer cation chain lengths. Moreover, as compared to the bulk diffusion coefficients, diffusivities of ions in confinement exhibit an order of magnitude decrease (Table 7.1). Of note, the diffusion coefficients for the cations and anions become very similar under confinement, although they exhibit considerable differences in the bulk. This phenomenon has been reported by previous simulation works, including for ionic liquids on flat and rough electrode surfaces[228] and confined in slit pores.[183,217,229] Our findings complement a previous investigation of effects of pore size on dynamics of ionic liquids confined in slit nanopores, which had reported on decreasing differences between dynamics of cations and anions associated with corresponding decreasing pore sizes.[161] In our case, since ions in the slit pore can only form a single layer (Figure 7.7(b)), cation displacement likely produces similar displacement of surrounding anions, which increases the similarities between the calculated cation and anion self-diffusion coefficients.

Table 7.1 Comparison of ion self-diffusion coefficients ($10^{-10}$ $m^2/s$) in bulk and in slit pores

| Electrolyte | Cation Diffusion ($10^{-10}$ $m^2$ $s^{-1}$) | | Anion Diffusion ($10^{-10}$ $m^2$ $s^{-1}$) | |
|---|---|---|---|---|
| | Bulk | Slit Pore | Bulk | Slit Pore |
| C2mim-TFSI | 2.589 | 0.432 | 1.435 | 0.451 |
| C4mim-TFSI | 1.216 | 0.078 | 0.881 | 0.078 |
| C6mim-TFSI | 0.872 | 0.018 | 0.73 | 0.019 |

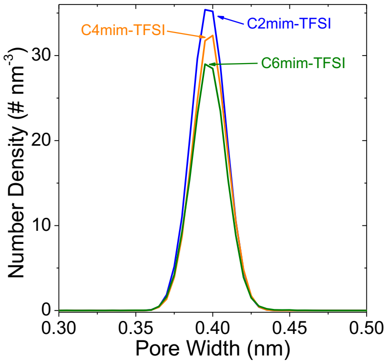

Figure 7.8 Number density for anions inside the slit pore.

In this nanoconfinement, ions could only form a single layer. Figure 7.7(b) and Figure 7.8 further confirm this with center-of-mass number density distributions across slit pore surfaces. As the cation chain length increases, the cation distribution becomes narrower, implying that the long alkyl tails hamper movement and self-rearrangement of cations. Since longer chain lengths also increase cation size, the average number density of cation inside the pore decreased from [$C_2MIm^+$] to [$C_6MIm^+$] (Figure 7.7(d)). Furthermore, as shown in Figure 7.7(c-d), larger cations have the capability to displace anions, reducing the anion peak height and the average number density of anions in the pore. Number densities for cations and anions for the three electrolytes are included in Table 7.1. In Figure 7.7(d), cation always shows slightly higher number densities than anion. While the charge neutrality is maintained for the whole system, this slight difference in cation and anion numbers inside slit pore may be attributed to their different affinity to the slit surface at PZC, through van der Waals interactions. MD simulations of planar electrode surfaces also reported different ratio of cation and anion presented in the EDL.[34,67]

### 7.3.2 Bulk properties of solvated ionic liquids

Figure 7.9 shows the center-of-mass (COM) radial distribution functions and the coordination numbers. The RDFs of anion around cation are shown in Figure 7.9(a). The first anion peak of each RDF appears at about 0.5 nm. This distance does not change much as more ACN presented in the solution, but the peak height increases. Note that the RDFs are normalized with respect to the number that would be observed if the molecules are uncorrelated. This indicates that the correlation between cation and anion is still strong even when the ion concentration is low. Figure 7.9(b) further shows the coordination number of anions around a cation, where the coordination number decreases as ACN weight percentage increases, dropping from 7.5 at neat state to 0.84 when the system has 90 wt% ACN.

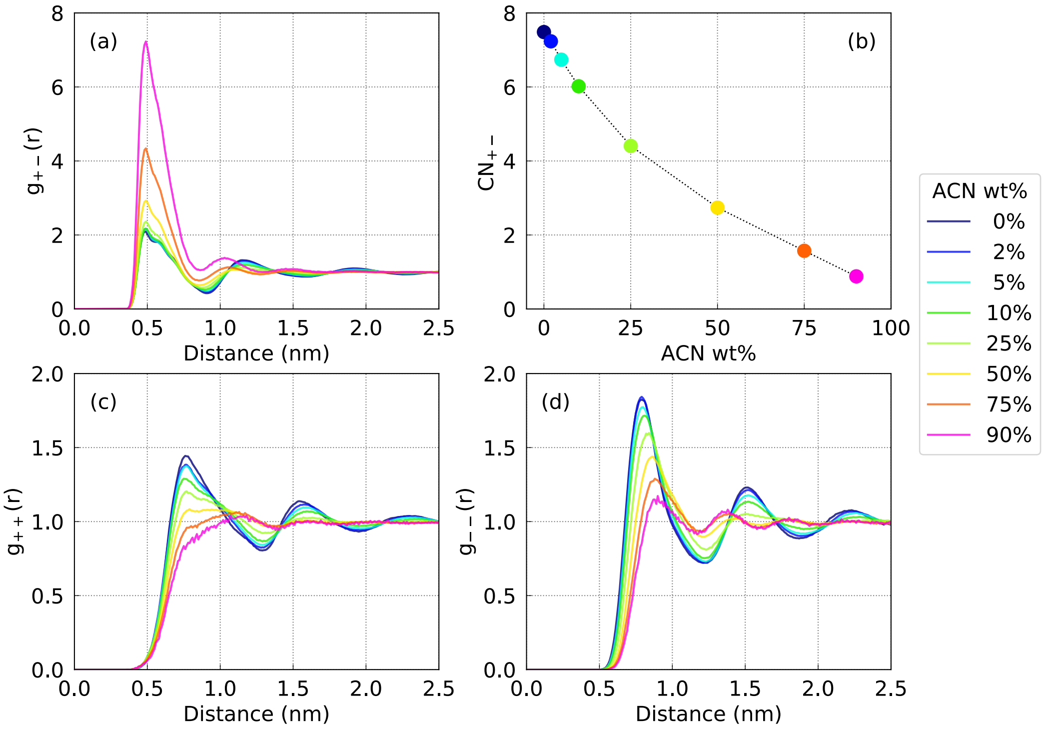

Figure 7.9 (a) RDF of cation and anion. (b) Coordination number (CN) of anions around cation. (c) RDF of cation and cation. (d) RDF of anion and anion.

Combining these two together, we infer that the dilution of the ionic liquid weakens ion correlations by reducing ion pairs, but still, the cation-anion correlation is strong. Figure 7.9(c-d) show the RDFs of cation-cation and anion-anion respectively. In both figures, we see drops of peak heights as the electrolyte becomes more dilute. Especially for the system with 90 wt% ACN, the curves only oscillate marginally around 1, indicating the same charge ions have very weak correlation. In addition, the location of the first peak also shifts to a larger distance as more ACN is added. Both imply that the solvation of ionic liquids breaks the correlation between ions with same charges. Figure 7.10 shows the RDF and coordination number of ACN around each ion. These RDFs have very similar peak locations, and the first peak only drop slightly as the ACN concentration increases. Since the number of ion pairs are reduced by dilution, the coordination number of ACN around each ion increases in turn. Due to bulky sizes of the ions, the coordination number of ACN around an ion may eventually reach more than 15.

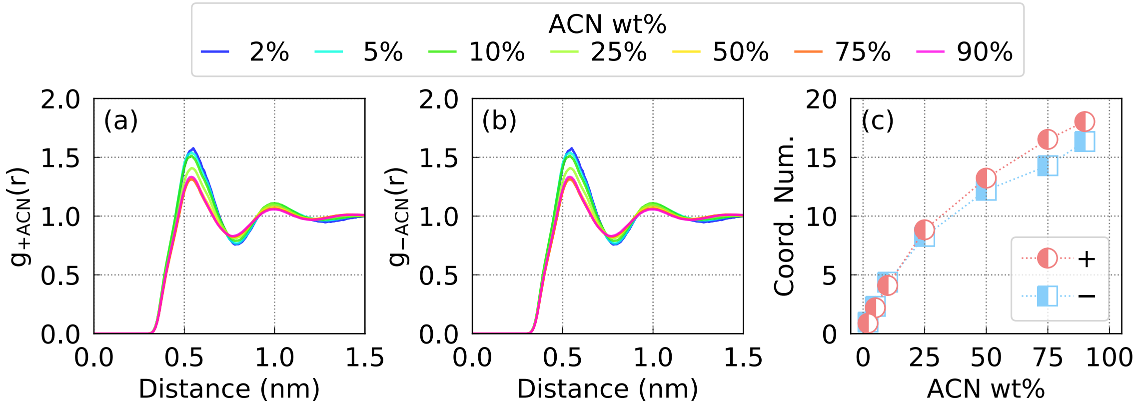

Figure 7.10 (a) RDF of acetonitrile around cation. (b) RDF of anion around anion. (c) Coordination number of acetonitrile around cation (+) and anion (−).

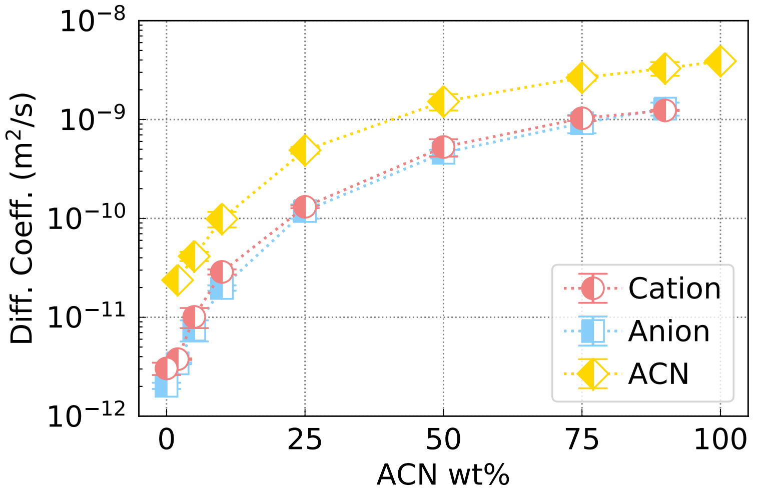

Figure 7.11 Self-diffusion coefficients for ions and acetonitrile in bulk.

To study how the solvation affects ion and solvent dynamics, we calculated self-diffusion coefficients for each ion and solvent. As shown in Figure 7.11, solvation remarkably increases the self-diffusion coefficients of all species. It's also worth noting that the change of diffusivity is more significant in the high ion concentration regime: adding 10 wt% ACN to the neat ionic liquid increases the ion self-diffusion coefficient by about an order of magnitude. This effect also extends to other solvents, as described in our group's previous work on solvating ionic liquids with 22 solvents.[63] Another interesting observation is that cation and anion have very similar diffusion coefficients for all ACN concentrations. This could be attributed to the strong correlation between cation and anion even when they are solvated, which we've shown earlier in Figure 7.9.

### 7.3.3 Capacitance, EDL structure and ion dynamics of solvated IL on carbon electrodes

Differential capacitance has been used in computational works to illustrate the capacitance behavior as a function of biased potential, and to compare with experimental capacitance. Bell-shaped differential capacitance curves are presented in Figure 7.12(a) for systems with 25 wt% ACN. It's obvious that both edges surfaces exhibit capacitance higher than other carbon surfaces. Our previous work indicates that graphene edge surfaces could break down ion pair association, and induce more efficient counter-ion responds, thereby enhancing EDL capacitance.[180] However, it's not so clear how to determine which graphene edge has higher capacitance, nor to compare the capacitance between non-edge carbon electrodes. For example, the armchair edge has higher differential capacitance than the zigzag edge at positive potentials, but this is reversed when biased with negative potentials.

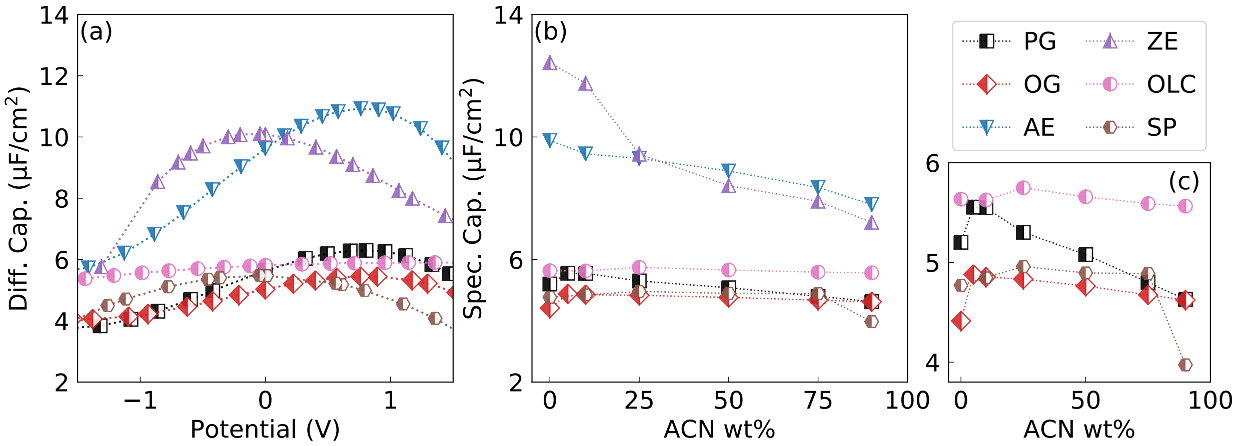

Figure 7.12 (a) Differential capacitance as a function of electric potential for the systems with 25 wt% ACN. (b) Specific capacitance (−1V to 1V) as a function of ACN weight percentage. (c) Specific capacitance excluding the graphene edges. The abbreviation in the legend strands for pristine graphene (PG), oxidized graphene (OG), graphene armchair edge (AE), graphene zigzag edge (ZE), onion-like carbon (OLC), and slit-pore carbon (SP).

In order to quantify the effects of dilution on the capacitance, and also to compare the capacitance between different systems, we calculated the specific capacitance from −1 V to 1V, as shown in Figure 7.12(b-c). This potential range covers most of our simulation data points, and the differential capacitance estimated from polynomial fittings is stable in this range. The specific capacitance is plotted as a function of ACN weight percentage. Again, we see that the graphene edges have the highest capacitance. The zigzag edge has higher specific capacitance than the armchair edge when the ion concentration is high, but exhibits slightly lower specific capacitance in the dilute regime. In addition, the specific capacitance of graphene edges decreases monotonically when adding more ACN. In contrast, the specific capacitance of non-edge electrode has a nonmonotonic relationship with the ACN weight percentage. The curves in Figure 7.12(c) all exhibit maximum values at intermediate concentration. It is shown that, for these non-edge electrodes, by diluting the ionic liquid electrolyte with ACN, the specific capacitance would first increase and then decrease. As mentioned in the introduction, Bozym, Uralcan and their coworkers have also shown this capacitance behavior on glassy carbon and graphene.[68,69] Moreover, classical density functional theory work also demonstrates that adding polar additive to neat ionic liquids could boost the capacitance of slit-pore carbons.[182] Here, we further demonstrate that the enhancement of capacitance through dilution of the ionic liquid electrolyte is not individual, but rather common to carbon materials, including basal plane graphene, onion-like carbons, and slit-pore carbons.

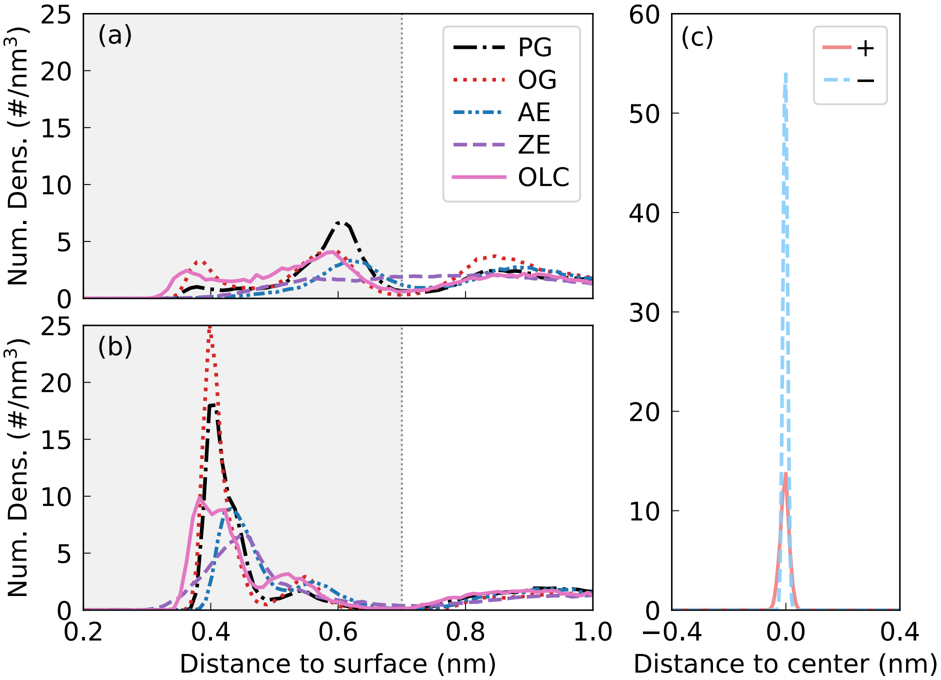

Figure 7.13 COM number densities of (a) cation and (b) anion near non-slit electrode surfaces. (c) COM number densities of cation (+) and anion (−) inside slit-pore. All of the electrodes were charged with 5 μC cm$^{-2}$, and the electrolyte here contains 25 wt% ACN.

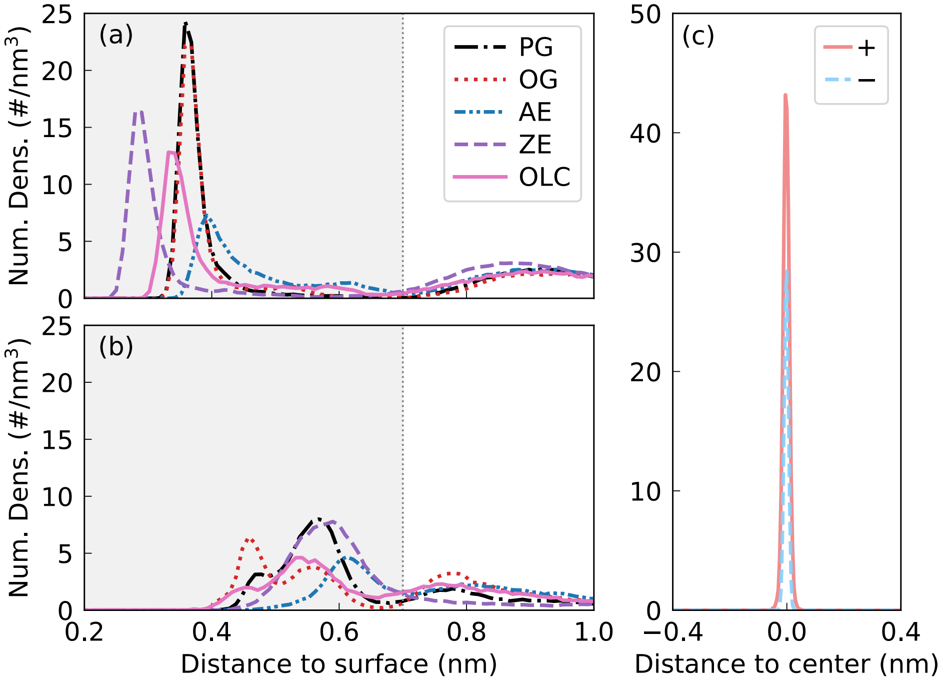

Figure 7.14 COM number densities of (a) cation and (b) anion near non-slit electrode surfaces. (c) COM number densities inside a 0.8-nm slit-pore (−5 μC cm$^{-2}$). Electrolyte contains 25 wt% ACN.

In an effort to understand why the graphene edges behave differently from other non-edge electrodes and the appearance of capacitance maximum on those non-edge surfaces, careful investigations of the EDL formed near the electrode surface are needed. Figure 7.13 shows the center-of-mass (COM) number density profiles of ions near an open electrode surface or confined in the 0.8-nm slit-pore, where the surface charge density is 5 μC cm$^{-2}$. We notice that the first counter-ion peaks (Figure 7.13(b)) all lie within 0.7 nm from the electrode surface. The peaks on the graphene basal planes, i.e. pristine graphene and oxidized graphene, located around 0.4 nm, are high and narrow. The counter-ion peak on the oxidized graphene is higher than the pristine graphene due to the higher affinity of the hydroxyl groups to the anions.[195] The counter-ion distributions on the edge surfaces are more dispersive, and the peaks are lower. The peaks also shift to larger distances than those on the basal planes. Similarly, OLC has a peak around 0.4 nm, but the peak is lower and broader compared to those on the basal planes. The ions confined in the 0.8 nm slit-pore form a thin layer around the slit center, as shown in Figure 7.13(c), where the ion distribution is just a sharp peak. Comparing the planar surfaces to the non-planar surfaces, we infer that ions tend to form thin layers on planar surfaces, but these structured layers are disrupted when the surface is rough (graphene edges) or has curvature (OLC). Since the slit-pore model is also constructed by two planar surfaces, this effect gets magnified, and the counter-ion peak height reaches almost 3 times of that on the pristine graphene. Similar phenomenon is observed when the surfaces are negatively charged. Shown in Figure 7.14, peaks in the number density distributions are sharper on planar surfaces, and more dispersive on edge surfaces or OLC.

Besides counter-ions, co-ions are also presented in the EDL. Figure 7.13(a) illustrates that co-ions have low peaks around 0.4 nm, but stronger peaks at around 0.6 nm. This alternating layering of counter-ions and co-ions near an electrode surface is typical for ionic-liquid-based supercapacitors, and leads to charge overscreening.[181] Due to strong ion correlations, the charge in the first absorbed layer overscreens that on the electrode surface, and the subsequent layer again overcompensates the charge in its previous layer. This effect also exists inside the slit-pores. As shown in Figure 7.13(c) and Figure 7.14(c), each counter-ion peak is accompanied by a co-ion peak with a lower height. In consequence, only a fraction of the adsorbed counter-ions is actually used in the charge storage. Several reports indicate that the reduction of the charge overscreening effect increases the capacitance and optimizes charge storage of supercapacitors.[230–232]

To quantify the charge overscreening effect, we define a charge screening factor $F_S(z)$. For the basal planes and edge planes, the charge screening factor is defined as:

$$F_s(z) = -\frac{1}{\sigma}\int_0^z \left(\rho(z') - \rho_{pzc}(z')\right) \mathrm{d}z' \tag{7.1}$$

where $\rho(z')$ is the charge density in the direction perpendicular to the electrode surface, and $\rho_{pzc}(z')$ is the charge density at potential of zero charge (PZC), and $\sigma$ is the surface charge density. Similarly, the charge screening factor for OLC is defined as:

$$F_s(z) = -\frac{1}{R^2\sigma}\int_R^r r'^2 \left(\rho(r') - \rho_{pzc}(r')\right) \mathrm{d}r' \tag{7.2}$$

where $\rho(r')$ is the charge distribution in the radial direction, and $\rho_{pzc}(r')$ is the charge distribution at PZC, and $R$ is the radius of the outmost layer of OLC. By definition, the screening factor exceeds 1 if the charge overscreening happens at the interface. The screening factors for different surfaces excluding the slit-pore carbon are shown in Figure 7.15.

With the neat ionic liquid as the electrolyte, all surfaces exhibit a charge overscreening behavior, but the magnitudes are different. We observe high peaks (first peak height around 3.5) on the planar surfaces (Figure 7.15(a-b)) and the spherical surface (Figure 7.15(e)). But the peaks are lower on the edge surfaces as shown in Figure 7.15(c-d). This is likely due to the roughness introduced by the edge surfaces, which breaks down ion correlations and makes the ion distribution more localized (Figure 7.13), hence reducing the charge overscreening effect. As a result, the graphene edges offer higher capacitance than other non-edge electrodes. In addition, we notice that adding ACN into the system reduces the screening factor. The screening factors shown in Figure 7.15 all decrease as the ACN weight percentage increases. Particularly, for the planar surfaces and spherical surface (Figure 7.15(a, b, e)), the screening factor of the first peak drops from around 3.5 to around 2. In contrast, the change of screening factors on edge surfaces is less significant. In Figure 6(c-d), the addition of solvent only decreases the screening factor slightly, and gradually shifts the peaks to a larger distance in the meantime. The reason could be that the ion correlations have already been mostly broken by the rough surfaces, and the effect of solvation is limited in this case.

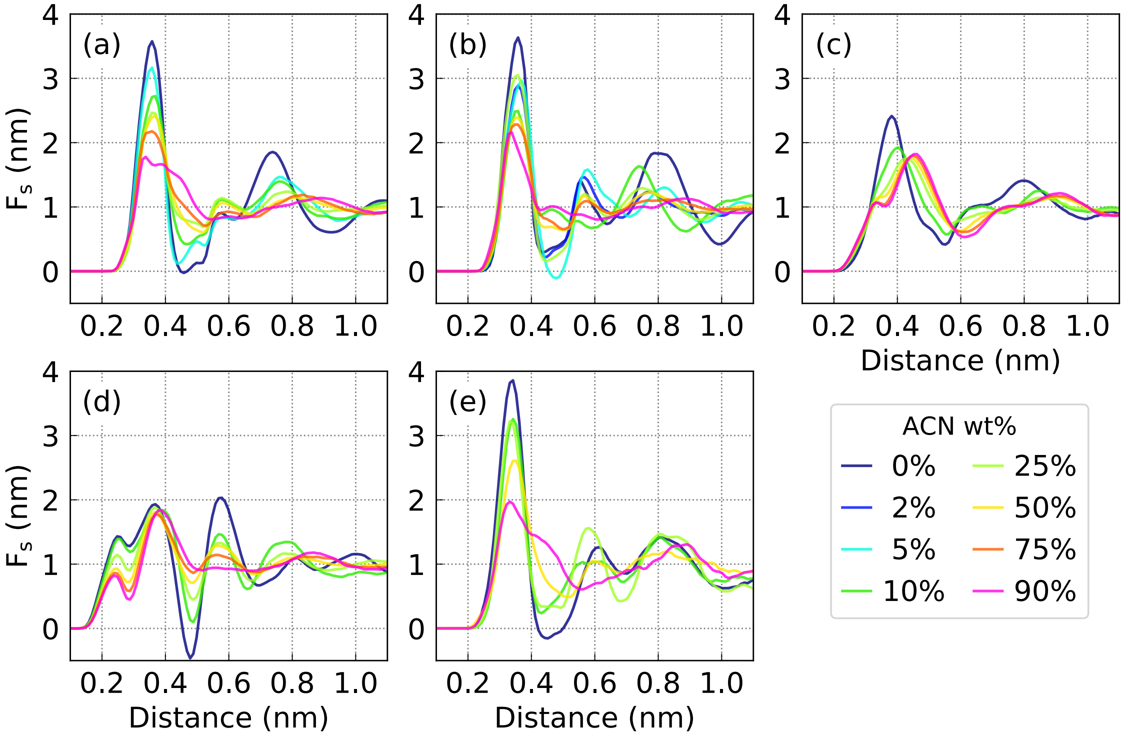

Figure 7.15 Charge screening factor as a function of distance on electrode surfaces with charge density of 5 μC cm$^{-2}$: (a) pristine graphene; (b) oxidized graphene; (c) armchair edge; (d) zigzag edge; (e) onion-like carbon.

For ions confined in the 0.8-nm slit-pore, since they only form a single layer inside the pore, we calculate the fraction of counter-ions to illustrate the overscreening effect.

$$F_{Counter-ion} = \frac{N_{Counter-ion}}{N_{Counter-ion} + N_{Co-ion}} \tag{8}$$

where $N_{Counter-ion}$ and $N_{Co-ion}$ are the numbers of counter-ion and co-ions confined in the slit-pore respectively. Ideally, the charge storage is most efficient when the pore only absorbs the counter-ions, which means the fraction of counter-ion is 1. But due to the strong ion correlations, the fraction might become lower than 1. Figure 7.16 shows the fraction of counter-ions at different solvent percentages. Initially, the slit-pore contains a mixture of counter-ions and co-ions when the electrolyte is the neat ionic liquid. Dilution of the electrolyte breaks the ion pairing inside the slit-pore. The fraction of counter-ions gradually increases as more ACN is added, and finally reaches 1 when ACN weight percentage reaches 90%.

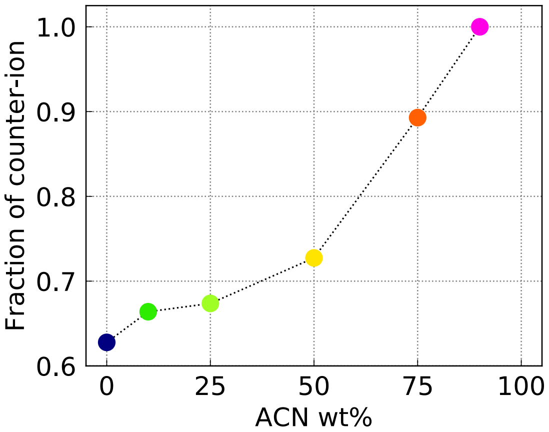

Figure 7.16 Fraction of counter-ion inside the 0.8-nm slit-pore as a function of acetonitrile weight percentage. The surface charge density is 5 μC $cm^{-2}$.

As stated previously in this section, the decrease of screening factor could increase the capacitance. In one aspect, the addition of solvent in the ionic liquid electrolyte could improve the capacitance by decreasing the charge overscreening effect. Nevertheless, we also need to consider that the effect of dilution of ion concentrations. As shown in Figure 7.17 and 7.18, the ion concentrations on an open surface or inside the slit-pore are reduced when the electrolyte becomes more dilute. Thus, adding solvent into the ionic liquid electrolyte introduces two competing effects: while the decreased overscreening effect tend to increase the capacitance, the dilution of ion concentrations decreases the capacitance. And the aforementioned non-monotonic capacitance behavior on pristine graphene, oxidized graphene, onion-like carbon and slit-pore, is the result of this competition. In the high ion concentration regime, the decreased charge overscreening effect is the dominant reason for the increase capacitance, and the dilution of ion concentration explains for the drop of capacitance in the low ion concentration regime. As for the graphene edges, since the charge overscreening effect is already low even for the neat ionic liquid, the dilution effect dominates throughout the solvent percentage range. Consequently, the capacitance of graphene edges decreases monotonically as the solvent concentration increases.

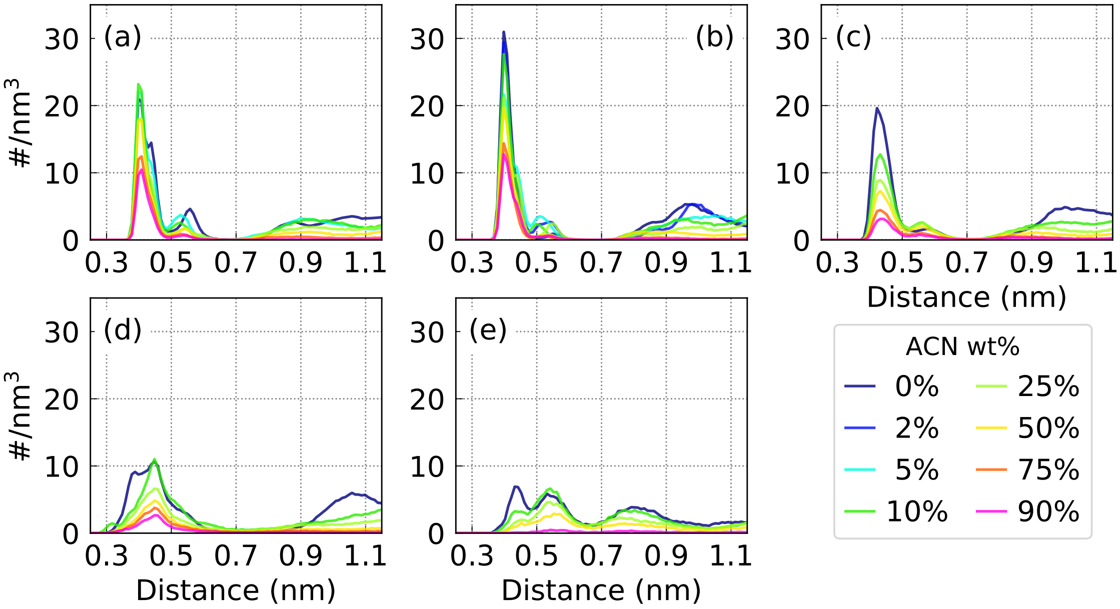

Figure 7.17 COM number density of counter-ions on surfaces with a surface charge density of 5 μC cm$^{-2}$: (a) pristine graphene; (b) oxidized graphene; (c) armchair edge; (d) zigzag edge; (e) onion-like carbon.

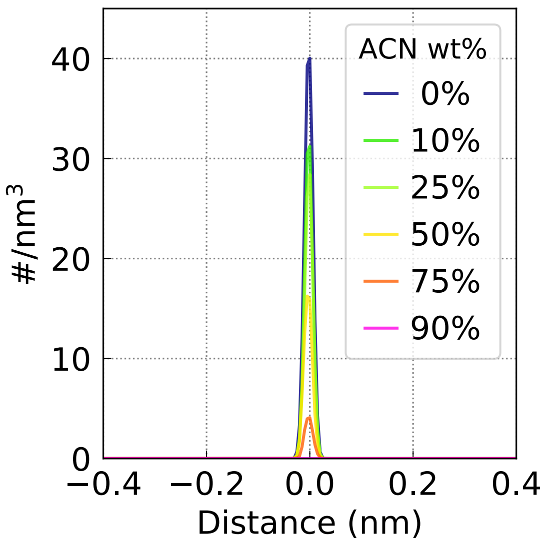

Figure 7.18 COM number density of counter-ions inside the 0.8-nm slit-pore with a surface charge density of 5 μC cm$^{-2}$.

To characterize the ion dynamics at the interface, we calculated the ion self-diffusion coefficient using Einstein relation in the directions not bounded by the electrode surface. As shown in Figure 7.13, we consider the region within 0.7 nm from the electrode surface as the interfacial region for non-slit-pore electrodes, and the region encompassed by the two slits as the interfacial region for the slit-pore electrode. Since ions may enter and exit the interfacial region during each simulation run, we only take into account the ions that stayed in the region throughout each production run.

Figure 7.19 shows the ion and solvent self-diffusion coefficients at the interface as a function of ACN weight percentage. Compared to the bulk diffusion coefficients in Figure 7.11, the confinement generally slows down the ion and solvent dynamics. Especially in the high ion concentration regime, ion self-diffusion coefficients are 1 to 2 orders of magnitude lower than those in bulk. The addition of solvent also drastically increases the diffusion coefficients for all species: the improvement of diffusion coefficients from a neat ionic liquid to a dilute solution (90 wt% ACN) could be more than 3 orders of magnitude. It's also worth noting that the increment of diffusion coefficients is more significant in the concentrated regime than in the dilute regime. For example, adding 25 wt% ACN into the neat ionic liquid increases the ion diffusion coefficients by almost 2 orders of magnitude. But adding another 25 wt% ACN only improves the diffusivity by less than 1 order of magnitude.

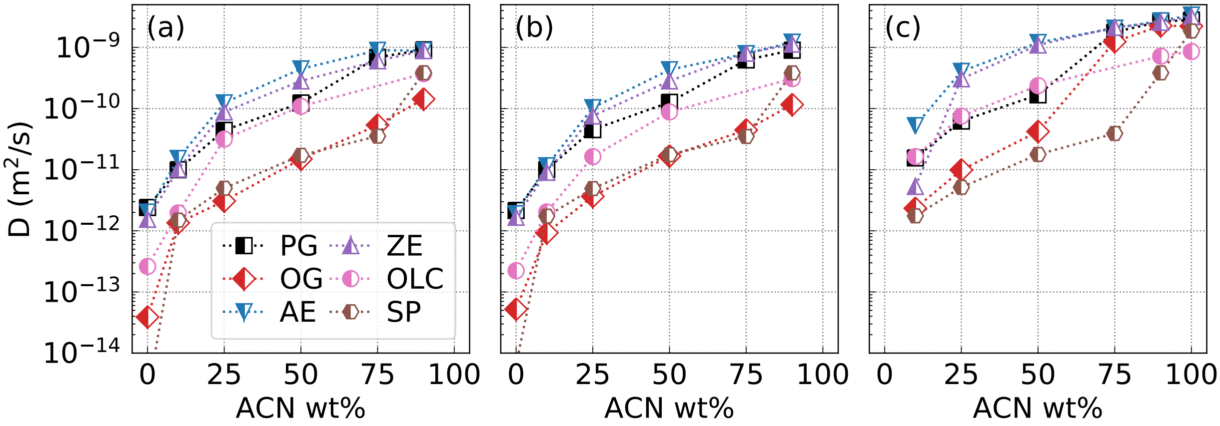

Figure 7.19 Self-diffusion coefficient of (a) cation, (b) anion, and (c) acetonitrile at the interface as a function of acetonitrile weight percentage.

An optimum supercapacitor should have both high energy density and power density. From our previous discussion on capacitance, the capacitance on non-edge carbon electrodes exhibit a capacitance maximum when the ion liquid electrolyte is solvated. Thus, adding certain amount of solvent into the neat ionic liquid could both boost their energy density and power density. As for the graphene edges, their capacitance decreases monotonically with the solvent concentration, but the ion dynamics improves notably. And adding solvent into the ionic liquid electrolyte offers a comprised combination of energy density and power density.

## 7.4 Conclusions

In this chapter, we discussed the effects of electrolyte composition and concentration on the performance of supercapacitors. First, the effects of cation size were studied. Our findings show good agreement between QENS-derived dynamics and MD-derived ion diffusivities: smaller ions accumulate in larger densities and move through pores at faster rates for the imidazolium-based ionic liquids studied here. In addition, MD simulations of solvated ionic liquids on carbon electrodes suggest that diluting the ionic liquid electrolyte with acetonitrile has two competing effects on capacitance. On one hand, the solvent weakens ion correlations and reduces the charge overscreening effect, which increases the capacitance. On the other hand, diluting the electrolyte also diminishes absorbed ion concentrations, which decreases the capacitance. As a result of this competition, non-edge carbon surfaces, including pristine graphene, oxidized graphene, carbon onion, and slit-pore carbon, exhibit a capacitance maximum during dilution. For graphene edges, since the charge overscreening effect is already moderated by their rough surfaces, the diluting effect plays a major role, and the capacitance decreases monotonically with solvent concentration. Moreover, the addition of solvent drastically improves ion and solvent dynamics in the bulk and at interfaces, especially in the high ion concentration regime. Our work demonstrates the comprehensive effects of electrolyte composition and concentration on the performance of carbon supercapacitors, and provides computational supports for better designs of supercapacitors with both high energy density and power density.

# CHAPTER VIII

# CONCLUSIONS AND FUTURE WORK

## 8.1 Conclusions

Molecular dynamics simulations have been used to evaluated the performance of ionic-liquid-carbon-based electric double layer capacitor. On the electrode side, we investigated the effects of different surface chemistries and geometries on the capacitance and ion dynamics of carbon-based materials. On the electrolyte side, we evaluated how changing the cation size and dilution of an ionic liquid could change the performance of supercapacitors. Our work combined various collaborations, including joint density functional calculations and experimental measurements, such as QENS, SANS, and X-ray scattering. Our integrated approach extended the knowledge about the charging mechanisms of IL-carbon-based EDLCs, and provided guidance for better designs of future energy storage devices.

In Chapter IV, the effects of nitrogen doping on the capacitance of graphene supercapacitor was analyzed by MD simulations and JDFT calculations. It is found that nitrogen-doping had relatively small effects on the EDL capacitance for the doping concentrations examined. However, the graphitic and pyridinic doping configurations significantly increased the quantum capacitance. The pyrrolic doping configuration had similar quantum capacitance to that of pristine graphene. Thus, doping nitrogen with graphitic or pyridinic configurations could greatly increase the total capacitance by increasing quantum capacitance. Given that the pyridinic and pyrrolic nitrogen doping configurations have higher thermal stability than the graphitic doping configuration, a good strategy is to dope the nitrogen with the pyridinic configuration and avoid the pyrrolic configuration.

In Chapter V, we studied the capacitance of graphene edge planes in contact with an electrolyte. MD simulations with explicit electrolytes revealed that graphene edges have higher EDL capacitance than the graphene basal plane due to two reasons: the surface inhomogeneity of edge surfaces favored the adsorption of counter-ions; the edge planes had higher solvent-accessible surface area. In addition, the joint density functional theory calculations with implicit solvation models showed that the zigzag edge had higher total capacitance than the armchair edge and the basal plane. The quantum capacitance, dielectric screening, and EDL responses all played important roles on the total capacitance. Our theoretical work provided a complete picture of various factors influencing the capacitive performance of graphene edges, and suggested that the zigzag edge could potentially increase the capacitance of graphene-based supercapacitors.

In Chapter VI, we determined the influence of surface chemistry on electrosorption and capacitance of supercapacitors with nonporous and porous carbon electrodes. On nonporous graphene electrodes, the neat ionic liquid and solvated ionic liquids all showed decreased capacitance when the surfaces were hydroxylated. In the neat ionic liquid case, the hydroxyl groups either diluted the counter-ion accumulation or attracted co-ions into the EDL, which all decreased the capacitance. In the case of solvated ionic liquids, the distribution and orientation of acetonitrile across the system exerted vital influence on the capacitance, especially on the positive hydroxyl-free electrode. Furthermore, MD simulations of ion mobility with respect to electrode surface in the lateral and perpendicular directions revealed significantly slower diffusion performance on oxidized surfaces. In the case of ion confinement in CDCs with small (0.8 nm) pores, oxygen-rich CDC pore surfaces allowed [TFSI$^-$] anions to align parallel to pore surfaces and decreased electrolyte density in uncharged pores. Subsequently, ions obtained greater room and mobility during electrosorption, and oxidized porous electrodes demonstrated higher capacitance, faster ion dynamics, and better rate handling ability. In the case of ion confinement in bimodal CDCs, the oxidized pore strongly attracted ions, which creates space for fast diffusion of ions in pore centers. But the oxidized pore failed to accommodate ions and reorganize ions into dense configurations inside the pore, and thus exhibited lower capacitance compared to defunctionalized pores.

Finally, in Chapter VII, we discussed the effects of electrolyte composition and concentration on the performance of supercapacitors. First, the effects of cation size were studied. Our findings show good agreement between QENS-derived dynamics and MD-derived ion diffusivities: smaller ions accumulate in larger densities and move through pores at faster rates for the imidazolium-based ionic liquids studied here. In addition, MD simulations of solvated ionic liquids on carbon electrodes uncover that diluting the ionic liquid electrolyte with acetonitrile has two competing effects on capacitance. On one hand, the solvent weakens ion correlations and reduces the charge overscreening effect, which increases the capacitance. On the other hand, diluting the electrolyte also diminishes absorbed ion concentrations, which decreases the capacitance. As a result of this competition, non-edge carbon surfaces, including pristine graphene, oxidized graphene, carbon onion, and slit-pore carbon, exhibit a capacitance maximum during dilution. For graphene edges, since the charge overscreening effect is already moderated by their rough surfaces, the diluting effect plays a major role, and the capacitance decreases monotonically with solvent concentration. Moreover, the addition of solvent drastically improves ion and solvent dynamics in the bulk and at interfaces, especially in the high ion concentration regime. Our work demonstrates the comprehensive effects of electrolyte composition and concentration on the performance of ionic-liquid-carbon supercapacitors, and provides computational supports for better designs of supercapacitors with both high energy density and power density.

## 8.2 Recommended Future Work

### 8.2.1 Effects of surface chemistry on MXene-based supercapacitors

MXenes are a class of 2D materials first reported by Naguib et al,[233] which show 2D morphology, ion-intercalation capacity, metallic conductivity, and tunable surface terminations. These properties make them promising electrodes for supercapacitors, where high volumetric capacitance up to 1500 F $cm^{-3}$ was reported in aqueous electrolyte.[234] MXenes are usually referred to as $M_{n+1}X_nT_x$, where M stands for an early transition metal, X stands for carbon and/or nitrogen, and T is the surface terminations, including =O, −OH, −F, etc. Similar to carbon materials, the surface chemistry of MXene makes the charging mechanism of MXene-based supercapacitors complicated, and not fully understood up until now. In aqueous electrolytes, the appearance of redox peaks in cyclic voltammograms suggests pseudocapacitive reactions of surface functional groups.[235] In addition, intercalation of cations between MXene layers was also observed in experimental[236] and computational works.[237] A complete understanding of the charging process, and the effects of surface chemistry requires an integrated approach that combines theoretical calculations, including MD simulation and DFT calculation, and experiments, including electrochemical tests and surface characterization.

### 8.2.2 Effects of electrolyte composition on MXene-based supercapacitors

Currently, most published studies have been on MXene electrodes with aqueous electrolytes,[238] however the effects of electrolyte composition has not been fully understood. Wang et al showed by simply changing the solvent of an electrolyte system, the capacitance of MXene-based supercapacitor drastically increased.[239] This sheds lights on enhancing the capacitance of MXene-based supercapacitors by modifying the electrolyte composition and concentration. MD simulation will be a powerful tool to do this. With the help of software environments, such as MOSDEF,[240] MD simulations can be automated to evaluate a variety of electrolytes at the same time. Our group's previous simulation work used a screening approach to study mixtures of ionic liquids in 22 solvents at a range of concentrations.[171] Similar approaches could be applied to the electrolyte/electrode interfacial systems to find out the optimum solvent type and concentration.

### 8.2.3 Charging and discharging dynamics of EDLCs

Another interesting topic to pursue is to further understand the charging/discharging dynamics of ions at the interface. In this work, we used ion self-diffusion coefficients to represent the mobility of ions at the interface. While the ion self-diffusion is a good indicator of the mobility of the ion itself, the mobility of ions at the interface can be affected by other factors. Particularly, in electrochemical tests and real-life applications, supercapacitors are charged with cyclic potentials. Thus, besides self-diffusion, the ions are also driven by the change of electric potentials on electrodes during the charging/discharging process. In addition, as shown by previous studies, the charging and discharging process can also cause volumetric change of MXene electrodes, which in turn could affect the structure of intercalated/adsorbed ions.[237,241] An investigation of dynamics of charging and discharging process will provide more fundamental insights about the performance of MXene-based supercapacitors.

# REFERENCES

(1) Simon, P.; Gogotsi, Y. Materials for Electrochemical Capacitors. *Nat Mater* **2008**, *7*, 845–854.

(2) Simon, P.; Gogotsi, Y.; Dunn, B. Where Do Batteries End and Supercapacitors Begin? *Science (80-. ).* **2014**, *343*, 1210–1211.

(3) Zhang, L. L.; Zhou, R.; Zhao, X. S. Graphene-Based Materials as Supercapacitor Electrodes. *J. Mater. Chem.* **2010**, *20*, 5983–5992.

(4) Zhu, Y.; Murali, S.; Stoller, M. D.; Ganesh, K. J.; Cai, W.; Ferreira, P. J.; Pirkle, A.; Wallace, R. M.; Cychosz, K. a; Thommes, M.; et al. Carbon-Based Supercapacitors Produced by Activation of Graphene. *Science* **2011**, *332*, 1537–1541.

(5) Gamby, J.; Taberna, P. L.; Simon, P.; Fauvarque, J. F.; Chesneau, M. Studies and Characterisations of Various Activated Carbons Used for Carbon/Carbon Supercapacitors. *J. Power Sources* **2001**, *101*, 109–116.

(6) Lewandowski, A.; Olejniczak, A.; Galinski, M.; Stepniak, I. Performance of Carbon-Carbon Supercapacitors Based on Organic, Aqueous and Ionic Liquid Electrolytes. *J. Power Sources* **2010**, *195*, 5814–5819.

(7) Gogotsi, Y.; Nikitin, A.; Ye, H.; Zhou, W.; Fischer, J. E.; Yi, B.; Foley, H. C.; Barsoum, M. W. Nanoporous Carbide-Derived Carbon with Tunable Pore Size. *Nat. Mater.* **2003**, *2*, 591–594.

(8) Chmiola, J.; Largeot, C.; Taberna, P. L.; Simon, P.; Gogotsi, Y. Monolithic Carbide-Derived Carbon Films for Micro-Supercapacitors. *Science (80-. ).* **2010**, *328*, 480–483.

(9) Zhang, L. L.; Zhao, X. S. Carbon-Based Materials as Supercapacitor Electrodes. *Chem.*

*Soc. Rev.* **2009**, *38*, 2520–2531.

(10) Stoppa, A.; Zech, O.; Kunz, W.; Buchner, R. The Conductivity of Imidazolium-Based Ionic Liquids from (-35 to 195) °c. A. Variation of Cations Alkyl Chain. *J. Chem. Eng. Data* **2010**, *55*, 1768–1773.

(11) Brandt, A.; Pohlmann, S.; Varzi, A.; Balducci, A.; Passerini, S. Ionic Liquids in Supercapacitors. *MRS Bull.* **2013**, *38*, 554–559.

(12) Osti, N. C.; Naguib, M.; Tyagi, M.; Gogotsi, Y.; Kolesnikov, A. I.; Mamontov, E. Evidence of Molecular Hydrogen Trapped in Two-Dimensional Layered Titanium Carbide-Based MXene. *Phys. Rev. Mater.* **2017**, *1*, 024004.

(13) Black, J. M.; Feng, G.; Fulvio, P. F.; Hillesheim, P. C.; Dai, S.; Gogotsi, Y.; Cummings, P. T.; Kalinin, S. V.; Balke, N. Strain-Based in Situ Study of Anion and Cation Insertion into Porous Carbon Electrodes with Different Pore Sizes. *Adv. Energy Mater.* **2014**, *4*.

(14) Qu, L.; Qiao, W. Constant Power Control of DFIG Wind Turbines with Supercapacitor Energy Storage. *IEEE Trans. Ind. Appl.* **2011**, *47*, 359–367.

(15) Bañuelos, J. L.; Feng, G.; Fulvio, P. F.; Li, S.; Rother, G.; Dai, S.; Cummings, P. T.; Wesolowski, D. J. Densification of Ionic Liquid Molecules within a Hierarchical Nanoporous Carbon Structure Revealed by Small-Angle Scattering and Molecular Dynamics Simulation. *Chem. Mater.* **2014**, *26*, 1144–1153.

(16) Miller, J. R.; Simon, P. Materials Science. Electrochemical Capacitors for Energy Management. *Science* **2008**, *321*, 651–652.

(17) Zhan, C.; Lian, C.; Zhang, Y.; Thompson, M. W.; Xie, Y.; Wu, J.; Kent, P. R. C.; Cummings, P. T.; Jiang, D. E.; Wesolowski, D. J. Computational Insights into Materials and Interfaces for Capacitive Energy Storage. *Adv. Sci.* **2017**, *4*.

(18) Zhang, W.; Zhu, S.; Luque, R.; Han, S.; Hu, L.; Xu, G. Recent Development of Carbon Electrode Materials and Their Bioanalytical and Environmental Applications. *Chem. Soc. Rev.* **2016**, *45*, 715–752.

(19) McCreery, R. L. Advanced Carbon Electrode Materials for Molecular Electrochemistry. *Chem. Rev.* **2008**, *108*, 2646–2687.

(20) Futaba, D. N.; Hata, K.; Yamada, T.; Hiraoka, T.; Hayamizu, Y.; Kakudate, Y.; Tanaike, O.; Hatori, H.; Yumura, M.; Iijima, S. Shape-Engineerable and Highly Densely Packed Single-Walled Carbon Nanotubes and Their Application as Super-Capacitor Electrodes. *Nat. Mater.* **2006**, *5*, 987–994.

(21) Pech, D.; Brunet, M.; Durou, H.; Huang, P.; Mochalin, V.; Gogotsi, Y.; Taberna, P.-L.; Simon, P. Ultrahigh-Power Micrometre-Sized Supercapacitors Based on Onion-like Carbon. *Nat. Nanotechnol.* **2010**, *5*, 651–654.

(22) McDonough, J. K.; Gogotsi, Y. Carbon Onions: Synthesis and Electrochemical Applications. *Interface Mag.* **2016**, *22*, 61–66.

(23) Novoselov, K. S.; Geim, a K.; Morozov, S. V; Jiang, D.; Zhang, Y.; Dubonos, S. V; Grigorieva, I. V; Firsov, a a. Electric Field Effect in Atomically Thin Carbon Films. *Science* **2004**, *306*, 666–669.

(24) Meyer, J. C.; Geim, A. K.; Katsnelson, M. I.; Novoselov, K. S.; Booth, T. J.; Roth, S. The Structure of Suspended Graphene Sheets. *Nature* **2007**, *446*, 60–63.

(25) Allen, M. J.; Tung, V. C.; Kaner, R. B. Honeycomb Carbon: A Review of Graphene. *Chem. Rev.* **2010**, *110*, 132–145.

(26) Pensado, A. S.; Malberg, F.; Gomes, M. F. C.; Pádua, A. a. H.; Fernández, J.; Kirchner, B. Interactions and Structure of Ionic Liquids on Graphene and Carbon Nanotubes Surfaces.

*RSC Adv.* **2014**, *4*, 18017.

(27) Cheng, Q.; Tang, J.; Ma, J.; Zhang, H.; Shinya, N.; Qin, L. C. Graphene and Nanostructured MnO2 Composite Electrodes for Supercapacitors. *Carbon N. Y.* **2011**, *49*, 2917–2925.

(28) Compton, O. C.; Nguyen, S. T. Graphene Oxide, Highly Reduced Graphene Oxide, and Graphene: Versatile Building Blocks for Carbon-Based Materials. *Small* **2010**, *6*, 711–723.

(29) Dreyer, D. R.; Park, S.; Bielawski, C. W.; Ruoff, R. S. The Chemistry of Graphene Oxide. *Chem. Soc. Rev.* **2010**, *39*, 228–240.

(30) Xu, B.; Yue, S.; Sui, Z.; Zhang, X.; Hou, S.; Cao, G.; Yang, Y. What Is the Choice for Supercapacitors: Graphene or Graphene Oxide? *Energy Environ. Sci.* **2011**, *4*, 2826.

(31) Buglione, L.; Chng, E. L. K.; Ambrosi, A.; Sofer, Z.; Pumera, M. Graphene Materials Preparation Methods Have Dramatic Influence upon Their Capacitance. *Electrochem. commun.* **2012**, *14*, 5–8.

(32) Shim, Y.; Jung, Y.; Kim, H. J. Graphene-Based Supercapacitors: A Computer Simulation Study. *J. Phys. Chem. C* **2011**, *115*, 23574–23583.

(33) Feng, G.; Zhang, J. S.; Qiao, R. Microstructure and Capacitance of the Electrical Double Layers at the Interface of Ionic Liquids and Planar Electrodes. *J. Phys. Chem. C* **2009**, *113*, 4549–4559.

(34) Vatamanu, J.; Cao, L.; Borodin, O.; Bedrov, D.; Smith, G. D. On the Influence of Surface Topography on the Electric Double Layer Structure and Differential Capacitance of Graphite/Ionic Liquid Interfaces. *J. Phys. Chem. Lett.* **2011**, *2*, 2267–2272.

(35) Merlet, C.; Péan, C.; Rotenberg, B.; Madden, P. A.; Simon, P.; Salanne, M. Simulating

Supercapacitors: Can We Model Electrodes as Constant Charge Surfaces? *J. Phys. Chem. Lett.* **2013**, *4*, 264–268.

(36) Kislenko, S. a; Samoylov, I. S.; Amirov, R. H. Molecular Dynamics Simulation of the Electrochemical Interface between a Graphite Surface and the Ionic Liquid BMIM PF6. *Phys. Chem. Chem. Phys.* **2009**, *11*, 5584–5590.

(37) Vatamanu, J.; Borodin, O.; Smith, G. D. Molecular Insights into the Potential and Temperature Dependences of the Differential Capacitance of a Room-Temperature Ionic Liquid at Graphite Electrodes. **2010**, No. Md, 14825–14833.

(38) Kim, Y. J.; Yang, C. M.; Park, K. C.; Kaneko, K.; Kim, Y. A.; Noguchi, M.; Fujino, T.; Oyama, S.; Endo, M. Edge-Enriched, Porous Carbon-Based, High Energy Density Supercapacitors for Hybrid Electric Vehicles. *ChemSusChem* **2012**, *5*, 535–541.

(39) Pope, M. A.; Aksay, I. A. Four-Fold Increase in the Intrinsic Capacitance of Graphene through Functionalization and Lattice Disorder. *J. Phys. Chem. C* **2015**, *119*, 20369–20378.

(40) Biel, B.; Blase, X.; Triozon, F.; Roche, S. Anomalous Doping Effects on Charge Transport in Graphene Nanoribbons. *Phys. Rev. Lett.* **2009**, *102*, 1–4.

(41) Wietecha, M. S.; Zhu, J.; Gao, G.; Wang, N.; Feng, H.; Gorring, M. L.; Kasner, M. L.; Hou, S. Platinum Nanoparticles Anchored on Chelating Group-Modified Graphene for Methanol Oxidation. *J. Power Sources* **2012**, *198*, 30–35.

(42) Gammon, W. J.; Kraft, O.; Reilly, a. C.; Holloway, B. C. Experimental Comparison of N(1s) X-Ray Photoelectron Spectroscopy Binding Energies of Hard and Elastic Amorphous Carbon Nitride Films with Reference Organic Compounds. *Carbon N. Y.* **2003**, *41*, 1917–1923.

(43) Zhao, L.; He, R.; Rim, K. T.; Schiros, T.; Kim, K. S.; Zhou, H.; Gutiérrez, C.; Chockalingam, S. P.; Arguello, C. J.; Pálová, L.; et al. Visualizing Individual Nitrogen Dopants in Monolayer Graphene. *Science* **2011**, *333*, 999–1003.

(44) Jeong, H. M.; Lee, J. W.; Shin, W. H.; Choi, Y. J.; Shin, H. J.; Kang, J. K.; Choi, J. W. Nitrogen-Doped Graphene for High-Performance Ultracapacitors and the Importance of Nitrogen-Doped Sites at Basal Planes. *Nano Lett.* **2011**, *11*, 2472–2477.

(45) Xia, J.; Chen, F.; Li, J.; Tao, N. Measurement of the Quantum Capacitance of Graphene. *Nat. Nanotechnol.* **2009**, *4*, 505–509.

(46) Stoller, M. D.; Magnuson, C. W.; Zhu, Y.; Murali, S.; Suk, J. W.; Piner, R.; Ruoff, R. S. Interfacial Capacitance of Single Layer Graphene. *Energy Environ. Sci.* **2011**, *4*, 4685.

(47) Paek, E.; Pak, a. J.; Hwang, G. S. A Computational Study of the Interfacial Structure and Capacitance of Graphene in [BMIM][PF6] Ionic Liquid. *J. Electrochem. Soc.* **2012**, *160*, A1–A10.

(48) Gogotsi, Y.; Simon, P. True Performance Metrics in Electrochemical Energy Storage. *Science (80-. ).* **2011**, *334*, 917–918.

(49) Dyatkin, B.; Gogotsi, Y. Effects of Structural Disorder and Surface Chemistry on Electric Conductivity and Capacitance of Porous Carbon Electrodes. *Faraday Discuss.* **2014**, *172*, 139–162.

(50) Presser, V.; Heon, M.; Gogotsi, Y. Carbide-Derived Carbons - from Porous Networks to Nanotubes and Graphene. *Adv. Funct. Mater.* **2011**, *21*, 810–833.

(51) Merlet, C.; Rotenberg, B.; Madden, P. A.; Taberna, P. L.; Simon, P.; Gogotsi, Y.; Salanne, M. On the Molecular Origin of Supercapacitance in Nanoporous Carbon Electrodes. *Nat Mater* **2012**, *11*, 306–310.

(52) Frolov, A. I.; Kirchner, K.; Kirchner, T.; Fedorov, M. V. Molecular-Scale Insights into the Mechanisms of Ionic Liquids Interactions with Carbon Nanotubes. *Faraday Discuss.* **2012**, *154*, 235.

(53) Wood, B. C.; Ogitsu, T.; Otani, M.; Biener, J. First-Principles-Inspired Design Strategies for Graphene-Based Supercapacitor Electrodes. *J. Phys. Chem. C* **2014**, *118*, 4–15.

(54) Li, S.; Feng, G.; Cummings, P. T. Interfaces of Dicationic Ionic Liquids and Graphene: A Molecular Dynamics Simulation Study. *J. Phys. Condens. Matter* **2014**, *26*, 284106.

(55) Wishart, J. F. Energy Applications of Ionic Liquids. *Energy Environ. Sci.* **2009**, *2*, 956.

(56) Zhu, Q.; Song, Y.; Zhu, X.; Wang, X. Ionic Liquid-Based Electrolytes for Capacitor Applications. *J. Electroanal. Chem.* **2007**, *601*, 229–236.

(57) Largeot, C.; Portet, C.; Chmiola, J.; Taberna, P. L.; Gogotsi, Y.; Simon, P. Relation between the Ion Size and Pore Size for an Electric Double-Layer Capacitor. *J. Am. Chem. Soc.* **2008**, *130*, 2730–2731.

(58) Lin, R.; Huang, P.; Ségalini, J.; Largeot, C.; Taberna, P. L.; Chmiola, J.; Gogotsi, Y.; Simon, P. Solvent Effect on the Ion Adsorption from Ionic Liquid Electrolyte into Sub-Nanometer Carbon Pores. *Electrochim. Acta* **2009**, *54*, 7025–7032.

(59) Sheng, K.; Sun, Y.; Li, C.; Yuan, W.; Shi, G. Ultrahigh-Rate Supercapacitors Based on Eletrochemically Reduced Graphene Oxide for Ac Line-Filtering. *Sci. Rep.* **2012**, *2*, 247.

(60) Béguin, F.; Presser, V.; Balducci, A.; Frackowiak, E. Carbons and Electrolytes for Advanced Supercapacitors. *Adv. Mater.* **2014**, *26*, 2219–2251.

(61) Zhong, C.; Deng, Y.; Hu, W.; Qiao, J.; Zhang, L.; Zhang, J. A Review of Electrolyte Materials and Compositions for Electrochemical Supercapacitors. *Chem. Soc. Rev.* **2015**, *44*, 7484–7539.

(62) Ruiz, V.; Huynh, T.; Sivakkumar, S. R.; Pandolfo, A. G. Ionic Liquid-Solvent Mixtures as Supercapacitor Electrolytes for Extreme Temperature Operation. *RSC Adv.* **2012**, *2*, 5591–5598.

(63) Sacci, R. L.; Matsumoto, R.; Thompson, M. W.; Sanders, N. C.; Cummings, P. T. Scalable Screening of Soft Matter: A Case Study of Mixtures of Ionic Liquids and Organic Solvents. *J. Phys. Chem. B* **2019**, acs.jpcb.8b11527.

(64) Chaban, V. V.; Voroshylova, I. V.; Kalugin, O. N.; Prezhdo, O. V. Acetonitrile Boosts Conductivity of Imidazolium Ionic Liquids. *J. Phys. Chem. B* **2012**, *116*, 7719–7727.

(65) Weingarth, D.; Noh, H.; Foelske-Schmitz, A.; Wokaun, A.; Kötz, R. A Reliable Determination Method of Stability Limits for Electrochemical Double Layer Capacitors. *Electrochim. Acta* **2013**, *103*, 119–124.

(66) Liu, W.; Yan, X.; Lang, J.; Xue, Q. Effects of Concentration and Temperature of EMIMBF 4/Acetonitrile Electrolyte on the Supercapacitive Behavior of Graphene Nanosheets. *J. Mater. Chem.* **2012**, *22*, 8853–8861.

(67) Li, S.; Zhang, P.; Fulvio Pasquale, F.; Hillesheim Patrick, C.; Feng, G.; Dai, S.; Cummings Peter, T. Enhanced Performance of Dicationic Ionic Liquid Electrolytes by Organic Solvents. *J. Phys. Condens. Matter* **2014**, *26*, 284105.

(68) Bozym, D. J.; Uralcan, B.; Limmer, D. T.; Pope, M. A.; Szamreta, N. J.; Debenedetti, P. G.; Aksay, I. A. Anomalous Capacitance Maximum of the Glassy Carbon-Ionic Liquid Interface through Dilution with Organic Solvents. *J. Phys. Chem. Lett.* **2015**, *6*, 2644–2648.

(69) Uralcan, B.; Aksay, I. A.; Debenedetti, P. G.; Limmer, D. T. Concentration Fluctuations and Capacitive Response in Dense Ionic Solutions. *J. Phys. Chem. Lett.* **2016**, *7*, 2333–

2338.

(70) Helmholtz, H. Ueber Einige Gesetze Der Vertheilung Elektrischer Ströme in Körperlichen Leitern Mit Anwendung Auf Die Thierisch-elektrischen Versuche. *Ann. Phys.* **1853**.

(71) Nanjundiah, C. Differential Capacitance Measurements in Solvent-Free Ionic Liquids at Hg and C Interfaces. *J. Electrochem. Soc.* **2006**.

(72) Gouy, M. Sur La Constitution de La Charge Électrique à La Surface d'un Électrolyte. *J. Phys. Théorique Appliquée* **1910**.

(73) David Leonard Chapman. A Contribution to the Theory of Electrocapillarity. *London, Edinburgh Dublin Philos. Mag. J. Sci.* **1913**.

(74) Kornyshev, A. A. Double-Layer in Ionic Liquids: Paradigm Change? *J. Phys. Chem. B* **2007**, *111*, 5545–5557.

(75) Fedorov, M. V; Kornyshev, A. A. Ionic Liquids at Electri Fi Ed Interfaces. **2014**.

(76) Frenkel, D.; Smit, B. Understanding Molecular Simulation: From Algorithms to Applications. 2001, p 664.

(77) Uysal, A.; Zhou, H.; Feng, G.; Lee, S. S.; Li, S.; Fenter, P.; Cummings, P. T.; Fulvio, P. F.; Dai, S.; McDonough, J. K.; et al. Structural Origins of Potential Dependent Hysteresis at the Electrified Graphene/Ionic Liquid Interface. *J. Phys. Chem. C* **2014**, *118*, 569–574.

(78) Li, S.; Van Aken, K. L.; McDonough, J. K.; Feng, G.; Gogotsi, Y.; Cummings, P. T. The Electrical Double Layer of Dicationic Ionic Liquids at Onion-like Carbon Surface. *J. Phys. Chem. C* **2014**, *118*, 3901–3909.

(79) Paek, E.; Pak, A. J.; Hwang, G. S. Curvature Effects on the Interfacial Capacitance of Carbon Nanotubes in an Ionic Liquid. *J. Phys. Chem. C* **2013**, *117*, 23539–23546.

(80) Feng, G.; Qiao, R.; Huang, J.; Dai, S.; Sumpter, B. G.; Meunier, V. The Importance of Ion

Size and Electrode Curvature on Electrical Double Layers in Ionic Liquids. *Phys. Chem. Chem. Phys.* **2011**, *13*, 1152–1161.

(81) Van Aken, K. L.; McDonough, J. K.; Li, S.; Feng, G.; Chathoth, S. M.; Mamontov, E.; Fulvio, P. F.; Cummings, P. T.; Dai, S.; Gogotsi, Y. Effect of Cation on Diffusion Coefficient of Ionic Liquids at Onion-like Carbon Electrodes. *J. Phys. Condens. Matter* **2014**, *26*, 284104.

(82) Feng, G.; Cummings, P. T. Supercapacitor Capacitance Exhibits Oscillatory Behavior as a Function of Nanopore Size. *J. Phys. Chem. Lett.* **2011**, *2*, 2859–2864.

(83) Pinilla, C.; Del Pópolo, M. G.; Kohanoff, J.; Lynden-Bell, R. M. Polarization Relaxation in an Ionic Liquid Confined between Electrified Walls. *J. Phys. Chem. B* **2007**, *111*, 4877–4884.

(84) Fedorov, M. V.; Kornyshev, A. a. Ionic Liquid near a Charged Wall: Structure and Capacitance of Electrical Double Layer. *J. Phys. Chem. B* **2008**, *112*, 11868–11872.

(85) Shim, Y.; Kim, H. J. Nanoporous Carbon Supercapacitors in an Ionic Liquid: A Computer Simulation Study. *ACS Nano* **2010**, *4*, 2345–2355.

(86) Spohr, E. Molecular Simulation of the Electrochemical Double Layer. *Electrochim. Acta* **1999**, *44*, 1697–1705.

(87) Feng, G.; Jiang, D. E.; Cummings, P. T. Curvature Effect on the Capacitance of Electric Double Layers at Ionic Liquid/Onion-like Carbon Interfaces. *J. Chem. Theory Comput.* **2012**, *8*, 1058–1063.

(88) Kondrat, S.; Georgi, N.; Fedorov, M. V; Kornyshev, a a. A Superionic State in Nano-Porous Double-Layer Capacitors: Insights from Monte Carlo Simulations. *Phys. Chem. Chem. Phys.* **2011**, *13*, 11359–11366.

(89) Limmer, D. T.; Merlet, C.; Salanne, M.; Chandler, D.; Madden, P. a.; Van Roij, R.; Rotenberg, B. Charge Fluctuations in Nanoscale Capacitors. *Phys. Rev. Lett.* **2013**, *111*, 1–5.

(90) Luque, N. B.; Schmickler, W. The Electric Double Layer on Graphite. *Electrochim. Acta* **2012**, *71*, 82–85.

(91) Rochester, C. C.; Lee , A. a.; Pruessner, G.; Kornyshev, A. a. Interionic Interactions in Conducting Nanoconfinement. *ChemPhysChem* **2013**, *14*, 4121–4125.

(92) Siepmann, J. I.; Sprik, M. Influence of Surface Topology and Electrostatic Potential on Water/Electrode Systems. *J. Chem. Phys.* **1995**, *102*, 511–524.

(93) Reed, S. K.; Lanning, O. J.; Madden, P. a. Electrochemical Interface between an Ionic Liquid and a Model Metallic Electrode. *J. Chem. Phys.* **2007**, *126*, 084704.

(94) Merlet, C.; Péan, C.; Rotenberg, B.; Madden, P. a; Daffos, B.; Taberna, P.-L.; Simon, P.; Salanne, M. Highly Confined Ions Store Charge More Efficiently in Supercapacitors. *Nat. Commun.* **2013**, *4*, 2701.

(95) Péan, C.; Merlet, C.; Rotenberg, B.; Madden, P. A.; Taberna, P. L.; Daffos, B.; Salanne, M.; Simon, P. On the Dynamics of Charging in Nanoporous Carbon-Based Supercapacitors. *ACS Nano* **2014**, *8*, 1576–1583.

(96) Wang, Z.; Yang, Y.; Olmsted, D. L.; Asta, M.; Laird, B. B. Evaluation of the Constant Potential Method in Simulating Electric Double-Layer Capacitors. *J. Chem. Phys.* **2014**, *141*, 184102.

(97) Wang, Y.; Shi, Z.; Huang, Y.; Ma, Y.; Wang, C.; Chen, M.; Chen, Y. Supercapacitor Devices Based on Graphene Materials. *J. Phys. Chem. C* **2009**, *113*, 13103–13107.

(98) Dahl, I.; Kjølseth, C.; Fjeld, H.; Prytz, Ø.; Inge, P.; Estournès, C.; Haugsrud, R.; Norby, T.

Anomalous Increase in Carbon Capacitance at Pore Sizes Less Than 1 Nanometer. *Science (80-. ).* **2006**, *313*, 1760–1763.

(99) Stoller, M. D.; Park, S.; Zhu, Y.; An, J.; Ruoff, R. S. Graphene-Based Ultracapacitors. *Nano Lett.* **2008**, *8*, 3498–3502.

(100) Kott, T. M.; Hu, B.; Brown, S. H.; Kane, B. E. Valley-Degenerate Two-Dimensional Electrons in the Lowest Landau Level. *Phys. Rev. B - Condens. Matter Mater. Phys.* **2014**, *89*, 16–20.

(101) Shan, X.; Chen, S.; Wang, H.; Chen, Z.; Guan, Y.; Wang, Y.; Wang, S.; Chen, H. Y.; Tao, N. Mapping Local Quantum Capacitance and Charged Impurities in Graphene via Plasmonic Impedance Imaging. *Adv. Mater.* **2015**, *27*, 6213–6219.

(102) Brooksby, P. A.; Farquhar, A. K.; Dykstra, H. M.; Waterland, M. R.; Downard, A. J. Quantum Capacitance of Aryldiazonium Modified Large Area Few-Layer Graphene Electrodes. *J. Phys. Chem. C* **2015**, *119*, 25778–25785.

(103) Paek, E.; Pak, A. J.; Hwang, G. S. On the Influence of Polarization Effects in Predicting the Interfacial Structure and Capacitance of Graphene-like Electrodes in Ionic Liquids. *J. Chem. Phys.* **2015**, *142*, 024701.

(104) Stoller, M. D.; Magnuson, C. W.; Zhu, Y.; Murali, S.; Suk, J. W.; Piner, R.; Ruoff, R. S. Interfacial Capacitance of Single Layer Graphene. *Energy Environ. Sci.* **2011**, *4*, 4685–4689.

(105) Paek, E.; Pak, A. J.; Hwang, G. S. On the Influence of Polarization Effects in Predicting the Interfacial Structure and Capacitance of Graphene-like Electrodes in Ionic Liquids. *J. Chem. Phys.* **2015**, *142*, 0–6.

(106) Vatamanu, J.; Ni, X.; Liu, F.; Bedrov, D. Tailoring Graphene-Based Electrodes from

Semiconducting to Metallic to Increase the Energy Density in Supercapacitors. *Nanotechnology* **2015**, *26*, 464001.

(107) Zhang, L. L.; Zhao, X.; Ji, H.; Stoller, M. D.; Lai, L.; Murali, S.; Mcdonnell, S.; Cleveger, B.; Wallace, R. M.; Ruoff, R. S. Nitrogen Doping of Graphene and Its Effect on Quantum Capacitance, and a New Insight on the Enhanced Capacitance of N-Doped Carbon. *Energy Environ. Sci.* **2012**, *5*, 9618.

(108) Zhang, C.; Fu, L.; Liu, N.; Liu, M.; Wang, Y.; Liu, Z. Synthesis of Nitrogen-Doped Graphene Using Embedded Carbon and Nitrogen Sources. *Adv. Mater.* **2011**, *23*, 1020–1024.

(109) Zhan, C.; Zhang, Y.; Cummings, P. T.; Jiang, D. Enhancing Graphene Capacitance by Nitrogen: Effects of Doping Configuration and Concentration. *Phys. Chem. Chem. Phys.* **2016**, *18*, 4668–4674.

(110) Li, D.; Yu, C.; Wang, M.; Zhang, Y.; Pan, C. Synthesis of Nitrogen Doped Graphene from Graphene Oxide within an Ammonia Flame for High Performance Supercapacitors. *RSC Adv.* **2014**, *4*, 55394–55399.

(111) Jia, Z.; Wang, B.; Wang, Y.; Qi, T.; Liu, Y.; Wang, Q. Hierarchical Porous Nitrogen Doped Reduced Graphene Oxide Prepared by Surface Decoration-Thermal Treatment Method as High-Activity Oxygen Reduction Reaction Catalyst and High-Performance Supercapacitor Electrodes. *RSC Adv.* **2016**, *6*, 49497–49504.

(112) Sun, L.; Wang, L.; Tian, C.; Tan, T.; Xie, Y.; Shi, K.; Li, M.; Fu, H. Nitrogen-Doped Graphene with High Nitrogen Level via a One-Step Hydrothermal Reaction of Graphene Oxide with Urea for Superior Capacitive Energy Storage. *RSC Adv.* **2012**, *2*, 4498–4506.

(113) Sun, H. Ab Initio Characterizations of Molecular Structures, Conformation Energies, and

Hydrogen-Bonding Properties for Polyurethane Hard Segments. *Macromolecules* **1993**, *26*, 5924–5936.

(114) Berendsen, H. J. C.; Grigera, J. R.; Straatsma, T. P. The Missing Term in Effective Pair Potentials. *J. Phys. Chem.* **1987**, *91*, 6269–6271.

(115) Smith, D. E.; Dang, L. X. Interionic Potentials of Mean Force for SrCl2 in Polarizable Water. *Chem. Phys. Lett.* **1994**, *230*, 209–214.

(116) Yeh, I.-C.; Berkowitz, M. L. Ewald Summation for Systems with Slab Geometry. *J. Chem. Phys.* **1999**, *111*, 3155.

(117) Darden, T.; York, D.; Pedersen, L. Particle Mesh Ewald: An N Log(N) Method for Ewald Sums in Large Systems. *J. Chem. Phys.* **1993**, *98*, 10089.

(118) Berendsen, H. J. C.; Grigera, J. R.; Straatsma, T. P. The Missing Term in Effective Pair Potentials. *J. Phys. Chem.* **1987**, *91*, 6269–6271.

(119) Chialvo, A. A.; Vlcek, L.; Cummings, P. T. Surface Corrugation Effects on the Water–Graphene Interfacial and Confinement Behavior. *J. Phys. Chem. C* **2013**, *117*, 23875–23886.

(120) Wang, B.; Tsetseris, L.; Pantelides, S. T. Introduction of Nitrogen with Controllable Configuration into Graphene via Vacancies and Edges. *J. Mater. Chem. A* **2013**, *1*, 14927–14934.

(121) Paek, E.; Pak, A. J.; Kweon, K. E.; Hwang, G. S. On the Origin of the Enhanced Supercapacitor Performance of Nitrogen-Doped Graphene. *J. Phys. Chem. C* **2013**, *117*, 5610–5616.

(122) Lv, R.; Li, Q.; Botello-Méndez, A. R.; Hayashi, T.; Wang, B.; Berkdemir, A.; Hao, Q.; Eléas, A. L.; Cruz-Silva, R.; Gutiérrez, H. R.; et al. Nitrogen-Doped Graphene: Beyond

Single Substitution and Enhanced Molecular Sensing. *Sci. Rep.* **2012**, *2*, 1–8.

(123) Jiang, B.; Song, S.; Wang, J.; Xie, Y.; Chu, W.; Li, H.; Xu, H.; Tian, C.; Fu, H. Nitrogen-Doped Graphene Supported Pd@PdO Core-Shell Clusters for C-C Coupling Reactions. *Nano Res.* **2014**, *7*, 1280–1290.

(124) Wang, H.; Maiyalagan, T.; Wang, X. Review on Recent Progress in Nitrogen-Doped Graphene: Synthesis, Characterization, and Its Potential Applications. *ACS Catal.* **2012**, *2*, 781–794.

(125) Chen, R.; Wang, Y.; Liu, Y.; Li, J. Selective Electrochemical Detection of Dopamine Using Nitrogen-Doped Graphene/Manganese Monoxide Composites. *RSC Adv.* **2015**, *5*, 85065–85072.

(126) Jiang, B.; Tian, C.; Wang, L.; Sun, L.; Chen, C.; Nong, X.; Qiao, Y.; Fu, H. Highly Concentrated, Stable Nitrogen-Doped Graphene for Supercapacitors: Simultaneous Doping and Reduction. *Appl. Surf. Sci.* **2012**.

(127) Tian, Z.; Dai, S.; Jiang, D. E. Stability and Core-Level Signature of Nitrogen Dopants in Carbonaceous Materials. *Chem. Mater.* **2015**.

(128) Cao, H.; Zhou, X.; Qin, Z.; Liu, Z. Low-Temperature Preparation of Nitrogen-Doped Graphene for Supercapacitors. *Carbon N. Y.* **2013**, *56*, 218–223.

(129) Punnathanam, S. N. A Gibbs-Ensemble Based Technique for Monte Carlo Simulation of Electric Double Layer Capacitors (EDLC) at Constant Voltage. *J. Chem. Phys.* **2014**, *140*.

(130) Kiyohara, K.; Asaka, K. Monte Carlo Simulation of Porous Electrodes in the Constant Voltage Ensemble. *J. Phys. Chem. C* **2007**, *111*, 15903–15909.

(131) Wang, L.; Chen, X.; Zhu, W.; Wang, Y.; Zhu, C.; Wu, Z.; Han, Y.; Zhang, M.; Li, W.; He, Y.; et al. Detection of Resonant Impurities in Graphene by Quantum Capacitance

Measurement. *Phys. Rev. B - Condens. Matter Mater. Phys.* **2014**, *89*, 1–6.

(132) Pak, A. J.; Paek, E.; Hwang, G. S. Tailoring the Performance of Graphene-Based Supercapacitors Using Topological Defects: A Theoretical Assessment. *Carbon N. Y.* **2014**, *68*, 734–741.

(133) Pak, A. J.; Paek, E.; Hwang, G. S. Correction: Relative Contributions of Quantum and Double Layer Capacitance to the Supercapacitor Performance of Carbon Nanotubes in an Ionic Liquid. *Phys. Chem. Chem. Phys.* **2014**, *16*, 20248–20249.

(134) Yang, H. Targeted Nanosystems: Advances in Targeted Dendrimers for Cancer Therapy. *Nanomedicine Nanotechnology, Biol. Med.* **2016**, *12*, 309–316.

(135) Banerjee, S.; Shim, J.; Rivera, J.; Jin, X.; Estrada, D.; Solovyeva, V.; You, X.; Pak, J.; Pop, E.; Aluru, N.; et al. Electrochemistry at the Edge of a Single Graphene Layer in a Nanopore. *ACS Nano* **2013**, *7*, 834–843.

(136) Zheng, C.; Zhou, X. F.; Cao, H. L.; Wang, G. H.; Liu, Z. P. Edge-Enriched Porous Graphene Nanoribbons for High Energy Density Supercapacitors. *J. Mater. Chem. A* **2014**, *2*, 7484–7490.

(137) Yuan, W.; Zhou, Y.; Li, Y.; Li, C.; Peng, H.; Zhang, J.; Liu, Z.; Dai, L.; Shi, G. The Edge- and Basal-Plane-Specific Electrochemistry of a Single-Layer Graphene Sheet. *Sci. Rep.* **2013**, *3*, 1–7.

(138) Zhan, C.; Jiang, D. Contribution of Dielectric Screening to the Total Capacitance of Few-Layer Graphene Electrodes. **2016**.

(139) Jia, X.; Campos-Delgado, J.; Terrones, M.; Meunier, V.; Dresselhaus, M. S. Graphene Edges: A Review of Their Fabrication and Characterization. *Nanoscale* **2011**, *3*, 86–95.

(140) Abraham, M. J.; Murtola, T.; Schulz, R.; Páall, S.; Smith, J. C.; Hess, B.; Lindah, E.

Gromacs: High Performance Molecular Simulations through Multi-Level Parallelism from Laptops to Supercomputers. *SoftwareX* **2015**, *1–2*, 19–25.

(141) Berendsen, H. J. C.; Postma, J. P. M.; van Gunsteren, W. F.; DiNola, a; Haak, J. R. Molecular Dynamics with Coupling to an External Bath. *J. Chem. Phys.* **1984**, *81*, 3684–3690.

(142) Pak, a J.; Paek, E.; Hwang, G. S. Impact of Graphene Edges on Enhancing the Performance of Electrochemical Double Layer Capacitors. *J. Phys. Chem. C* **2014**, *118*, 21770–21777.

(143) Ji, H.; Zhao, X.; Qiao, Z.; Jung, J.; Zhu, Y.; Lu, Y.; Zhang, L. L.; MacDonald, A. H.; Ruoff, R. S. Capacitance of Carbon-Based Electrical Double-Layer Capacitors. *Nat. Commun.* **2014**, *5*, 1–7.

(144) Yang, H.; Zhang, X.; Yang, J.; Bo, Z.; Hu, M.; Yan, J.; Cen, K. Molecular Origin of Electric Double-Layer Capacitance at Multilayer Graphene Edges. *J. Phys. Chem. Lett.* **2016**, acs.jpclett.6b02659.

(145) Tian, J.; Cao, H.; Wu, W.; Yu, Q.; Chen, Y. P. Direct Imaging of Graphene Edges: Atomic Structure and Electronic Scattering. *Nano Lett.* **2011**, *11*, 3663–3668.

(146) Wei, D.; Wang, F. Relative Stability of Armchair, Zigzag and Reczag Graphene Edges on the Ru(0001) Surface. *Surf. Sci.* **2012**, *606*, 485–489.

(147) Shu, H.; Chen, X.; Tao, X.; Ding, F. Edge Structural Stability and Kinetics of Graphene Chemical Vapor Deposition Growth. *ACS Nano* **2012**, *6*, 3243–3250.

(148) Ruffieux, P.; Wang, S.; Yang, B.; Sanchez-Sanchez, C.; Liu, J.; Dienel, T.; Talirz, L.; Shinde, P.; Pignedoli, C. A.; Passerone, D.; et al. On-Surface Synthesis of Graphene Nanoribbons with Zigzag Edge Topology. *Nature* **2016**, *531*, 489–492.

(149) Simon, P.; Gogotsi, Y. Charge Storage Mechanism in Nanoporous Carbons and Its Consequence for Electrical Double Layer Capacitors. *Philos. Trans. R. Soc. A Math. Phys. Eng. Sci.* **2010**, *368*, 3457–3467.

(150) Perkin, S.; Salanne, M.; Madden, P.; Lynden-Bell, R. Is a Stern and Diffuse Layer Model Appropriate to Ionic Liquids at Surfaces? *Proc. Natl. Acad. Sci.* **2013**, *110*, E4121–E4121.

(151) Deyoung, A. D.; Park, S. W.; Dhumal, N. R.; Shim, Y.; Jung, Y.; Kim, H. J. Graphene Oxide Supercapacitors: A Computer Simulation Study. *J. Phys. Chem. C* **2014**, *118*, 18472–18480.

(152) Feng, G.; Li, S.; Presser, V.; Cummings, P. T. Molecular Insights into Carbon Supercapacitors Based on Room-Temperature Ionic Liquids. *J. Phys. Chem. Lett.* **2013**, *4*, 3367–3376.

(153) Chmiola, J.; Yushin, G.; Dash, R.; Gogotsi, Y. Effect of Pore Size and Surface Area of Carbide Derived Carbons on Specific Capacitance. *J. Power Sources* **2006**, *158*, 765–772.

(154) Huang, J.; Sumpter, B. G.; Meunier, V. A Universal Model for Nanoporous Carbon Supercapacitors Applicable to Diverse Pore Regimes, Carbon Materials, and Electrolytes. *Chem. - A Eur. J.* **2008**, *14*, 6614–6626.

(155) Uesugi, E.; Goto, H.; Eguchi, R.; Fujiwara, A.; Kubozono, Y. Electric Double-Layer Capacitance between an Ionic Liquid and Few-Layer Graphene. *Sci. Rep.* **2013**, *3*, 1595.

(156) Zhan, C.; Neal, J.; Wu, J.; Jiang, D. Quantum Effects on the Capacitance of Graphene-Based Electrodes. *J. Phys. Chem. C* **2015**, 150917101153000.

(157) Kerisit, S.; Schwenzer, B.; Vijayakumar, M. Effects of Oxygen-Containing Functional Groups on Supercapacitor Performance. *J. Phys. Chem. Lett.* **2014**, *5*, 2330–2334.

(158) Fornasiero, F.; In, J. Bin; Kim, S.; Park, H. G.; Wang, Y.; Grigoropoulos, C. P.; Noy, A.;

Bakajin, O. PH-Tunable Ion Selectivity in Carbon Nanotube Pores. *Langmuir* **2010**, *26*, 14848–14853.

(159) Joseph, S.; Mashl, R. J.; Jakobsson, E.; Aluru, N. R. Electrolytic Transport in Modified Carbon Nanotubes. *Nano Lett.* **2003**, *3*, 1399–1403.

(160) Pean, C.; Daffos, B.; Rotenberg, B.; Levitz, P.; Haefele, M.; Taberna, P. L.; Simon, P.; Salanne, M. Confinement, Desolvation, and Electrosorption Effects on the Diffusion of Ions in Nanoporous Carbon Electrodes. *J. Am. Chem. Soc.* **2015**, *137*, 12627–12632.

(161) Rajput, N. N.; Monk, J.; Singh, R.; Hung, F. R. On the Influence of Pore Size and Pore Loading on Structural and Dynamical Heterogeneities of an Ionic Liquid Confined in a Slit Nanopore. *J. Phys. Chem. C* **2012**, *116*, 5169–5181.

(162) Monk, J.; Singh, R.; Hung, F. R. Effects of Pore Size and Pore Loading on the Properties of Ionic Liquids Confined inside Nanoporous CMK-3 Carbon Materials. *J. Phys. Chem. C* **2011**, *115*, 3034–3042.

(163) Kondrat, S.; Wu, P.; Qiao, R.; Kornyshev, A. A. Accelerating Charging Dynamics in Subnanometre Pores. *Nat. Mater.* **2014**, *13*, 387–393.

(164) Fedorov, M. V.; Kornyshev, A. A. Ionic Liquids at Electrified Interfaces. *Chem. Rev.* **2014**, *114*, 2978–3036.

(165) Ohba, T.; Kojima, N.; Kanoh, H.; Kaneko, K. Supporting Information for Unique Hydrogen-Bonded Structure of Water around Ca Ions Confined in Carbon Slit Pore. **2009**, 1–12.

(166) Frolov, A. I.; Kirchner, K.; Kirchner, T.; Fedorov, M. V. Molecular-Scale Insights into the Mechanisms of Ionic Liquids Interactions with Carbon Nanotubes. *Faraday Discuss.* **2012**, *154*, 235–247.

(167) Baldelli, S. Surface Structure at the Ionic Liquid-Electrified Metal Interface. *Acc. Chem. Res.* **2008**, *41*, 421–431.

(168) Richey, F. W.; Tran, C.; Kalra, V.; Elabd, Y. A. Ionic Liquid Dynamics in Nanoporous Carbon Nanofibers in Supercapacitors Measured with in Operando Infrared Spectroelectrochemistry. *J. Phys. Chem. C* **2014**, *118*, 21846–21855.

(169) Canongia Lopes, J. N. A.; Pádua, A. A. H. Nanostructural Organization in Ionic Liquids. *J. Phys. Chem. B* **2006**, *110*, 3330–3335.

(170) Fedorov, M. V.; Kornyshev, A. a. Ionic Liquids at Electrified Interfaces. *Chem. Rev.* **2014**, *114*, 2978–3036.

(171) Hayes, R.; Warr, G. G.; Atkin, R. Structure and Nanostructure in Ionic Liquids. *Chem. Rev.* **2015**, 150601082109009.

(172) Lopes, J. N. C.; Pádua, A. A. H. Molecular Force Field for Ionic Liquids Composed of Triflate or Bistriflylimide Anions. *J. Phys. Chem. B* **2004**, *108*, 16893–16898.

(173) Canongia Lopes, J. N.; Deschamps, J.; Pádua, A. A. H. Modeling Ionic Liquids Using a Systematic All-Atom Force Field. *J. Phys. Chem. B* **2004**, *108*, 2038–2047.

(174) Yan, J. A.; Xian, L.; Chou, M. Y. Structural and Electronic Properties of Oxidized Graphene. *Phys. Rev. Lett.* **2009**, *103*, 1–4.

(175) Cornell, W. D.; Cieplak, P.; Bayly, C. I.; Gould, I. R.; Merz, K. M.; Ferguson, D. M.; Spellmeyer, D. C.; Fox, T.; Caldwell, J. W.; Kollman, P. a. A Second Generation Force Field for the Simulation of Proteins, Nucleic Acids, and Organic Molecules. *J. Am. Chem. Soc.* **1995**, *117*, 5179–5197.

(176) Feng, G.; Huang, J.; Sumpter, B. G.; Meunier, V.; Qiao, R. Structure and Dynamics of Electrical Double Layers in Organic Electrolytes. *Phys. Chem. Chem. Phys.* **2010**, *12*,

5468–5479.

(177) Krueger, A. *Carbon Nanomaterials*; 2014; Vol. 10.

(178) Feng, G.; Qiao, R.; Huang, J.; Sumpter, B. G.; Meunier, V. Ion Distribution in Electrified Micropores and Its Role in the Anomalous Enhancement of Capacitance. *ACS Nano* **2010**, *4*, 2382–2390.

(179) Lockett, V.; Sedev, R.; Ralston, J.; Horne, M.; Rodopoulos, T. Differential Capacitance of the Electrical Double Layer in Imidazolium-Based Ionic Liquids: Influence of Potential, Cation Size, and Temperature. *J. Phys. Chem. C* **2008**, *112*, 7486–7495.

(180) Zhan, C.; Zhang, Y.; Cummings, P. T.; Jiang, D. en. Computational Insight into the Capacitive Performance of Graphene Edge Planes. *Carbon N. Y.* **2017**, *116*, 278–285.

(181) Bazant, M. Z.; Storey, B. D.; Kornyshev, A. A. Double Layer in Ionic Liquids: Overscreening versus Crowding. *Phys. Rev. Lett.* **2011**, *106*, 6–9.

(182) Liu, K.; Wu, J. Boosting the Performance of Ionic-Liquid-Based Supercapacitors with Polar Additives. *J. Phys. Chem. C* **2016**, *120*, 24041–24047.

(183) He, Y.; Qiao, R.; Vatamanu, J.; Borodin, O.; Bedrov, D.; Huang, J.; Sumpter, B. G. Importance of Ion Packing on the Dynamics of Ionic Liquids during Micropore Charging. *J. Phys. Chem. Lett.* **2016**, *7*, 36–42.

(184) Kondrat, S.; Wu, P.; Qiao, R.; Kornyshev, A. a. Accelerating Charging Dynamics in Subnanometre Pores. *Nat. Mater.* **2014**, *13*, 387–393.

(185) Kumar, P. V.; Bardhan, N. M.; Tongay, S.; Wu, J.; Belcher, A. M.; Grossman, J. C. Scalable Enhancement of Graphene Oxide Properties by Thermally Driven Phase Transformation. *Nat. Chem.* **2014**, *6*, 151–158.

(186) Mysyk, R.; Raymundo-Piñero, E.; Béguin, F. Saturation of Subnanometer Pores in an

Electric Double-Layer Capacitor. *Electrochem. commun.* **2009**, *11*, 554–556.

(187) Richey, F. W.; Dyatkin, B.; Gogotsi, Y.; Elabd, Y. A. Ion Dynamics in Porous Carbon Electrodes in Supercapacitors Using in Situ Infrared Spectroelectrochemistry. *J. Am. Chem. Soc.* **2013**, *135*, 12818–12826.

(188) Chathoth, S. M.; Mamontov, E.; Dai, S.; Wang, X.; Fulvio, P. F.; Wesolowski, D. J. Fast Diffusion in a Room Temperature Ionic Liquid Confined in Mesoporous Carbon. *Epl* **2012**, *97*.

(189) Forse, A. C.; Merlet, C.; Allan, P. K.; Humphreys, E. K.; Griffin, J. M.; Aslan, M.; Zeiger, M.; Presser, V.; Gogotsi, Y.; Grey, C. P. New Insights into the Structure of Nanoporous Carbons from NMR, Raman, and Pair Distribution Function Analysis. *Chem. Mater.* **2015**, *27*, 6848–6857.

(190) Petkov, V.; Difrancesco, R. G.; Billinge, S. J. L.; Acharya, M.; Foley, H. C. Local Structure of Nanoporous Carbons. *Philos. Mag. B Phys. Condens. Matter; Stat. Mech. Electron. Opt. Magn. Prop.* **1999**, *79*, 1519–1530.

(191) Smith, M. A.; Foley, H. C.; Lobo, R. F. A Simple Model Describes the PDF of a Non-Graphitizing Carbon. *Carbon N. Y.* **2004**, *42*, 2041–2048.

(192) He, Y.; Huang, J.; Sumpter, B. G.; Kornyshev, A. A.; Qiao, R. Dynamic Charge Storage in Ionic Liquids-Filled Nanopores: Insight from a Computational Cyclic Voltammetry Study. **2015**.

(193) Pak, A. J.; Hwang, G. S. Charging Rate Dependence of Ion Migration and Stagnation in Ionic-Liquid-Filled Carbon Nanopores. *J. Phys. Chem. C* **2016**, *120*, 24560–24567.

(194) Dyatkin, B.; Mamontov, E.; Cook, K. M.; Gogotsi, Y. Capacitance, Charge Dynamics, and Electrolyte-Surface Interactions in Functionalized Carbide-Derived Carbon

Electrodes. *Prog. Nat. Sci. Mater. Int.* **2015**, *25*, 631–641.

(195) Dyatkin, B.; Zhang, Y.; Mamontov, E.; Kolesnikov, A. I.; Cheng, Y.; Meyer, H. M.; Cummings, P. T.; Gogotsi, Y. Influence of Surface Oxidation on Ion Dynamics and Capacitance in Porous and Nonporous Carbon Electrodes. *J. Phys. Chem. C* **2016**, *120*, 8730–8741.

(196) Chathoth, S. M.; Mamontov, E.; Fulvio, P. F.; Wang, X.; Baker, G. A.; Dai, S.; Wesolowski, D. J. An Unusual Slowdown of Fast Diffusion in a Room Temperature Ionic Liquid Confined in Mesoporous Carbon. *Epl* **2013**, *102*.

(197) Hayes, R.; Warr, G. G.; Atkin, R. Structure and Nanostructure in Ionic Liquids. *Chem. Rev.* **2015**, *115*, 6357–6426.

(198) McEwen, A. B. Nonaqueous Electrolytes for Electrochemical Capacitors: Imidazolium Cations and Inorganic Fluorides with Organic Carbonates. *J. Electrochem. Soc.* **2006**, *144*, L84.

(199) Dyatkin, B.; Osti, N. C.; Gallegos, A.; Zhang, Y.; Mamontov, E.; Cummings, P. T.; Wu, J.; Gogotsi, Y. Electrolyte Cation Length Influences Electrosorption and Dynamics in Porous Carbon Supercapacitors. *Electrochim. Acta* **2018**, *283*, 882–893.

(200) Yoon, H.; Best, A. S.; Forsyth, M.; MacFarlane, D. R.; Howlett, P. C. Physical Properties of High Li-Ion Content N-Propyl-N-Methylpyrrolidinium Bis(Fluorosulfonyl)Imide Based Ionic Liquid Electrolytes. *Phys. Chem. Chem. Phys.* **2015**, *17*, 4656–4663.

(201) Zhou, Q.; Henderson, W. A.; Appetecchi, G. B.; Montanino, M.; Passerini, S. Physical and Electrochemical Properties of N-Alkyl-N-Methylpyrrolidinium Bis(Fluorosulfonyl)Imide Ionic Liquids: PY13FSI and PY 14FSI. *J. Phys. Chem. B* **2008**, *112*, 13577–13580.

(202) Balducci, A.; Henderson, W. A.; Mastragostino, M.; Passerini, S.; Simon, P.; Soavi, F. Cycling Stability of a Hybrid Activated Carbon//Poly(3-Methylthiophene) Supercapacitor with N-Butyl-N-Methylpyrrolidinium Bis(Trifluoromethanesulfonyl) Imide Ionic Liquid as Electrolyte. *Electrochim. Acta* **2005**, *50*, 2233–2237.

(203) Profatilova, I. A.; Choi, N. S.; Roh, S. W.; Kim, S. S. Electrochemical and Thermal Properties of Graphite Electrodes with Imidazolium- and Piperidinium-Based Ionic Liquids. *J. Power Sources* **2009**, *192*, 636–643.

(204) Lane, G. H.; Bayley, P. M.; Clare, B. R.; Best, A. S.; Macfarlane, D. R.; Forsyth, M.; Hollenkamp, A. F. Ionic Liquid Electrolyte for Lithium Metal Batteries: Physical, Electrochemical, and Interfacial Studies Of. *Society* **2010**, 21775–21785.

(205) Borodin, O.; Jow, T. R. Quantum Chemistry Studies of the Oxidative Stability of Carbonate, Sulfone and Sulfonate-Based Electrolytes Doped with BF; 2011; Vol. 33, pp 77–84.

(206) Van Aken, K. L.; Beidaghi, M.; Gogotsi, Y. Formulation of Ionic-Liquid Electrolyte to Expand the Voltage Window of Supercapacitors. *Angew. Chemie - Int. Ed.* **2015**, *54*, 4806–4809.

(207) Lin, R.; Taberna, P.; Presser, V.; Carlos, R. P.; Rupesinghe, N. L.; Teo, K. B. K.; Gogotsi, Y.; Simon, P. Capacitive Energy Storage from À 50 to 100 ° C Using an Ionic Liquid Electrolyte. **2011**, 2396–2401.

(208) Fox, E. T.; Weaver, J. E. F.; Henderson, W. A. Tuning Binary Ionic Liquid Mixtures: Linking Alkyl Chain Length to Phase Behavior and Ionic Conductivity. *J. Phys. Chem. C* **2012**, *116*, 5270–5274.

(209) Wang, X.; Mehandzhiyski, A. Y.; Arstad, B.; Van Aken, K. L.; Mathis, T. S.; Gallegos,

A.; Tian, Z.; Ren, D.; Sheridan, E.; Grimes, B. A.; et al. Selective Charging Behavior in an Ionic Mixture Electrolyte-Supercapacitor System for Higher Energy and Power. *J. Am. Chem. Soc.* **2017**, *139*, 18681–18687.

(210) Tsai, W. Y.; Lin, R.; Murali, S.; Li Zhang, L.; McDonough, J. K.; Ruoff, R. S.; Taberna, P. L.; Gogotsi, Y.; Simon, P. Outstanding Performance of Activated Graphene Based Supercapacitors in Ionic Liquid Electrolyte from -50 to 80°C. *Nano Energy* **2013**, *2*, 403–411.

(211) Wang, X.; Zhou, H.; Sheridan, E.; Walmsley, J. C.; Ren, D.; Chen, D. Geometrically Confined Favourable Ion Packing for High Gravimetric Capacitance in Carbon-Ionic Liquid Supercapacitors. *Energy Environ. Sci.* **2016**, *9*, 232–239.

(212) Olivier-Bourbigou, H.; Magna, L. Ionic Liquids: Perspectives for Organic and Catalytic Reactions. *J. Mol. Catal. A Chem.* **2002**, *182–183*, 419–437.

(213) Kosmulski, M.; Gustafsson, J.; Rosenholm, J. B. Thermal Stability of Low Temperature Ionic Liquids Revisited. *Thermochim. Acta* **2004**, *412*, 47–53.

(214) Quinn, B. M.; Ding, Z.; Moulton, R.; Bard, A. J. Novel Electrochemical Studies of Ionic Liquids. *Langmuir* **2002**, *18*, 1734–1742.

(215) Tivony, R.; Safran, S.; Pincus, P.; Silbert, G.; Klein, J. Charging Dynamics of an Individual Nanopore. *Nat. Commun.* **2018**, *9*, 4203.

(216) Lee, A. A.; Kondrat, S.; Vella, D.; Goriely, A. Dynamics of Ion Transport in Ionic Liquids. *Phys. Rev. Lett.* **2015**, *115*, 1–5.

(217) Dyatkin, B.; Osti, N. C.; Zhang, Y.; Wang, H.-W.; Mamontov, E.; Heller, W. T.; Zhang, P.; Rother, G.; Cummings, P. T.; Wesolowski, D. J.; et al. Ionic Liquid Structure, Dynamics, and Electrosorption in Carbon Electrodes with Bimodal Pores and

Heterogeneous Surfaces. *Carbon N. Y.* **2018**, *129*, 104–118.

(218) Dyatkin, B.; Gogotsi, O.; Malinovskiy, B.; Zozulya, Y.; Simon, P.; Gogotsi, Y. High Capacitance of Coarse-Grained Carbide Derived Carbon Electrodes. *J. Power Sources* **2016**, *306*, 32–41.

(219) Li, Z.; Mendez-Morales, T.; Salanne, M. Computer Simulation Studies of Nanoporous Carbon-Based Electrochemical Capacitors. *Curr. Opin. Electrochem.* **2018**, *9*, 81–86.

(220) Hoover, W. G. Canonical Dynamics: Equilibrium Phase-Space Distributions. *Phys. Rev. A* **1985**, *31*, 1695–1697.

(221) Zhong, X.; Liu, Z.; Cao, D. Improved Classical United-Atom Force Field for Imidazolium-Based Ionic Liquids: Tetrafluoroborate, Hexafluorophosphate, Methylsulfate, Trifluoromethylsulfonate, Acetate, Trifluoroacetate, and Bis(Trifluoromethylsulfonyl)Amide. *J. Phys. Chem. B* **2011**, *115*, 10027–10040.

(222) Essmann, U.; Perera, L.; Berkowitz, M. L.; Darden, T.; Lee, H.; Pedersen, L. G. A Smooth Particle Mesh Ewald Method. *J Chem Phys* **1995**, *103*, 8577–8593.

(223) Wu, X.; Liu, Z.; Huang, S.; Wang, W.; Simulation, M. Molecular Dynamics Simulation of Room-Temperature Ionic Liquid Mixture of [Bmim][BF 4 ] and Acetonitrile by a Refined Force Field W. **2005**, 2771–2779.

(224) Yan, J. A.; Chou, M. Y. Oxidation Functional Groups on Graphene: Structural and Electronic Properties. *Phys. Rev. B - Condens. Matter Mater. Phys.* **2010**, *82*, 21–24.

(225) Rizzo, R. C.; Jorgensen, W. L. OPLS All-Atom Model for Amines: Resolution of the Amine Hydration Problem. *J. Am. Chem. Soc.* **1999**, *121*, 4827–4836.

(226) Sun, H.; Mumby, S. J.; Maple, J. R.; Hagler, A. T. An Ab Initio CFF93 All-Atom Force Field for Polycarbonates. *J. Am. Chem. Soc.* **1994**, *116*, 2978–2987.

(227) Hess, B.; Bekker, H.; Berendsen, H. J. C.; Fraaije, J. G. E. M. LINCS: A Linear Constraint Solver for Molecular Simulations. *J. Comput. Chem.* **1997**, *18*, 1463–1472.

(228) Vatamanu, J.; Vatamanu, M.; Borodin, O.; Bedrov, D. A Comparative Study of Room Temperature Ionic Liquids and Their Organic Solvent Mixtures near Charged Electrodes. *J. Phys. Condens. Matter* **2016**, *28*.

(229) Rajput, N. N.; Monk, J.; Hung, F. R. Ionic Liquids Confined in a Realistic Activated Carbon Model: A Molecular Simulation Study. *J. Phys. Chem. C* **2014**, *118*, 1540–1553.

(230) Kondrat, S.; Kornyshev, A. Corrigendum: Superionic State in Double-Layer Capacitors with Nanoporous Electrodes. *J. Phys. Condens. Matter* **2013**, *25*, 119501.

(231) Merlet, C.; Rotenberg, B.; Madden, P. a; Taberna, P.-L.; Simon, P.; Gogotsi, Y.; Salanne, M. On the Molecular Origin of Supercapacitance in Nanoporous Carbon Electrodes. *Nat. Mater.* **2012**, *11*, 306–310.

(232) Banda, H.; Daffos, B.; Périé, S.; Chenavier, Y.; Dubois, L.; Aradilla, D.; Pouget, S.; Simon, P.; Crosnier, O.; Taberna, P. L.; et al. Ion Sieving Effects in Chemically Tuned Pillared Graphene Materials for Electrochemical Capacitors. *Chem. Mater.* **2018**, *30*, 3040–3047.

(233) Naguib, M.; Mochalin, V. N.; Barsoum, M. W.; Gogotsi, Y. 25th Anniversary Article: MXenes: A New Family of Two-Dimensional Materials. *Adv. Mater.* **2014**, *26*, 992–1005.

(234) Lukatskaya, M. R.; Mashtalir, O.; Ren, C. E.; Dall'Agnese, Y.; Rozier, P.; Taberna, P. L.; Naguib, M.; Simon, P.; Barsoum, M. W.; Gogotsi, Y. Cation Intercalation and High Volumetric Capacitance of Two-Dimensional Titanium Carbide. *Science (80-. ).* **2013**, *341*, 1502–1505.

(235) Dall'Agnese, Y.; Lukatskaya, M. R.; Cook, K. M.; Taberna, P. L.; Gogotsi, Y.; Simon, P.

High Capacitance of Surface-Modified 2D Titanium Carbide in Acidic Electrolyte. *Electrochem. commun.* **2014**.

(236) Lukatskaya, M. R.; Mashtalir, O.; Ren, C. E.; Dall'Agnese, Y.; Rozier, P.; Taberna, P. L.; Naguib, M.; Simon, P.; Barsoum, M. W.; Gogotsi, Y. Cation Intercalation and High Volumetric Capacitance of Two-Dimensional Titanium Carbide. *Science (80-. ).* **2013**.

(237) Xu, K.; Lin, Z.; Merlet, C.; Taberna, P. L.; Miao, L.; Jiang, J.; Simon, P. Tracking Ionic Rearrangements and Interpreting Dynamic Volumetric Changes in Two-Dimensional Metal Carbide Supercapacitors: A Molecular Dynamics Simulation Study. *ChemSusChem* **2018**, 1–9.

(238) Zhang, X.; Zhang, Z.; Zhou, Z. MXene-Based Materials for Electrochemical Energy Storage. *J. Energy Chem.* **2018**, *27*, 73–85.

(239) Wang, X.; Mathis, T. S.; Li, K.; Lin, Z.; Vlcek, L.; Torita, T.; Osti, N. C.; Hatter, C.; Urbankowski, P.; Sarycheva, A.; et al. Influences from Solvents on Charge Storage in Titanium Carbide MXenes. *Nat. Energy* **2019**.

(240) Klein, C.; Sallai, J.; Jones, T. J.; Iacovella, C. R.; McCabe, C.; Cummings, P. T. A Hierarchical, Component Based Approach to Screening Properties of Soft Matter; 2016.

(241) Griffin, J. M.; Forse, A. C.; Tsai, W. Y.; Taberna, P. L.; Simon, P.; Grey, C. P. In Situ NMR and Electrochemical Quartz Crystal Microbalance Techniques Reveal the Structure of the Electrical Double Layer in Supercapacitors. *Nat. Mater.* **2015**, *14*, 812–819.